# Noise Computation of Induction Machines

Zur Erlangung des akademischen Grades eines
Doktors der technischen Wissenschaften
ausgeführte Dissertation

eingereicht an der
Fakultät für Elektrotechnik
der Technischen Universität Graz

von

Bernhard Weilharter

Berichter: Univ.-Prof. Dr.-techn. Oszkár Bíró
Univ.-Prof. Dr.-Ing. habil. Katrin Ellermann

Graz, 31. Juli 2012

## Abstract

Audible noise radiated by electrical machines is gaining more and more in importance in the design process of electrical machines. Therefore, computation methods are necessary which identify the problematic noise sources and facilitate a low noise design.

This work begins with the validation of an analytical approach to determine the noise behaviour of induction machines. Analytical electromagnetic, structural, and acoustical computations are performed. The obtained results are then compared with data from numerical computations as well as vibration and noise measurements.

Investigations of the noise behaviour of induction machines demand the calculation of the rotating stress waves and thus the determination of the magnetic field-harmonics. Therefore, a method to compute the field-harmonics of a skewed induction machine using a multi-slice model has been developed.

Following that, the surface vibrations of an induction machine due to stress waves acting on the stator and rotor core are analysed. The focus lies on the investigation of the influence of stress waves varying in axial direction and with higher spatial ordinal numbers on the surface vibration of a squirrel cage induction machine.

At last, the rotating stress waves acting in the air gap of an induction machine at nominal operating point and obtained by an electromagnetic finite element multi-slice simulation are applied to a three-dimensional structural finite element model. A structural harmonic simulation is then performed. With a three-dimensional boundary element model the sound pressure on the surface of the machine is computed along with the noise radiation in the environment.

# Zusammenfassung

Im Auslegungsprozess von elektrischen Maschinen spielt die Geräuschberechnung eine immer wichtigere Rolle. Um die Lärmquellen zu identifizieren und entsprechende Modifikationen vorzunehmen sind geeignete Berechnungsmethoden notwendig.

Diese Arbeit beginnt mit der Validierung eines analytischen Berechnungsverfahrens zur Ermittlung des Geräuschverhaltens von Asynchronmaschinen. Dieses Verfahren umfasst elektromagnetische, strukturmechanische und akustische Berechnungen. Die ermittelten Ergebnisse werden mit numerischen Lösungen und Messdaten von Schwingungs- und Geräuschmessungen verglichen.

Die Untersuchungen des Geräuschverhaltens von elektrischen Maschinen erfordert die Berechnung der Kräfte, insbesondere deren Harmonische, die aus den Oberwellen des Luftspaltfeldes resultieren. Für geschrägte Maschinen wurde eine Methode entwickelt, mit der die Oberfelder und deren Verteilung in axialer Richtung mit Hilfe eines Multi-Slice Modells ermittelt werden können.

Im Anschluss daran wird der Einfluss unterschiedlicher Kraftwellen, die auf den Stator oder Rotor einer Asynchronmaschine wirken, auf das Schwingungsverhalten untersucht. Besonderes Augenmerk liegt dabei auf Kraftwellen mit hohen Ordnungszahlen bzw. mit ungleichförmiger Verteilung in axialer Richtung.

Als letzer Punkt wurde die Schallabstrahlung einer Asynchronmaschine berechnet. Mit Hilfe der Finite Elemente Methode wurden die elektromagnetischen Kräfte, die in einer geschrägten Asynchronmaschine im Nennbetriebspunkt wirken, ermittelt und anschließend die Vibrationen mit einem geeigneten Strukturmodell berechnet. Die Schwingungen an der Oberfläche der Maschine dienen als Eingangsgröße für die Randelemente Methode zur Berechnung des Schalldrucks an der Oberfläche der Maschine sowie der Schallausbreitung in die Umgebung.

## Acknowledgements

Working in the Christian Doppler Laboratory for Multiphysical Simulation, Analysis and Design of Electrical Machines was a very interesting as well as challenging experience to me. At this point, I would like to thank those people, without whose precious support throughout these years, this work would not have been possible.

First of all, I would like to express my deep gratitude to my research supervisor Univ.-Prof. Dr.-techn. Oszkár Bíró. Thank you for your patient guidance, enthusiastic encouragement and constructive feedback.

Furthermore, I would like to thank the Christian Doppler Research Association (CDG) who has supported this research.

I am also deeply grateful for the support of the ELIN Motoren Gmbh. Special thanks in particular to Dr. Georg Ofner and Dr. Hermann Lang for your advices and assistance throughout this work and for the productive working relationship.

My thanks are also extended to the Institute of Mechanics at the Graz University of Technology, with Univ.-Prof. Dr.-Ing. habil. Kathrin Ellermann as the head of it, for providing measurement facilities and in particular to Mr. Mathias Mair for the contributions to this work.

I am deeply indebted to Mr. Siegfried Rainer, Dr. Andrej Stermecki, Mr. Martin Hettegger and Mr. Paul Handgruber, my colleagues from the Christian Doppler Laboratory and the Institute for Fundamentals and Theory in Electrical Engineering at the Graz University of Technology. Your contributions, advices and detailed comments have been of great value to me.

Finally, I want to thank my family and friends for their patience and their encouragement which I appreciate very much.

# CONTENTS

# 1 INTRODUCTION

## 1.1 Motivation

Electrical machines nowadays are an integral part in our modern and technophile society in everyday life situations. The increase in electrification is not only eminent in the personal household but also in industrial applications and the trend seems to be a further increase, not only because the efficiency and application possibilities rise due to technological enhancements e.g. in inverter feeding, but also because the urge to sustainable and ecological-friendly policy grows. The automotive industry can be mentioned as a prominent example, where electrical drives are gaining more and more interest and, after hybrid applications, the trend to purely electric driven vehicles is meanwhile conceivable.

Furthermore, the trend to higher electrification also implies an increased energy demand to be satisfied. The increasing sensitivity towards sustainability and ecological friendly applications makes the way for alternative power plants, as for example wind power, resulting in new application areas and beyond that new requirements and challenges.

As human beings play the key-role in the usage and operation of these technologies, their increase also leads to an increased exposition to their emissions, at work and at home, thus 24 hours a day. One problematic emission of electrical machines is audible noise, which is gaining more and more attention due to the rising sensitivity regarding the quality of life.

Besides physical effects on the human hearing, also psychological effects, like release of stress hormones result in impairment of humans health. According to [4], noise "has emerged as the leading environmental nuisance in Europe" and is "the third largest environmental burden of disease". Therefore this issue is gaining more and more in importance in human society. Depending on the possible effects, there exist different regulations especially for industrial applications [1], that have to be considered already in the design process of electrical machines.

Although the human ear covers a frequency range of about 16Hz to 16000Hz, it reacts most sensitively in a range of 1000 to 5000 Hz. Looking at the spectral content of the noise of electrical machines, the most problematic noise peaks arise exactly in this frequency interval. This means that special care has to be taken in the design process to keep their noise levels low so that no harm of the human hearing can occur.

As the demands regarding efficiency and costs also rise, the noise estimation process becomes more and more complex. More transferred power means larger forces acting on the machine and thus higher emitted noise. The reduction of material not only saves money, but as the construction changes, typically more problems with resonances occur, especially for low weight designs. The arising forces must not interfere with these natural frequencies as this leads to large noise peaks and, besides that, may even lead to damages

of the machine. The ever widening employment of inverter feeding of electrical machines increases the number of occurring frequencies in a machine. The chance that one of these matches a resonance obviously increases. If these frequencies are not constant but vary according to operation conditions, which is the case in variable speed drives, the problem becomes overpowering. So, due to the rising demands and complexity, noise computation in electrical machines is a topic of high interest.

## 1.2 Review of literature

The noise emission of electrical machines can be traced back to different sources. One of the first detailed classifications is given in [29], a newer one in [90]. Besides mechanical sources, as for example bearings, rotor unbalance or the brushing, aerodynamic sources are listed there as well. The latter normally leads to broad band noise due to turbulence and separation of the flow of the cooling air. If, however, there is an object near the impeller, a pure tone, so-called siren noise, with a frequency proportional to its rotational speed, also may occur, which typically results in enormous sound pressure levels. A more detailed overview and computation methods for these sources can be found for example in [90], [75], [34].

A third source, and the one on which the focus of this thesis lies, is the noise of electromagnetic origin, i.e. one due to the electromagnetic forces acting on the machine and leading to vibrations. The electromagnetic forces can be split into forces due to magnetostrictive effect, Lorentz forces and electromagnetic force densities due to changes of the permeability. The latter ones are the largest at the surface of the teeth where the material changes from iron to air.

Early investigations presented in [38] and [8] have shown that magnetostrictive effects and the Lorentz forces on the conductors can be neglected as sources. Recent works regarding the magnetostrictive effect in the vibration analysis have been reported in [11]. Numerical computation results with and without using a magneto-mechanical coupling for considering magnetostriction, have been carried out and the results are compared with measurements of a mid-size synchronous generator and a small induction machine. This analysis shows that the influence of magnetostriction and the necessitiy of using a magneto-mechanical coupling is given for large machines with a thin stator yoke only, in particular the vibrations at lower frequencies increase in magnitude. Hence, the assumption of neglecting magnetostrictive effects and Lorentz forces is valid.

Methods to determine the forces due to the change of permeability are presented in [41]. A comparison of four different computation techniques (equivalent current density, equivalent magnetic charges, energy principle, Maxwell stress) to determine the electromagnetic force densities by numerical methods is given in [55]. A more recent investigation of the computation of the electromagnetic force densities has been carried out in [37] comparing the virtual work principle and the Maxwell stress tensor. The latter one is the most common technique in the noise computation process, especially in analytical approaches, whereas the first one is mainly applied in numerical techniques.

The computed forces can then be applied to a structural model where, besides an appropriate computation of the deformations and vibrations, especially the determination of the natural resonances is of importance. The vibrations again cause fluctuations in the surrounding air, which propagate with the sonic speed of air and thus result in audible noise. Again, especially in electrical machines, the occurring frequencies are in a range where the human ear is the most sensitive and this makes the noise investigation and elaboration of appropriate computation methods an important topic.

Summing up, the physical areas relevant for the generation of electromagnetically excited audible noise are electromagnetics, structural mechanics and acoustics, which have to be appropriately coupled. The magneto-mechanical coupling can be reduced to applying the surface forces computed with the Maxwell stress tensor method on the stator (and rotor) teeth. For the structural mechanics and acoustic field computation it is also sufficient to neglect the interaction of the sound pressure with the structure. Compared to the forces that act on the structure the occurring sound pressure has no influence on the forced vibrations, especially for exterior radiation problems. A detailed procedure for coupling the different physics is also given in [81], [13].

The further review of the literature on the investigation of the noise computation of electrical machines focuses on electromagnetic generated noise. The sequence is according to the different physics: starting with the computation of the electromagnetic fields, going on to the estimation of the structural response and then the computation of the noise radiation. Some comprehensive noise computation methods can be found in e.g. [42], [8], [65].

### 1.2.1 Electromagnetic field analysis in the noise computation process

This section covers a historical review regarding the electromagnetic field computation methods in conjunction with the noise estimation process, starting from analytical to numerical methods and further to state of the art methods combining the two.

One of the first discussions about the noise phenomena of induction machines is given by Hildebrand [38]. Similar to [19], he explains that problematic noise phenomena - he is dealing with induction machines - can be traced back to the air-gap field, i.e. higher harmonics due to the not ideally sinusoidal flux density distribution in the air-gap. He is one of the first to introduce the idea of decomposing the air-gap field into field components with distinct frequencies and spatial ordinal numbers and hence computing distinct force wave components acting on the stator as well as on the rotor teeth with the Maxwell stress tensor method. The decomposition is carried out by assigning the field components (and thus the force components) to their sources: magneto-motive force harmonics (stator, rotor) and permeance harmonics (stator and rotor slots, saturation, eccentricity etc.). Similar to [38] and [19], Morrill has also presented an approach based on the idea of decomposing the magnetic flux density in the air-gap into its harmonics [51]. His motivation was to set up the basis for fundamentals of a sound theory for noise computation in electrical machines. He started with a few assumptions, e.g. his approach did not consider permeance variations and their resulting harmonics, however the idea of decomposing the field and thus forces in wave components is the same and is one of the main advantages of analytical approaches in the noise computation process as it allows the assignment of critical noise peaks to their sources.

Hildebrand and Morrill, have both listed the force waves with different frequencies and spatial ordinal numbers related to the azimuthal direction and compared them to experimental data. However, as the focus has lain on the determination of the frequencies and spatial ordinal numbers, no determination of the magnetic field amplitudes has been men-

tioned. Furthermore, no approach to account for the structural response has been set up explicitly. Morrill for example "leaves this to future generations". Hildebrand only discusses the effects of the force waves on the structure and, contrary to [19] where the emitted noise is traced back to unbalanced magnetic pull, a resultant force acting on the rotor and on the stator, Hildebrand also speaks of a "polygonal distortion of the stator", as a source of noise of induction machines. This means that a force distribution with a distinct "pole-pair number" is resulting in relevant vibrations and leading to noise.

Some years later these ideas and approaches can also be found in one of the first comprehensive analytical procedures to determine the noise behaviour of induction machines presented in the work [42] by Jordan. In his methodology, he has defined categories, similar to [38], of the most relevant field harmonics and has set up computation rules to determine their amplitudes, spatial ordinal numbers, phases and frequencies. The appropriate force harmonics are then computed by using the Maxwell stress tensor method. His concept, including the structural and acoustic computations which will be explained later, allows the assignment of a distinct force component to the two magnetic field components involved and thus to a particular part of the machine and to its physical provenance. Appropriate measures, e.g. modifications of the structure to shift resonances or a different slot combination to change the excitation frequencies, can hence be investigated already in the design process. Further comprehensive analytical approaches are presented in [26] or [8], publications contemporary to [42]. However, they differ in the assumptions for the structural and acoustical computation as explained in the following sections. Regarding the computation of the magnetic field based on Jordan, more sophisticated methodologies are applied e.g. in [56]. A summary of the most important methodologies regarding the harmonic theory of rotating fields is presented in [68]. Techniques for the computation of different magnetic field components due to permeance variations like slotting, saturation, eccentricity are included as well as for those due to magneto-motive force waves including the consideration of the armature reaction.

Investigations regarding the force wave components resulting from magnetic fields computed with more sophisticated analytical approaches considering saturation and armature reaction, and a comparison with experimental vibration data, i.e. their spectral content, are shown in [82]. These analyses have been carried out for a squirrel cage induction motor and the measured vibration amplitudes are assigned in a very detailed manner to the causing magnetic force components and above all to the measured resonances. The aim has been to determine the role of the magnetic field harmonics on the forces and thus vibration. By comparing the computed and measured voltages, an overestimation of the amplitudes of the slot harmonics could be detected. The amplitudes of the computed saturation side-band component, however, are smaller than the measured ones. If the machine is loaded, the magneto-motive-force components in the rotor will increase similarly to the saturation effects. This leads to larger forces at the slot harmonic frequencies and in the saturation side-band. The measured vibrations have shown a 10 times larger amplitude of the slot harmonics compared to no-load operation.

The consideration of force waves for the structural computation is mostly confined to

those with lower spatial ordinal numbers and thus larger wave lengths, because those may lead to critical bending deformations of the stator yoke, as has also been stated in the previously presented investigations [42], [82]. In [97], explicit investigations of force wave components with different spatial ordinal numbers have been carried out. The focus lies on the analysis of forces with higher spatial ordinal numbers in the azimuthal direction. Applying such force waves on the teeth only, sub-harmonics occur, as there are no forces acting in the slots. Depending on the spatial ordinal number and the number of the teeth, those sub-harmonics may have large amplitudes and low spatial ordinal numbers and these can then again lead to large bending deformations of the stator yoke.

With the progress in numerical techniques, the finite element analysis has become a common tool in the computational treatment of electromagnetic field problems [20]. The main advantage of the finite element method is the possibility to set up more detailed models of electrical machines e.g. regarding the shape of the teeth. This, and the possibility to consider effects like eddy currents in the rotor bars and saturation, enables a more detailed evaluation of the magnetic field distribution in the machine. Furthermore, the results for the higher harmonic field components, especially the amplitudes, can be determined more accurately than by analytical methods.

Since the assignment of noise peaks to their sources is advantageous for noise computation and reduction purposes, similar approaches as with analytical methods have recently been applied to numerical simulations. In [43], the magnetic field in the air gap is obtained by a two-dimensional transient finite element simulation for the no-load operating point of an induction machine. The electromagnetic stress acting on the surface of the stator is then computed using the Maxwell stress tensor. Thereupon, the obtained stress distribution is decomposed into its harmonics and spatial ordinal numbers applying a two-dimensional Fourier analysis: according to time and the azimuthal direction. This method then enables the assignment of the force wave components to the arising noise peaks.

In [7], the numerically computed electromagnetic stress is also decomposed into its harmonics employing a two-dimensional Fourier decomposition and the force spectrum is compared to measured results of vibrations and noise of a loaded synchronous generator similar to [82]. The computed force wave components are then assigned to the measured vibration and noise peaks, however, without considering the structural response, i.e. the natural resonances, which may have influence on some noise peaks.

A more sophisticated method to obtain the assignment not only to the force wave components but also to the magnetic field components, as a result of a numerical simulation, is presented in [80]. By introducing a so-called space vector representation to describe the magnetic field and force waves by rotating vectors and by applying a two-dimensional Fourier transformation to the magnetic field, a description of the force wave components by a convolution pair of magnetic field space vectors is possible. Similar to [42], a cause and effect relationship is obtained, with higher accuracy of the computed amplitudes.

The electromagnetic field computation carried out in [65], [66] involves machines with skewing. This approach comprises a comprehensive noise computation approach. The electromagnetic machine model has been set up in 2D and the results have then been

applied to a three dimensional model to get the force distribution in the air-gap due to skewing in axial direction, too, to impress the forces on a three-dimensional structural finite element modelling.

However, such three-dimensional computations can be very time consuming, although computational resources increase from year to year. One possibility involving less computation time is to use a multi-slice model (see [24] and [57]) to determine the influence of the skewing on the magnetic field distribution in axial direction. This means, 2D finite element models each representing a slice of the machine at distinct axial positions are set up. For each slice the rotor has to be positioned according to the skewing angle and the currents in the rotor bars are coupled via an electric circuit model. This method requires less computational effort than three-dimensional simulations and provides a good means to determine the axial variation of the magnetic flux due to the skewing, which is of importance as the forces then also vary in axial direction and affect the structural vibrations. End effects and fluxes in axial direction cannot be taken into account with this model but these are negligible for noise computation purposes. Investigations on end-winding leakage and axial flux confirming this assumption are presented for example in [48].

The above numerical approaches belong to the state of the art computational techniques. However, analytical methods still play an important role in the noise computation process, as fast computations are possible. Their disadvantage is that they are not capable of predicting magnetic field amplitudes accurately. In [107], for example, the analytic determination of the magnetic field distribution in a brushless permanent magnet synchronous machine is improved by validating the results with numerical simulations. Moreover, in the design process of electrical machines, parameter studies have to be carried out to get the optimal construction. For this purpose, it is important that the problematic force components can be assigned to their sources and this has to be achieved in a reasonable time. Therefore, fast computational methods are required. In a recent work [46], the characterization and reduction of noise due to pulse width modulation (PWM) supply is carried out by analytical means and the switching frequency has been set so that the audible noise has decreased by 5dB. Another recent example is shown in [14]. There, the influence of the saturation on the magnetic noise is investigated by analytical means and by changing the number of rotor slots, the audible noise is reduced up to 15dB. Summing up, both analytical and numerical methods have their advantages in the noise computation process if applied properly, i.e. combinations of the two can lead to a considerable increase in efficiency.

### 1.2.2 Structural investigations

The early noise analyses of [38] and [19] are confined to the computation of the force wave components resulting from the magnetic fields. The design rules for slot configurations, skewing, etc. that have been set up to avoid critical forces do not consider the structural behaviour, i.e. the natural resonances of the stator, therefore these design rules are not applicable to an arbitrary machine design.

The structural modelling is probably the most problematic issue in the noise computa-

tion process. The complex assembly of an electrical machine with the stator as the crucial part directly exposed to the electromagnetic force requires enormous efforts in setting up appropriate models to determine the vibrational behaviour that leads to acoustic noise generation.

The following section lists the findings related to experimental investigations of the structural behaviour of the machine as well as analytical and numerical approaches to determine the structural responses.

As the stator is the part where the forces originating from the electromagnetic field act on, its modelling has been an important issue from the beginning of the noise investigations.

One of the first analytical models set up for the computation of the deformation amplitude on the back of the stator core stack has been set up by [42]. The stator has been considered as an infinitely long cylinder and the deformation in radial direction is determined according to force wave amplitude, frequency and wave number in azimuthal direction. The teeth of the stator are considered as additional mass distributed on the yoke. Such an approach is also possible when considering the windings, which may have significant influence on the structural behaviour. However, besides the confinement to a two-dimensional model, the housing and its coupling to the stator is not taken into account, which is also the case for a similar approach presented in [8].

Erdelyi criticizes the two-dimensional approaches and simplifications made by Jordan [42] and Alger [8]. He claims that there is more than one natural frequency in each mode of the stator core stack when mounted in the frame of the induction machine. Moreover, he maintains that the influence of the housing cannot be neglected, as it is the major part that radiates sound. In his work [26] he presents a comprehensive approach to determine the noise of polyphase induction motors of medium size, where the stator is mounted via ribs on the outer frame. He sets up an analytical model with the outer frame and the stator considered as cylindrical shells and connected via the ribs. The results of this investigation show that there exist four eigenfrequencies for each mode. The results proved to be good compared with measurements, however the presented general approach needs to be applied separately for different specific designs.

In [85], a frequency equation to determine not only the radial deformation but also torsional and axial vibration has been derived for stators encased tightly in the housing. In this computational approach, the displacements are assumed to be small and the stator core stack is regarded as a homogeneous and isotropic body. The windings and teeth are only considered as additional masses and their stiffening effect has been neglected. The forces obtained from electromagnetic field computations are applied to the structure as wave components with a distinct frequency, wave number and amplitude. The authors do not confine their model to describe only the two-dimensional vibration behaviour. Their focus also lies on the computation of deformations in axial direction. They stress the fact that, especially for long stators, the flexural bending cannot be neglected as, particularly for skewed machines, the forces acting on the machine vary in axial direction and thus cause axial bending of the stator. Several conclusions can be derived from their computational

results: first of all, the deformations in the different directions are coupled. This means that a radial force distribution does not necessarily lead to a purely radial deformation. The second point is that there exist several eigenfrequencies for a distinct modal pattern. These higher resonances may lie in the problematic frequency range - where the harmonics of the forces occur - especially in larger machines. The investigations of the influence of the frame have yielded that it affects the higher resonances and, moreover, the flexural vibrations.

In [84], the previously introduced approach is validated with experimental results. The natural resonances are measured and compared with the computational results. The computed and measured results for the eigenfrequencies of the different modes match very well, however, considering the teeth and windings as additional masses is not sufficient. Therefore, the approach has been supplemented by the use of Frohne's factors [29] considering the teeth as cantilever beams and a much better match has been achieved. This again implies that the teeth and windings influence the stiffness of the system.

As the determination of the eigenfrequencies of the stator is a crucial issue, detailed experimental investigations regarding the influence of teeth, winding, frame and lamination on the eigenfrequencies as well as on the amplitudes of vibration have been carried out in [35]. It is shown that the consideration of the windings as additional masses is not sufficient. Their contribution to the stiffness of the stator is large especially for higher modes. Teeth and winding combined act like an additional mass, whereas the frame and the lamination have only slight influence on the resonance frequencies. Regarding the vibration amplitudes, only the teeth lead to an increase. A decrease of the amplitudes is detected when considering winding, lamination and frame. The influence of the material damping has been investigated by analysing the steepness of the resonance peaks in the frequency response spectrum. It is shown that only the lamination causes damping, which can be very high especially for lower order modes.

Similar results have been delivered by [96]. Additionally, the influence of wedges, temperature and clamping pressure has been analysed. The latter only leads to a slight increase of the eigenfrequencies. The wedges, on the contrary, lead to a much more significant increase especially for higher modes. An increase of the temperature softens the structure and thus decreases the eigenfrequencies, which explains the different noise of "cold" and "warm" machines. The numerical computations involve an appropriate definition of the material parameters especially for the wedges and insulation of the windings. The results match very well with measurements.

Due to the obvious influence of winding and teeth on the stiffness of the structure a computational model of [85] incorporating the effect of teeth and windings has been introduced in [88], by Verma and Girgis. This is an extension to investigations of the same authors given in [36], [86] and [87], where the method is compared to solid thick models (no lamination). The purpose was to validate the modified method on short [71] and long stator models [106]. The examination of the influence of the length of the stator core stack on the eigenfrequencies showed no effect on the purely radial extensional modes. For long stators, variations of the radial vibrations in axial direction have been detected which con-

tribute significantly to the vibration behaviour. The analysis of an impregnated stator has shown an increase of the stiffness and a decrease of the damping of the winding. The resonances in the measured frequency response occur much sharper than without impregnation and the amplitudes are much larger. These effects have also been detected in more recent investigations regarding the influence of windings, frame and impregnation in [72].

Regarding the damping behaviour, analyses have shown that the laminations and windings have an influence on the damping of the structural system. An investigation to determine the amount of damping occurring in the structural vibration has been carried out in [83]. Distributed electro-magnetic forces are applied to the stator core with different dominant spatial ordinal numbers. The determined damping ratios [69] lie between 1% and 5% and are not proportional to the frequency, i.e. for different spatial ordinal numbers of the force waves a different damping occurs. Furthermore, the investigations have shown that all resonances are excited irrespectively of the force wave number. However, if the spatial ordinal number of the force is the same as the mode number at the resonance frequency, the vibrations are more critical.

The advantages and disadvantages of analytical methods compared to numerical techniques are similar to those in the electromagnetic field computation. Analytical approaches enable fast computations which are especially important in the design process and for parameter studies. With the finite element method, the complex structure of an electrical machine can be modelled more appropriately as more parts (stator, rotor and housing) can be considered. Their influence on the structural response can then be determined with numerical simulations either in the time-domain or in the frequency domain. However, as transients can be neglected and are seldom of interest for noise computation purposes, the evaluation of the structural deformation is usually performed in the frequency domain and the steady state solution is obtained. Transient solutions of previous electromagnetic field and force computations therefore also have to be transformed in the frequency domain. The natural resonances and eigenvectors are usually computed via a modal analysis for undamped structural systems. The visualized computed modes can give valuable information about the structural response expected.

A modal approach has been used to investigate the influence of windings and impregnation on the natural frequencies in [12] by applying the finite element method to different stator core stack models of a synchronous machine. The numerical computation results have shown that the influence of the impregnation on the eigenfrequency is enormous, i.e. high stiffening effect has been shown. However these results have not been verified with experimental investigations. A similar and more recent examination has been carried out in [40] where the influence of the end-windings and the frame has also been investigated in a finite element analysis. The results of the eigenfrequencies match the measured ones very well.

In [66], examinations of the stator to housing couplings have been determined by computing the structural response using numerical techniques and analytical means based on [42]. First of all, it is shown that the deformation amplitudes in radial direction of the 2D analytical and 3D numerical simulations agree very well. Furthermore, the investigation

of the coupling has shown that aliasing of the force waves occurs according to the number of springs coupling the stator and the frame. Models with three and six springs and one with a shrinked stator are compared; the model with six springs yields the best results.

An investigation that compared the three-dimensional finite element modelling to experimental results has been carried out in [92]. This analysis delivers important conclusions for further 3D vibration analyses using the finite element method, like considering the windings and teeth as a uniformly distributed mass results in sufficient accuracy. Furthermore, it is shown that the influence of the end-shields and the support of the machine is not negligible either, because new vibration modes occur. Actually, all parts of the machine contribute to the vibrations and should be modelled. Regarding the lamination it is stated that an orthotropic material model is absolutely necessary. The investigations have shown that a Young's modulus in axial direction should be set to $1\% - 2\%$ of that in circumferential direction to obtain proper results for the vibration. This has also been shown in an earlier investigation in [31].

In [31], laminated stacks have been investigated regarding their stiffness behaviour in axial direction. It has been shown that the Young's modulus and the shear moduli in this direction decrease significantly depending on the clamping pressure. Furthermore, the larger the clamping pressure, the lower is the damping.

Further examinations of the lamination have been carried out in [95] for different models with different number of laminates and different clamping pressures. The main result of this work is that the magnitude of the frequency response functions is lower than for the corresponding solid model. This is the case especially for modes with a characteristic in axial direction. These results are especially relevant for three-dimensional finite element simulations, since considering the core stack as solid steel brings poor results. Furthermore, the analysis of the occurring mode shapes have shown that the pure radial modes [94] are independent of the axial dimension, clamping pressure or number of laminates. The damping has not been investigated in this work. However the results shown for the frequency responses indicated the same behaviour as in the previous works.

The main challenge in the finite element simulations is therefore the adjustment of the material properties, especially of the laminated core stacks. An efficient way to setting these material properties is presented in [77]. There, experimental modal analyses have been carried out on a stator core stack after each fabrication step. Additionally, a finite element model has been set up and a corresponding homogenized equivalent material parameter set is determined by fitting the response of the simulation model to the measured one. The adjustment works well, as test cases have shown, too. However, the drawback of this approach is that the adjusted material parameter set is only valid for the particular model.

The determination of the structural response is typically carried out in the frequency domain as mentioned previously. Due to the complex structural modelling, the computational effort can be very demanding, requiring an enormous amount of memory and resulting in long computation times. To reduce computation time and memory demand, model reduction techniques like for example a modal decomposition can be carried out [28],[9] on the

one hand. Another possibility to decrease computational efforts is using the superposition principle valid for linear systems like those in structural vibration problems considered here. The structural response is computed for the relevant force wave components only, and the overall deformation can then be computed by scaling and superimposing these results. This idea has been adopted e.g. in [17] and validated for an interior permanent magnet synchronous machine. An extended investigation can be found in [16] which furthermore shows that azimuthal forces also cause a significant contribution to the vibrations. A similar approach is presented in [63] where this idea is applied to a rapid sound power calculation of electrical machines. However this examination focuses on squared responses, as the sound power is proportional to the square of the sound pressure, and thus has limited validity.

### 1.2.3 Acoustical investigations

The last step, after estimating the vibrations especially on the surface of the machine, is to determine the radiated noise caused by these vibrations. With analytical means the emitted sound pressure is computed by simplifying the structure to a substitute radiator. In [42], the machine has been considered as a spherical radiator with the same radius as the outer radius of the machine. The use of a more sophisticated cylindrical radiator has been proposed in [8], as the shape of an electrical machine typically resembles a cylinder. These approaches are still common in analytical computations, see e.g. [28], especially since they allow the computation of the effect of each vibration mode separately.

Similarly to electromagnetics and structural mechanics, the finite element method is a possible numerical means in acoustics, too [39]. However, an alternative and more common approach is the boundary element method [21], where only the surface and not the whole surrounding air has to be discretised, which is advantageous especially for higher frequencies, as the number of necessary elements for the finite element method increases enormously. The previously computed vibrations, i.e. the normal component of the surface velocity, is applied as boundary condition on the surface and, after solving the boundary integral equations, the sound pressure can be evaluated at distinct field points. This method is meanwhile commonly used in the noise computation process for electrical machines, see e.g. [65], [64], [78] or [30].

The experimental investigations comprise measurements of the sound pressure or the sound power at distinct points surrounding the machine. Typically, the spectral content is of importance for electrical machines. For different rotational speeds, the spectra have to be evaluated separately. In [91] the acoustic behaviour of an induction machine (the structural investigation has been presented in [92]) supplied with different inverters is measured for different rotational speeds. The aerodynamic and mechanical noise have been determined in a previous step to separate them from the totally emitted sound power and thus estimate the amount of the electromagnetic noise. These examinations have shown that the switching harmonics affect the noise spectrum very much, especially for lower speeds, where the electromagnetic noise is dominating. Furthermore it is shown that spe-

cific speeds excite structural resonances, which results in an increase of the total emitted sound power. The influence of the load is larger at lower speeds. Corresponding numerical examinations using the boundary element method are presented in [93]. A comparison with the measured sound power levels yields discrepancies, which however are accumulated errors of the electromagnetic and structural computations, due to neglecting for example the axial variation of the forces or the modelling the rotor, which influence especially the low frequency results.

A further very detailed experimental investigation is carried out in [89]. Besides vibration measurements on the stator to identify the structural behaviour, the noise has been measured at different positions around the investigated squirrel cage induction machine for different loads. The increase of the load on the machine leads to an increase in vibrations, however not in a linear way. The acoustic measurements have also shown an increase of the noise level, but not equally for all frequencies. Furthermore, directivity measurements in an anechoic room have been carried out to examine the direction of noise radiation. The results have shown different characteristics at different frequencies showing the influence of the structural behaviour determined by its eigenmodes on the noise emission.

A very recent work [76] presents a more sophisticated method to measure the emitted noise. The recording of the sound pressure has been carried out with an acoustic camera. This method enables the assignment of large sound pressure peaks to distinct locations and parts of the machine. The designated part was a cooling duct having an eigenfrequency at the excitation frequency. Combined with numerical structural computations this part has been modified by shifting the resonance frequencies leading to a decrease of emitted noise.

## 1.3 Contribution of this work

The computational techniques for determining the noise behaviour of electrical machines comprise analytical and numerical methods. The need for fast computation approaches accompanies the use of analytical means, e.g. in the design process. If a variation of parameters has to be carried out for optimization purposes, analytical methods would be appropriate tools, too. On the contrary, for investigations involving geometrical details or non-homogeneous materials of electrical machines numerical approaches suit better. So depending on the field of interest both techniques are still used in the noise computation process.

Usually, for the use of analytical methods, simpler models are considered, as for example the two-dimensional ring model for the vibration computation. The investigation of the validity and the limitations of a comprehensive analytical approach is one topic in this thesis. The analytical results are compared to data obtained by numerical computations as well as by vibration and noise measurements. The results are discussed in detail to outline the restrictions. This analyses have been presented at [100] and published in [101].

One limitation is for example disregarding the axial variations of the forces in the air-

gap. In the literature it is stated that "the vibro-acoustic response of a structure very much depends on the distribution of the excitation force" and "the electromagnetic force should be modelled three-dimensionally". Hence a novel method, presented at [102] and published in [105], that uses the results of a multi-slice simulation and then computes the rotating force wave components with axial variation has been established.

Furthermore, a phenomenon regarding higher order force waves is discussed. The decomposition of the air-gap field into its wave components and the following force computation using the Maxwell stress tensor method results in force wave components whose higher ordinal numbers are neglected in the vibration computation. This is valid, as the most critical bending occurs for small ordinal numbers. However, with appropriate slotting configurations, force waves with high spatial ordinal numbers and large amplitudes can occur. Moreover, these components only act on the teeth. Therefore the question arises what happens to these force waves when applied to the teeth. The contribution of these components to the vibration might be of interest. This phenomenon has been examined in the literature but has been disregarded in many publications until now. The investigations are carried out by structural numerical simulations on a three-dimensional model of an induction machine and have been presented at [103] and will be published in [104].

The different forces acting on the structure lead to different vibrations of an electrical machine. Therefore, the structural behaviour, i.e. the different vibrational behaviour of stator and surface is analysed in a further step. The correlation of the structural vibrations and the noise radiation is investigated. The focus thereby lies on the investigation of the vibration modes that occur, especially those on the housing, and how they contribute to the acoustic behaviour. In the scope of these analyses, which have been presented at [98] and published in [99], experimental investigations of different stator core stacks have been carried out with the aim of validating a homogenized orthotropic material model.

## 1.4 Outline of the work

In the first chapter the motivation for this work and a literature review of research related to noise computation of electrical machines is presented along with the state of the art methods (computational and experimental) regarding electromagnetic, structural and acoustic phenomena of electrical machines. Following that, the contributions of this work in the field of noise computation especially for induction machines are presented.

The next chapter presents the theoretical background of electromagnetic field, structural vibration and acoustic computations along with the fundamental equations for each. Chapter 3 then deals with the noise computation of electrical machines and presents a comprehensive analytic noise computation method. The focus lies on induction machines. The method first of all comprises the computation of the magnetic field harmonics occurring in the air gap. The causes for the different field harmonics and the resulting mechanical stresses are discussed in detail. After that, the structural vibration computation is presented

along with the determination of the noise radiation of an electrical machine assuming a cylindrical shape.

In chapter 4 the numerical means used for each physical phenomenon that has to be dealt with is presented. First of all, some principles of the finite element method are explained shortly. Following that, the electromagnetic field computation in electrical machines using the finite element method is presented. For structural vibration problems the finite element method can be applied, too, which is shown in the next section. Finally, the boundary element method is introduced for the computation of the noise radiation of vibrating structures.

Chapters 5 to 8 then deal with the topics presented in section 1.3. In chapter 5, the validation of the noise computation approach presented in chapter 3 is carried out. The analytic computation results are compared to numerical simulation results as well as experimental ones.

In chapter 6, a newly developed method to determine the variation of the magnetic field in the air gap using multi-slice models is presented. Computations have been performed for models with four and five slices for the nominal operating point of a squirrel cage induction machine and the reconstruction method is applied to both of them. In a last step, simulation results of a multi-slice model are compared with that of a three-dimensional model for the short circuit operating point.

Chapter 7 deals with the investigation of the structural behaviour of an electrical machine due to different stress wave components acting on it. Therefore, different stress wave components are defined and then applied to a three-dimensional structural finite element model. The outcome is discussed in detail.

The following chapter 8 presents a comprehensive vibration and acoustic noise computation of an induction machine using the numerical means explained in chapter 4. Special focus thereby lies on the investigation of the structural vibration behaviour and how it affects the noise radiation.

At last, chapter 9 presents a summary of the obtained results. The outcome along with the problems that have occurred are discussed and some aspects interesting for future work then conclude this work.

# 2 FUNDAMENTALS

## 2.1 Noise generation in electrical machines

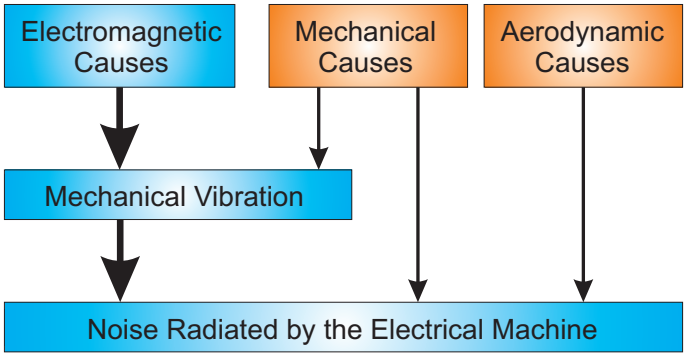


Figure 2.1: Causes of noise radiated by electrical machines

As mentioned in the introduction, the noise generation of electrical machines can be attributed to three main causes [29],[90],[75]. A schematic overview is depicted in Fig. 2.1. The aerodynamic causes comprise the pressure fluctuations due to the turbulences of the fluid flow of the cooling media. These pressure fluctuations are typically emitted directly as airborne noise (broadband noise). The mechanical causes include for example the bearings, the rotor imbalance or the brushes. The latter one, contrary to the first two, contributes directly to the noise generation. Owing to the low masses of bearings, they hardly produce any vibrations.

The focus of this work lies on the third cause of noise generation, i.e. electromagnetic phenomena. The electromagnetic fields especially in the air gap of electrical machines result in forces with a distinct spectral content causing structural vibrations. The magnitude of the vibrations depends, on the one hand, on the amplitudes of the forces, as is obvious, and on the other hand on the frequencies as they must not coincide with structural resonances. The surface oscillations then cause pressure fluctuations and thus a further energy conversion from vibrational to sound energy takes place. The spectral content of the emitted noise contains, on the one hand, the broad band noise of aerodynamic origin, and on the other hand noise peaks due to the electromagnetic forces. To account for humans' nonlinear perception of noise, the noise spectrum has to be rated with appropriate weighting curves.

In the following, the fundamentals to determine the governing quantities in each of the three domains - electromagnetics, mechanics and acoustics - are presented. For the electromagnetic domain, first of all, the governing equations to compute electromagnetic phe-

nomena, i.e. Maxwell's equations, are introduced. Maxwell's equations then are adapted for low frequency problems. Afterwards the determination of the forces that may arise from magnetic fields is explained. The fundamentals of mechanical problems comprise, first of all, the determination of the elastodynamic equations to compute the vibrations of an elastic body. In a next step coupled vibrations are investigated. A special focus hereby lies on the determination of the eigenvalues and eigenvectors and their contribution to the structural behaviour. The derivation of the governing equations for the acoustics concludes this chapter.

## 2.2 Electromagnetics

The phenomena of electromagnetic fields can be described with Maxwell's equations ([70], pp. 87-89). This is a set of equations that comprises Ampere's law, Faraday's law of induction and Gauss' laws given in the differential form as follows:

$$\nabla \times \mathbf{H} = \mathbf{J} + \frac{\partial \mathbf{D}}{\partial t}, \tag{2.1}$$

$$\nabla \times \mathbf{E} = -\frac{\partial \mathbf{B}}{\partial t}, \tag{2.2}$$

$$\nabla \cdot \mathbf{B} = 0, \tag{2.3}$$

$$\nabla \cdot \mathbf{D} = \rho. \tag{2.4}$$

In (2.1) Ampere's law extended by Maxwell's term $\frac{\partial \mathbf{D}}{\partial t}$ for time dependent conditions is given. A circulating magnetic field intensity $\mathbf{H}$ thereby results from a current density $\mathbf{J}$ and the current density obtained as the time derivative of the displacement $\mathbf{D}$. Equation (2.2) denotes Faraday's law meaning that the variation of a magnetic field $\mathbf{B}$ with time results in a circulating electric field $\mathbf{E}$.

Equations (2.3) and (2.4) denote Gauss' laws for magnetic and electric fields. An electric displacement $\mathbf{D}$ produced by electric charges (charge density $\rho$) diverges from positive charges and converges to negative charges. The divergence of the magnetic flux density $\mathbf{B}$ at any point is zero. The total (net) magnetic flux through a closed surface is thereby zero.

The given relationships are of general validity and independent from any material properties. However, the vectors can be related among each other depending on the material properties as follows:

$$\mathbf{D} = \varepsilon \mathbf{E}, \qquad \mathbf{B} = \mu \mathbf{H}, \qquad \mathbf{J} = \gamma (\mathbf{E} + \mathbf{E}_e). \tag{2.5}$$

The parameters $\varepsilon$ and $\mu$ are the electric permittivity and the magnetic permeability denoting the material's response to an electric and magnetic field, respectively. Usually $\varepsilon = \varepsilon_r \varepsilon_0$ and $\mu = \mu_r \mu_0$ is introduced, where $\varepsilon_0 = 8.8543 \cdot 10^{-12}$ F/m and $\mu_0 = 4\pi \cdot 10^{-7}$ H/m are the permittivity and permeability in vacuum and $\varepsilon_r$ and $\mu_r$ denote dimensionless constants of different materials related to vacuum. $\gamma$ is the conductivity of a material and $\mathbf{E}_e$ denotes an imposed electric field.

### 2.2.1 Quasi-static fields

For applications like electrical machines, Maxwell's equations can be simplified to the quasi-static limit by neglecting the displacement current density in (2.1), since

$$|\mathbf{J}| \gg \left|\frac{\partial \mathbf{D}}{\partial t}\right| \tag{2.6}$$

for the occurring frequencies, e.g. at $f = 20\,\text{kHz}$

$$\frac{|\mathbf{J}|}{|j2\pi f \mathbf{D}|} \approx 8 \cdot 10^{12}. \tag{2.7}$$

Two sets of equations can now be defined, one for the non-conducting region $\Omega_n$ and one for the conducting region $\Omega_c$. In $\Omega_c$ the current density $\mathbf{J}$ is unknown and an eddy current field is present. Therefore, Faraday's law has to be considered. In $\Omega_n$ a current density $\mathbf{J}_0$ is given[1]. The following set of differential equations then is obtained:

$$\nabla \times \mathbf{H} = \mathbf{J} \qquad \text{in } \Omega_c \tag{2.8}$$

$$\nabla \times \mathbf{E} = -\frac{\partial \mathbf{B}}{\partial t} \qquad \text{in } \Omega_c \tag{2.9}$$

$$\nabla \times \mathbf{H} = \mathbf{J}_0 \qquad \text{in } \Omega_n \tag{2.10}$$

$$\nabla \cdot \mathbf{B} = 0 \qquad \text{in } \Omega_c, \Omega_n \tag{2.11}$$

$$\mathbf{J} = \gamma \mathbf{E} \qquad \text{in } \Omega_c \tag{2.12}$$

The outer boundaries of $\Omega_c$ and $\Omega_n$ shall be denoted by $\Gamma_c$ and $\Gamma_n$ and homogeneous boundary conditions shall be assumed. If $\Gamma_c$ and $\Gamma_n$ are symmetry planes or artificial far boundaries we have the following boundary conditions:

$$\mathbf{H} \times \mathbf{n} = \mathbf{0} \quad \text{or} \quad \mathbf{E} \times \mathbf{n} = \mathbf{0} \qquad \text{on } \Gamma_c \tag{2.13}$$

$$\mathbf{H} \times \mathbf{n} = \mathbf{0} \quad \text{or} \quad \mathbf{B} \cdot \mathbf{n} = \mathbf{0} \qquad \text{on } \Gamma_n \tag{2.14}$$

where $\mathbf{n}$ is the outer normal unit vector. On the symmetry plane either the tangential components of $\mathbf{H}$ or $\mathbf{E}$ is zero. On the far boundary of the non-conducting domain $\Omega_n$ either the normal component of $\mathbf{B}$ or the tangential component of $\mathbf{H}$ is zero. On the interface $\Gamma_{nc}$ of the two regions $\Omega_n$ and $\Omega_c$ $\mathbf{H} \times \mathbf{n}$ and $\mathbf{B} \cdot \mathbf{n}$ are continuous. Applying these boundary conditions to the quasi-static equation system (2.8) to (2.12) yields a unique solution. However, analytical approaches only exist for simple geometries and problem definitions. For more complicated models numerical means are necessary to solve quasi-static problems, which will be introduced in section 4.3.

[1] The skin effect problem is neglected here. The current is assumed to flow in coils with cross sections smaller than the penetration depth.

## 2.3 Electromagnetic forces

In the scope of this work the forces $\mathbf{F} = q\mathbf{E}$ on electrical charges $q$ provoked by an electric field $\mathbf{E}$ shall be neglected. Only those forces due to a magnetic field shall be investigated. The derivation shown here is based on the approach presented in [18].

A magnetic flux density $\mathbf{B}(\mathbf{r})$ and a magnetic field intensity $\mathbf{H}(\mathbf{r})$ shall be defined at a position $\mathbf{r}$. Assuming linear magnetic material properties, the magnetic energy density $w_m(\mathbf{r}, \mathbf{B}(\mathbf{r}))$ is then defined as follows:

$$w_m(\mathbf{r}, \mathbf{B}(\mathbf{r})) = \int_0^{\mathbf{B}} \mathbf{H} \cdot \mathrm{d}\mathbf{B} = \frac{1}{2} \mathbf{H} \cdot \mathbf{B}. \tag{2.15}$$

Introducing a uniform vector field $\mathbf{v}$, the following identity can be obtained [18]:

$$\boldsymbol{\nabla} \cdot (\mathbf{B}(\mathbf{H} \cdot \mathbf{v}) - w_m \mathbf{v}) \equiv \mathbf{v} \cdot (\boldsymbol{\nabla} \times \mathbf{H} \times \mathbf{B} + \mathbf{H} \boldsymbol{\nabla} \cdot \mathbf{B} - \boldsymbol{\nabla} w_m). \tag{2.16}$$

A domain $\Omega$ with its bounding surface $\Gamma$ and the outward normal $\mathbf{n}$ shall now be defined. Inserting $\boldsymbol{\nabla} \times \mathbf{H} = \mathbf{J}$ and $\boldsymbol{\nabla} \cdot \mathbf{B} = 0$ into (2.16), using $\mathbf{B}(\mathbf{H} \cdot \mathbf{v}) = (\mathbf{B} \otimes \mathbf{H})\,\mathbf{v}$ and dropping $\mathbf{v}$ results in:

$$\int_\Omega \boldsymbol{\nabla} \cdot (\mathbf{B} \otimes \mathbf{H} - w_m \mathbf{I}) \mathrm{d}\Omega = \int_\Omega (\mathbf{J} \times \mathbf{B} - \boldsymbol{\nabla} w_m) \mathrm{d}\Omega = \mathbf{F}, \tag{2.17}$$

where $\mathbf{I}$ is the unit tensor. The right-hand side is the total force $\mathbf{F}$ acting on a volume $\Omega$ and it contains a volume force density with two terms. The first one stands for the Lorentz-force, the force on a given current density in a magnetic field. The second term is the force density due to the variation of the energy density. The gradient is especially large on the surface of highly permeable materials surrounded by air. This is the case in electrical machines where the magnetic field passes the air gap from the stator to the rotor.

If the permeabiltiy $\mu$ depends on the strain $\varepsilon$ of the material, which is the definition for magnetostriction according to [18], a further energy term $\Psi(\varepsilon, \mathbf{B})$ arises. This results in a strongly coupled problem of the magnetic and elastic energy. However, for the scope of this work the magnetostrictive effects can be neglected. As has also been shown in [11] those forces do not contribute significantly to the vibration behaviour of electrical machines except for machines with large stators and thin yokes.

The volume force density on the right hand side of (2.17) motivates the introduction of a stress tensor $\overline{\mathbf{T}}$ for the tensor on the left hand side. This is also referred to as the Maxwell stress tensor. Using (2.15):

$$\overline{\mathbf{T}} = \mathbf{B} \otimes \mathbf{H} - \frac{1}{2} (\mathbf{B} \cdot \mathbf{H})\, \mathbf{I}. \tag{2.18}$$

With Gauss' law, the total force $\mathbf{F}$ arising from a magnetic field and acting on a volume can now be determined via the Maxwell tensor $\overline{\mathbf{T}}$:

$$\mathbf{F} = \int_{\Omega} \nabla \cdot \overline{\mathbf{T}} \mathrm{d}\Omega = \oint_{\Gamma} \overline{\mathbf{T}} \mathbf{n} \mathrm{d}\Gamma. \tag{2.19}$$

The expression of the Maxwell tensor in (2.18) can be written as:

$$\overline{\mathbf{T}} = \begin{bmatrix} (B_x H_x - \frac{1}{2}\mathbf{B}\cdot\mathbf{H}) & B_x H_y & B_x H_z \\ B_y H_x & (B_y H_y - \frac{1}{2}\mathbf{B}\cdot\mathbf{H}) & B_y H_z \\ B_z H_x & B_z H_y & (B_z H_z - \frac{1}{2}\mathbf{B}\cdot\mathbf{H}) \end{bmatrix}. \tag{2.20}$$

Using the identity $(\mathbf{B}\otimes\mathbf{H} - w_m\mathbf{I})\cdot\mathbf{n} = (\mathbf{n}\cdot\mathbf{B})\mathbf{H} - w_m\mathbf{n}$, a surface force density $\boldsymbol{\sigma}_m$ can hence be defined as:

$$\boldsymbol{\sigma}_m = \overline{\mathbf{T}}\mathbf{n} = (\mathbf{n}\cdot\mathbf{B})\mathbf{H} - \frac{1}{2}(\mathbf{B}\cdot\mathbf{H})\mathbf{n}. \tag{2.21}$$

With this relationship, the force acting on an arbitrary surface element $\mathrm{d}\Gamma$ can therefore be determined as $\mathrm{d}\mathbf{F} = \boldsymbol{\sigma}_m \mathrm{d}\Gamma$. As outlayed in [18], the Maxwell tensor is valid for problems where no magnetostrictive effects are present. The location of the surface $\Gamma$ is arbitrary and can also cut through magnetized matter. Furthermore, non-linear *B*-*H* curves are allowed. The application of the Maxwell stress tensor to electrical machines is presented in section 3.1.4.

## 2.4 Structural mechanics

### 2.4.1 Equation of elastodynamic equilibrium

The structural vibration investigation of a deformable body implies the set up of an appropriate model based on the theory of elasticity and dynamical principles. Typically, the body is assumed to be a continuum, i.e. a continuous entity with homogeneous material properties. First the kinematics i.e. the displacements of the material points comprising the body are investigated. Then the constitutive laws for linear elastic problems are introduced and the equation of an elasto-dynamic body are set up. The following derivations can also be found in [73], [67] and [59].

**Kinematics of a continuum** A point $P$ of a deformable body $B$ shall be defined in the coordinate system $R$ with the basis $({}_R\mathbf{e}_1, {}_R\mathbf{e}_2, {}_R\mathbf{e}_3)$ with the initial position vector $\mathbf{r}$ at time $t = t_0$ and the actual position vector $\mathbf{R}$ at time $t$, i.e. by a Lagrange representation ([67], pp. 19). The displacement vector $\mathbf{s}$ of the deformed volume element $\mathrm{d}\Omega$ from $t_0$ to $t$ is then defined as follows:

$$\mathbf{s}(\mathbf{r},t) = \mathbf{R}(\mathbf{r},t) - \mathbf{r}. \tag{2.22}$$

The displacement vector $\mathbf{s}$ contains, on the one hand, the information about the change of the position and orientation compared to $t_0$, which describes the rigid body movement $\mathbf{s}_R$ of $B$ and, on the other hand, the information about the change of its shape $\mathrm{d}\Omega|_{t_0} \rightarrow \mathrm{d}\Omega|_t$, i.e. the deformation $\mathbf{s}_D$ and, therefore, $\mathbf{s} = \mathbf{s}_D + \mathbf{s}_R$.

Let $({}_B\mathbf{e}_1, {}_B\mathbf{e}_2, {}_B\mathbf{e}_3)$ be defined as the basis of the deformed body $B$ with coordinates $\mathbf{x} = (x_1, x_2, x_3)$ and $({}_R\mathbf{e}_1, {}_R\mathbf{e}_2, {}_R\mathbf{e}_3)$ with coordinates $\boldsymbol{\xi} = (\xi_1, \xi_2, \xi_3)$) shall move with the body (no rigid body movement terms for the displacement).

To determine the change of shape of the body $B$, the difference of the squares of the infinitesimal arc elements $\mathrm{d}\boldsymbol{\xi}$ for the actual configuration and $\mathrm{d}\mathbf{x}$ for the initial one is taken:

$$\mathrm{d}S^2 = \mathrm{d}\boldsymbol{\xi} \cdot \mathrm{d}\boldsymbol{\xi}, \qquad \mathrm{d}s = \mathrm{d}\mathbf{x} \cdot \mathrm{d}\mathbf{x}, \tag{2.23}$$

$$\frac{\mathrm{d}S^2 - \mathrm{d}s^2}{2} = \mathrm{d}\mathbf{x} \cdot \overline{\mathbf{G}} \cdot \mathrm{d}\mathbf{x} \tag{2.24}$$

where $\overline{\mathbf{G}}$ denotes the Green-Lagrange strain tensor and is determined in the following way:

$$\overline{G}_{ij} = \frac{1}{2}\left(\frac{\partial \xi_i}{\partial x_j} + \frac{\partial \xi_j}{\partial x_i} + \sum_{m=1}^{3} \frac{\partial \xi_m}{\partial x_i}\frac{\partial \xi_m}{\partial x_j}\right) \qquad i, j, \ldots 1, 2, 3. \tag{2.25}$$

**Linear elastic theory** For most practical applications simplifications regarding the structural behaviour, i.e. a linearisation of the previously presented kinematics, can be made. Therefore, the partial derivatives in (2.25) are assumed to be very small and the non-linear terms of $\overline{\mathbf{G}}$ are neglected. The components $\varepsilon_{ij}$ with $i, j = 1, 2, 3$ of the Green-Lagrange strain tensor can now be obtained in the following way

$$\varepsilon_{ij} = \frac{1}{2}\left(\frac{\partial \xi_i}{\partial x_j} + \frac{\partial \xi_j}{\partial x_i}\right), \qquad i, j = 1, 2, 3. \tag{2.26}$$

**Stress-strain relationship - Hooke's law** The stress and strain state in a deformable body $B$ is coupled via the material properties of the medium. Assuming a linear stress-strain relationship according to Hooke's law results in:

$$\sigma_{ij} = \lambda \boldsymbol{\nabla} \cdot \boldsymbol{\xi}\, \delta_{ij} + 2G\varepsilon_{ij} \qquad i, j = 1, 2, 3 \tag{2.27}$$

where $\lambda$ is Lamé's first parameter and $\delta_{ij}$ denotes the Kronecker symbol. The material constants defining $\lambda$ are the Young's modulus $E$ and the Poisson ratio $\nu$, see (2.28). Those constants also define the parameter $G$, also known as the shear modulus as it relates the shear strains and stresses:

$$\lambda = \frac{E\nu}{(1+\nu)(1-2\nu)} \qquad G = \frac{E}{2(1+\nu)} \tag{2.28}$$

**Equation of elastodynamic equilibrium** The presented relationships for an elastic body result in 15 unknowns and therefore 15 equations are to be set up in an elastodynamic problem. The strain tensor relates the displacements and the strains and results in six equations and further six are obtained with Hooke's Law relating the stresses and the strains. The last three equations are obtained with the basic law of continuum mechanics.

Newton's second law states that the change of the momentum with time equals the resulting (net) force acting on the body $B$. The total acceleration $\mathbf{a}$ is determined with respect to an inertial system as the second total time derivative of the displacement vector $\mathbf{s}$:

$$\mathbf{a} = \frac{d^2\mathbf{s}}{dt^2}. \tag{2.29}$$

With the local displacement vector $\boldsymbol{\xi}$ (for rigid body movement $\boldsymbol{\xi} = [0,0,0]$) a local acceleration $\mathbf{a}_L$ can be defined as the second local time derivative of $\boldsymbol{\xi}$:

$$\mathbf{a}_L = \frac{\partial^2\boldsymbol{\xi}}{\partial t^2}. \tag{2.30}$$

Let us assume that no rigid body movement occurs and, because of the assumption of small displacements, the inertia forces are determined by the local acceleration $\mathbf{a}_L$ only. Consider now an infinitesimal volume element with density $\rho$ and a volume force $\mathbf{f}_B$ acting on it, then, according to Cauchy's law, the following equilibrium with the inertia force $\rho\mathbf{a}_L$ and the stresses $\sigma_{ij}$ on the cut surfaces is obtained:

$$\boldsymbol{\nabla}\cdot\overline{\boldsymbol{\sigma}} + \mathbf{f}_B = \rho\frac{\partial^2\boldsymbol{\xi}}{\partial t^2} \tag{2.31}$$

where $\overline{\boldsymbol{\sigma}}$ is a symmetrical second order tensor containing the stress components $\sigma_{ij}$. For small values of $\frac{\partial\xi_i}{\partial x_i}$, $\frac{\partial\sigma_{ij}}{\partial x_i} = \frac{\partial\sigma_{ji}}{\partial\xi_i}$ holds ([59], pp. 175),([22], pp. 28). Therefore, using Lagrange's representation in the actual configuration is equivalent to using Euler's representation in the reference coordinate system ([67], pp. 79). Inserting (2.26) and (2.27) the following relationship can be obtained:

$$G\Delta\boldsymbol{\xi} + (\lambda+G)\boldsymbol{\nabla}(\boldsymbol{\nabla}\cdot\boldsymbol{\xi}) + \mathbf{f}_B = \rho\mathbf{a}_L = \frac{\partial^2\boldsymbol{\xi}}{\partial t^2} \tag{2.32}$$

This is the general differential equation for elastic oscillatory motions. It is of second order with respect to space and time with the displacement vector $\boldsymbol{\xi}$ as its argument. On the left hand side two operators appear. This indicates that (2.32) comprises two wave equations simultaneously. Introducing a scalar and vector potential for the divergence-free and irrotational part of $\boldsymbol{\xi}$ (Helmholtz decomposition):

$$\boldsymbol{\xi} = \boldsymbol{\nabla}\Phi + \boldsymbol{\nabla}\times\boldsymbol{\Psi} \tag{2.33}$$

allows, for the homogeneous part ($\mathbf{f}_B = 0$), the formulation of two wave equations with different wave numbers $k_\alpha$ and $k_\beta$

$$\frac{d^2\Phi}{dt^2} + {k_\alpha}^2 \Delta\Phi = 0, \tag{2.34}$$

$$\frac{d^2\boldsymbol{\Psi}}{dt^2} + {k_\beta}^2 \Delta\boldsymbol{\Psi} = \mathbf{0}. \tag{2.35}$$

The solution for the elastodynamic problem can thereby be split into a wave equation for longitudinal waves (2.34) and one for transversal waves (2.35) ([22], pp.74-88), ([73], pp.94-96).

### 2.4.2 n-degree of freedom mechanical system

Consider now a multi body system with $n$ degrees of freedom. With the application of the Euler-Lagrange equations ([45], pp. 60ff) one obtains the following general equation of motion for a non-linear multi body system ([69], pp. 188ff):

$$\mathbf{M}(\overline{\mathbf{q}}, t)\ddot{\overline{\mathbf{q}}} + \mathbf{k}(\overline{\mathbf{q}}, \dot{\overline{\mathbf{q}}}, t) = \mathbf{F}(\overline{\mathbf{q}}, \dot{\overline{\mathbf{q}}}, t). \tag{2.36}$$

In this equation $\mathbf{q}$ is an $n$-dimensional vector of the generalized coordinates. $\mathbf{M}$ is the symmetric $[n \times n]$ mass matrix of the system. $\mathbf{k}$ is the gyroscopic force vector of the dimension $[n \times 1]$ and $\mathbf{F}$ is the $[n \times 1]$ vector of the generalized forces.

Performing a linearisation around a position of equilibrium $\mathbf{q}_S(t)$ with $\overline{\mathbf{q}}(t) = \mathbf{q}_S(t) + \mathbf{q}(t)$, the following equation of equilibrium is obtained:

$$\mathbf{M}(t)\ddot{\mathbf{q}}(t) + \mathbf{P}(t)\dot{\mathbf{q}}(t) + \mathbf{Q}(t)\mathbf{q}(t) = \mathbf{F}(t). \tag{2.37}$$

The vector $\mathbf{q}$ denotes the displacements around the position of equilibrium $\mathbf{q}_S$. The gyroscopic forces $\mathbf{k}$ are now described by the sum of the product of $\mathbf{P}(t)$ with the velocity vector $\dot{\mathbf{q}}$ and of $\mathbf{Q}(t)$ with the displacement vector $\mathbf{q}$. $\mathbf{P}$ and $\mathbf{Q}$ are $[n \times n]$ matrices containing the information of the gyroscopic effects and the coupling of the bodies. If the matrices are constant and gyroscopic effects are neglected then the following differential equation of second order is obtained:

$$\mathbf{M}\ddot{\mathbf{q}} + \mathbf{D}\dot{\mathbf{q}} + \mathbf{K}\mathbf{q} = \mathbf{F}(t). \tag{2.38}$$

In this equation $\mathbf{D}$ denotes a symmetric $[nxn]$ matrix called damping matrix and $\mathbf{K}$ is also a symmetric $[n \times n]$ matrix and is referred to as stiffness matrix. The first term on the left hand side determines the kinetic energy of the system and the one with the stiffness matrix $\mathbf{K}$ the potential energy. The damping matrix $\mathbf{D}$ determines the dissipation occurring in the mechanical system and thus leads to a non-conservative system.

The same equation of motion can be derived for an elastodynamic system in (2.32), if for example the Ritz method is applied to it [33]. A special application of the Ritz method

realized by the finite element method is presented in the chapter 4.4. The investigated body is discretized with finite elements consisting of nodes that correspond to mass points. The connection of the nodes can be imagined as springs with stiffness according to the material properties.

**Solution in frequency domain** For structural vibration problems, typically stationary investigations are of interest, where the external force $\mathbf{F}$ is a harmonic function with a frequency $\Omega$ and an amplitude $\hat{\mathbf{F}}$. If the investigated problem is asymptotically stable ([69], pp. 205), then the transient oscillations can be neglected, since the homogeneous solution decays. Only the particular solution remains. Therefore, (2.38) can be transformed in the frequency domain and the following equation is gained:

$$(-\Omega^2\mathbf{M} + j\Omega\mathbf{D} + \mathbf{K})\hat{\mathbf{q}} = \hat{\mathbf{F}}. \tag{2.39}$$

This leads to a steady-state problem where the displacement vector $\hat{\mathbf{q}}$ is determined by

$$\hat{\mathbf{q}} = (-\Omega^2\mathbf{M} + j\Omega\mathbf{D} + \mathbf{K})^{-1}\hat{\mathbf{F}} \tag{2.40}$$

**Modal transformation** Regarding the undamped system only, a so-called modal transformation of the mechanical system can be carried out for quadratic and symmetric system matrices $\mathbf{M}$ and $\mathbf{K}$ [32],[33]. To this end, the homogeneous undamped part of equation (2.38) is considered:

$$\mathbf{M}\ddot{\mathbf{q}} + \mathbf{K}\mathbf{q} = 0 \tag{2.41}$$

and the eigenvalues $\lambda_i$ and the eigenvectors $\mathbf{r}_i$ are computed. The homogeneous solution can now be obtained as a linear combination of the eigenvectors with the coefficients $z_i$ $i = 1, 2, \ldots, n$:

$$\mathbf{q}(t) = \sum_{i=1}^{n} \mathbf{r}_i z_i(t). \tag{2.42}$$

The eigenvectors $\mathbf{r}_i$ can be arranged in a matrix $\mathbf{R}$, the so-called modal matrix. Furthermore a new displacement vector $\mathbf{z}$ containing the modal coordinates $z_i$ can be set up and a transformation of the modal coordinates to the original coordinates with the modal matrix $\mathbf{R}$ can be carried out:

$$\mathbf{q}(t) = \mathbf{R}\mathbf{z}(t). \tag{2.43}$$

Inserting this relationship into (2.40) with no damping ($\mathbf{D} = \mathbf{0}$) and multiplying with the transposed modal matrix from the left results in

$$\hat{\mathbf{q}} = (-\Omega^2\mathbf{R}^T\mathbf{M}\mathbf{R} + \mathbf{R}^T\mathbf{K}\mathbf{R})^{-1}\mathbf{R}^T\hat{\mathbf{F}} \tag{2.44}$$

or, with the following orthogonality properties

$$\mathbf{R}^T\mathbf{M}\mathbf{R} = \mathbf{I} \qquad \mathbf{R}^T\mathbf{K}\mathbf{R} = diag(\omega_i^2) \tag{2.45}$$

one obtains

$$\hat{\mathbf{q}} = \left(-\Omega^2\mathbf{I} + diag(\omega_i^2)\right)^{-1}\mathbf{R}^T\hat{\mathbf{F}}. \tag{2.46}$$

It can be seen in (2.46) that the solution of the displacement vector $\mathbf{x}$ is determined by two terms. One is the product of the transposed modal matrix with the excitation force vector. This results in a vector whose entries $i$ are zero if the force vector $\hat{\mathbf{F}}$ is orthogonal to the eigenvectors $\mathbf{r}_i$. The second term is determined by the inverse of the difference of the excitation frequency $\Omega$ and the eigenfrequencies $\omega_i$. The entries therefore are large for excitation frequencies near the eigenfrequencies.The eigenvectors corresponding to eigenvalues near the excitation frequencies therefore dominate the displacement vector $\hat{\mathbf{q}}$.

For damped systems, a similar derivation is possible as long as the damping matrix is constructed accordingly i.e. as a linear combination of the mass and stiffness matrices. Then, the eigenvectors stay the same and are orthogonalized with respect to the damping matrix ([69], pp. 202-204).

## 2.5 Acoustics

Acoustic media are typically homogeneous, inviscid and irrotational fluids and shall be defined in a domain $\Omega$. The acoustic fluid with the density $\overline{\rho}$ shall move with a velocity $\mathbf{v}$. The law of continuity therefore is as follows ([73], pp. 83ff):

$$\frac{\partial\overline{\rho}}{\partial t} + \boldsymbol{\nabla}\cdot\rho\mathbf{v} = 0. \tag{2.47}$$

The pressure $p$ is acting on the acoustic medium and, furthermore, for the sake of generality, an external volume force vector $\mathbf{f}$ (external source) shall be given. The equation of motion can now be obtained with Euler's equation for non-viscous fluids:

$$\rho\frac{d\mathbf{v}}{dt} + \boldsymbol{\nabla}\overline{p} = \mathbf{f}. \tag{2.48}$$

For the further derivations, the external sources $\mathbf{f}$ shall be omitted. For acoustical investigations, only small vibrations in the air are typically of interest. So, the total derivative $\frac{d\mathbf{v}}{dt}$ can be replaced by the partial derivative $\frac{\partial\mathbf{v}}{\partial t}$. Furthermore, a linearisation of the density $\overline{\rho}$ and the pressure $\overline{p}$ around the nominal atmospheric values $\rho_0$ and $p_0$ can be carried out:

$$\overline{\rho} = \rho_0 + \rho, \qquad \overline{p} = p_0 + p. \tag{2.49}$$

Neglecting higher order terms, this results in

$$\frac{\partial\rho}{\partial t} + \rho_0\boldsymbol{\nabla}\cdot\mathbf{v} = 0, \tag{2.50}$$

$$\rho_0\frac{\partial\mathbf{v}}{\partial t} + \boldsymbol{\nabla}p = 0. \tag{2.51}$$

The relation of the pressure $p$ and the density $\rho$ can be expressed by the thermodynamic laws for polytrope behaviour. However, typically adiabatic conditions are assumed for acoustic investigations which results in a linear relation of the sound pressure and the density:

$$\boldsymbol{\nabla} p = \left(\frac{\partial p}{\partial \rho}\right)_0 \boldsymbol{\nabla}\rho = c^2 \boldsymbol{\nabla}\rho \tag{2.52}$$

where $c = \sqrt{\kappa R T}$ is the sound velocity in air.

Multiplying (2.51) with $\nabla$ from the left, differentiating (2.50) with respect to time $t$ and using (2.52) results in the wave equation for acoustic fluids in the time domain:

$$\Delta p(\mathbf{r},t) - \frac{1}{c^2}\frac{\partial^2 p}{\partial t^2}(\mathbf{r},t) = 0 \tag{2.53}$$

where $\mathbf{r}$ denotes the position of a point in $\Omega$. For stationary conditions, a Fourier transformation can be performed and the Helmholtz equation is obtained:

$$\Delta\hat{p}(\mathbf{r}) + k^2\hat{p}(\mathbf{r}) = 0. \tag{2.54}$$

where $k = \frac{\omega}{c}$ is the wave number for the angular frequency $\omega$. The solutions for the sound pressure $p$ and the sound particle velocity $\mathbf{v}$ are then determined with:

$$p(t) = \mathrm{Re}(\hat{p}e^{j\omega t}), \qquad \mathbf{v}(t) = \mathrm{Re}(\hat{\mathbf{v}}e^{j\omega t}). \tag{2.55}$$

As the pressure is a scalar quantity, these wave equations determine longitudinal waves, cf. (2.34). Let $\Gamma$ be the surface enclosing $\Omega$ with the unit normal direction $\mathbf{n}$. Normal components are denoted by the subscript $n$. The following Dirichlet boundary conditions on $\Gamma_d$, Neumann boundary conditions on $\Gamma_n$ and mixed boundary conditions on $\Gamma_r$ can be defined:

$$\hat{p}(\mathbf{r}) = \overline{p}(\mathbf{r}), \qquad \mathbf{r} \in \Gamma_d \tag{2.56}$$

$$\hat{v}_n(\mathbf{r}) = \frac{j}{\rho_0\omega}\frac{\partial\hat{p}(\mathbf{r})}{\partial n} = \overline{v}_n(\mathbf{r}), \qquad \mathbf{r} \in \Gamma_n \tag{2.57}$$

$$\hat{p}(\mathbf{r}) = \overline{Z}(\mathbf{r})\hat{v}_n(\mathbf{r}) = \frac{j}{\rho_0\omega}\overline{Z}(\mathbf{r})\frac{\partial\hat{p}(\mathbf{r})}{\partial n}, \qquad \mathbf{r} \in \Gamma_r \tag{2.58}$$

where $\overline{p}(\mathbf{r})$ and $\overline{v}_n(\mathbf{r})$ denote prescribed functions for the sound pressure and sound particle velocity on the surface. The normal impedance boundary condition $\overline{Z}(\mathbf{r})$ relates the sound pressure to the sound particle velocity on the surface. This is often used to account for e.g. boundary layers of insulation materials. For exterior radiation problems and considering wave propagation in free space a further boundary condition, the so-called Sommerfeld boundary condition

$$\lim_{|\mathbf{r}|\to\infty} |\mathbf{r}| \left(\frac{\partial p(\mathbf{r})}{\partial \mathbf{r}} + jkp(\mathbf{r})\right) = 0 \tag{2.59}$$

has to be satisfied at $\Gamma_\infty$. This means that no reflection of the waves occurs at infinity. Applying these boundary conditions, a solution of (2.54) can be determined either analytically by separation of variables or numerically by using FEM or BEM, see section 4.5.

# 3 ANALYTICAL COMPUTATION APPROACH

In the following, the development of a comprehensive analytical method to determine the noise behaviour of electrical machines is presented. It comprises the determination of the air gap field and its harmonics. The derived force harmonics are then used as the boundary condition for the structural model, i.e. an infinitely long cylinder. The obtained surface oscillations subsequently serve as boundary conditions for the acoustic radiation model. The derivations presented are based on [42] and [68]. A validation of this method will be shown in chapter 5.

## 3.1 Air Gap Field

The electromagnetic causes of acoustic noise in electrical machines are mainly determined by the magnetic field in the air gap and its resulting forces on the stator and rotor teeth. The determination of the field is complicated as there are several factors, e.g. the configuration of the windings, the shape of the air gap or the material properties, that influence its behaviour [53].

For analytical investigations, several assumptions are made to get comprehensive formulations for the field computation. First of all, the field is assumed to be homogeneous. Furthermore, the magnetic field problem is reduced to a planar problem assuming an infinitely long machine. The magneto-motive forces in iron are neglected as its permeability $\mu_{Fe}$ is much larger than in air and therefore $\mu_{Fe} = \infty$ is assumed. The integral form of (2.10) then yields:

$$V_\delta(\varphi,t) = H_r(\varphi,t)\delta(\varphi,t) = \frac{1}{\mu_0} B_r(\varphi,t)\delta(\varphi,t) \tag{3.1}$$

where $V_\delta$ is the magneto-motive force in the air gap, $H_r$ is the radial component of the magnetic field intensity, $B_r$ the radial component of the magnetic flux density, $\delta$ the radial extent of the air gap, $\mu_0$ the permeability of air and $\varphi$ denotes the azimuthal coordinate in the air gap.

Introducing an azimuthally distributed, axially directed surface current density $\boldsymbol{\alpha} = \alpha \mathbf{e}_z$, the following relation for the magneto-motive force can be obtained:

$$V_\delta = R \int_\varphi \alpha(\varphi,t)\mathrm{d}\varphi + c(t). \tag{3.2}$$

where $R$ is the radius of the air gap. The constant $c(t)$ has been discussed in [68] as the contribution of the homopolar fluxes. However, these unipolar fluxes typically are

negligibly small and therefore are omitted for the further investigations which yields:

$$V_\delta(\varphi,t) = R\int_\varphi \alpha(\varphi,t)\mathrm{d}\varphi \tag{3.3}$$

Inserting this relation in (3.1), the magnetic flux density $B$ in the air gap can then be determined as follows:

$$B_r(\varphi,t) = \Lambda(\varphi,t)V_\delta(\varphi,t) \tag{3.4}$$

where $\Lambda$ is the permeance function. This approach assumes infinitely small slot openings. The slotting effects are considered by a modified air gap function $\delta''$. Both the magnetomotive force $V_\delta$ and the permeance $\Lambda$ vary with the azimuthal coordinate $\varphi$ according to the winding configuration and the slot configuration, respectively. The idea of analytical approaches [42], [68] is to represent the variation as a superposition of single wave components determined by a two dimensional Fourier decomposition.

### 3.1.1 Permeance harmonics

The variation of the permeance can be determined by a constant term $\Lambda_0$ and a periodic term $\Lambda_\lambda$:

$$\Lambda(\varphi,t) = \frac{\mu_0}{\delta(\varphi,t)} = \Lambda_0 + \Lambda_\lambda(\varphi,t). \tag{3.5}$$

The periodic term $\Lambda_\lambda(\varphi,t)$ shall now be determined as a superposition of wave components with an amplitude $\hat{\Lambda}_\lambda$, a spatial ordinal number $\lambda$, a rotational speed $\omega_\lambda$ and a phase angle $\psi_\lambda$. Furthermore the variations can be attributed to several phenomena: the variation of stator and rotor slotting (subscript SL), the permeance variation due to saturation (subscript Sa) and the variation due to eccentricities (subscript E):

$$\Lambda(\varphi,t) = \Lambda_{\lambda_\mathrm{SL}} + \Lambda_{\lambda_\mathrm{Sa}} + \Lambda_{\lambda_\mathrm{E}} = \Lambda_0 + \sum_\lambda \hat{\Lambda}_\lambda \cos(\lambda\varphi - 2\pi f_\lambda t + \psi_\lambda). \tag{3.6}$$

The variation of the permeance due to the stator and rotor slotting results in a superposition of permeance wave components $\Lambda_{\lambda\mathrm{SL}}$

$$\Lambda_{\lambda_\mathrm{SL}} = \sum_{\lambda_\mathrm{SL}} \hat{\Lambda}_{\lambda_\mathrm{SL}} \cos(\lambda_\mathrm{SL}\varphi - 2\pi f_{\lambda_\mathrm{SL}} t + \psi_{\lambda_\mathrm{SL}}), \quad \lambda_\mathrm{SL} = g_1 N_\mathrm{S} \pm g_2 N_\mathrm{R}, \qquad f_{\lambda_\mathrm{SL}} = f(1-s)\frac{g_2 N_\mathrm{R}}{p}, \tag{3.7}$$

$$g_1 = 0, \pm1, \pm2, \pm3, \ldots \qquad\qquad g_2 = 0, \pm1, \pm2, \pm3, \ldots$$

with a spatial ordinal number $\lambda_\mathrm{SL}$, which is a linear combination of the number of stator slots $N_\mathrm{S}$ and rotor slots $N_\mathrm{R}$. In the following the subscripts $S$ and $R$ denote stator and

rotor components, respectively. The coefficients are given with the counters $g_1$ and $g_2$. For $g_2 = 0$ only the stator slotting determines the permeance variations and the rotor is considered as smooth. The opposite is the case for $g_1 = 0$. Additionally, for the permeance variations of the rotor slots the rotor rotation has to be considered by the angular frequency $f_{\lambda_{\mathrm{SL}}}$. The frequency is determined by the current feeding frequency $f$, the pole pair number $p$ of the electrical machine, the slip $s$ and the spatial ordinal number due to the rotor slotting determined with $g_2 N_{\mathrm{R}}$. For the determination of the amplitudes, the permeance wave components $\Lambda_{\lambda\mathrm{SR}}$ are typically decomposed into components evoked by the stator $\Lambda_{\lambda\mathrm{S}}$ and rotor slotting $\Lambda_{\lambda\mathrm{R}}$ as well as the interacting components $\Lambda_{\lambda\mathrm{SR}}$ [68], [53].

A further influence on the permeance is given by the saturation of the teeth. The largest saturation occurs at positions where the fundamental magnetic field with a spatial ordinal number $p$ has a positive or negative maximum. The permeance wave $\Lambda_{\lambda Sa}$ due to saturation is therefore given with the spatial ordinal number $\lambda_{Sa} = 2p$ and the frequency of $f_{\lambda_{Sa}} = 2f$:

$$\Lambda_{\lambda Sa}(\varphi,t) = \sum_{\lambda_S a} \hat{\Lambda}_{\lambda_{Sa}} \cos(\lambda_{Sa}\varphi - 2\pi f_{\lambda_{Sa}} t + \psi_{\lambda_{Sa}}) \qquad \lambda_{Sa} = g_3 2p \qquad f_{\lambda_{Sa}} = g_3 2f \tag{3.8}$$
$$g_3 = \pm 1, \pm 2, \pm 3, \ldots$$

Typically, the cases $g_3 > 1$ can be neglected as their influence is only relevant for highly saturated machines. An approach to determine the amplitude $\hat{\Lambda}_{\lambda_{Sa}}$ for $g_3 = 1$ is proposed in [68], [53].

The last contribution to the permeance variations arises from the eccentricity of the rotor. The dislocation of the axis of the rotor compared to the stator can have several reasons, e.g. manufacturing inaccuracies or deflection of the rotor. The dislocation leads to a decrease of the air gap at a distinct circumferential position. The permeance wave component can be derived as follows:

$$\Lambda_{\lambda E} = \Lambda_{0E} + \sum_{\lambda_E} \hat{\Lambda}_{\lambda_E} \cos(\lambda_E \varphi - 2\pi f_{\lambda_E} t + \psi_{\lambda_E}) \qquad \lambda_E = \pm 1, \pm 2, \pm 3, \ldots \tag{3.9}$$

For a static eccentricity $f_{\lambda_E} = 0$ and for the dynamic eccentricity $f_{\lambda_E} = f\frac{\lambda_E}{p}(1-s)$. The amplitudes are functions of the deflection of the rotor axis from the stator axis [68], [53].

### 3.1.2 Magneto-motive force harmonics

Performing a two dimensional Fourier analysis, the current distribution of an $m$-corded winding can be described as follows [68]:

$$\alpha(\varphi,t) = -\sum_{\nu} \xi_\nu \hat{\alpha}_\nu \sin(\nu\varphi - 2\pi f_\nu t - \psi_\nu) \qquad \nu = p(1+2mg) \tag{3.10}$$
$$g = 0, \pm 1, \pm 2, \pm 3, \pm 4, \ldots$$

where $\xi_\nu$ denotes the winding factor which accounts for the influences of the winding configuration and is determined as follows:

$$\xi_\nu = \xi_{Z_\nu} \xi_{S_\nu} \xi_{Sk_\nu} \tag{3.11}$$

where $\xi_{Z_\nu}$ denotes the factor for the winding distribution, $\xi_{S_\nu}$ the factor for the winding pitch and $\xi_{Sk_\nu}$ the factor for the skewing. The winding factor $\xi_\nu$ is a function of the spatial ordinal number $\nu$. Inserting this relationship in (3.3) results in the following harmonic superposition for the magneto motive force:

$$V_\delta(\varphi,t) = \sum_\nu R\xi_\nu \frac{\hat{\alpha}_\nu}{\nu} cos(\nu\varphi - 2\pi f_\nu t - \psi_\nu) \tag{3.12}$$

### 3.1.3 Air-gap flux density

Using a simplified but physically relevant machine model, the previously introduced representation of the magneto motive force and permeance as a superposition of wave components with distinct spatial ordinal numbers and angular frequencies now allows the derivation of the magnetic flux density as a superposition of field components with the spatial ordinal number $k$:

$$B(\varphi,t) = \sum_k \hat{B}_k cos(k\varphi - 2\pi f_k t - \psi_k). \tag{3.13}$$

To maintain the physical allocation to the origin of the field components, the decomposition is performed, on the one hand, for discrete windings assuming constant permeance $\Lambda_0$, i.e. $\lambda = 0$, resulting in winding fields $B_{\text{wind}}$:

$$B_{\text{wind}}(\varphi,t) = \Lambda_0 R \sum_\nu \xi_\nu \frac{\hat{\alpha}_\nu}{\nu} \cos(\nu\varphi - 2\pi f_\nu t - \psi_\nu) \tag{3.14}$$

and, on the other hand, for permeance waves due to slotting, eccentricities and saturation, resulting in parametric fields $B_{\text{param}}$:

$$B_{\text{param}}(\varphi,t) = R \sum_\nu \sum_\lambda \hat{\Lambda}_\lambda \xi_\nu \frac{\hat{\alpha}_\nu}{\nu} \cos(\mu\varphi - 2\pi f_\mu t - \psi_\mu), \tag{3.15}$$

with

$$\mu = \nu \pm \lambda, \tag{3.16}$$

$$f_\mu = f_\nu \pm f_\lambda, \tag{3.17}$$

$$\psi_\mu = \psi_\nu \pm \psi_\lambda. \tag{3.18}$$

as the resulting spatial ordinal numbers, angular frequencies and phase angles of the field components for the permeance harmonics. By breaking the permeance harmonics further down, an assignment to the stator, rotor and interacting slotting fields and moreover to the saturation and eccentricity fields can be attained, see [68].

As, in general, magnetic fields are induced in both the stator and the rotor, the interaction of these fields has to be taken into consideration. For fields with the same spatial ordinal number and frequency typically a damped magnetic field results. In [68] the determination of complex damping factors using an equivalent circuit for higher harmonics is presented. If the number of cords and poles of stator and rotor are different (e.g. squirrel cage induction machine), then further magnetic field components arise.

### 3.1.4 Determination of the electromagnetic stresses

To calculate the electromagnetic forces due to the magnetic field harmonics in the air gap the Maxwell stress tensor of (2.20) is represented in cylindrical coordinates for $\mu = \text{const}$ and the constitutive law $\mathbf{H} = \frac{1}{\mu}\mathbf{B}$:

$$\overline{\mathbf{T}} = \frac{1}{\mu}\begin{bmatrix} (B_r^2 - \frac{1}{2}B^2) & B_r B_\varphi & B_r B_z \\ B_\varphi B_r & (B_\varphi^2 - \frac{1}{2}B^2) & B_\varphi B_z \\ B_z B_r & B_z B_\varphi & (B_z^2 - \frac{1}{2}B^2) \end{bmatrix} \tag{3.19}$$

with $r$, $\varphi$ and $z$ denoting the radial, azimuthal and axial direction of the machine. The surface $\Gamma$ where the stress tensor is to be evaluated shall be defined as a coaxial cylindrical surface in the air gap. The stresses shall be applied to the stator core. Thus, the normal vector $\mathbf{n}$ of the defined surface in cylinder coordinates is $\mathbf{n} = [-1\ 0\ 0]$.

With (2.21), the following stress vector is obtained for $\mu = \mu_0$:

$$\boldsymbol{\sigma}_m(r,\varphi,z,t) = -\frac{1}{2\mu_0}\begin{pmatrix} B_r^2 - B_\varphi^2 - B_z^2 \\ 2B_r B_\varphi \\ 2B_\varphi B_z \end{pmatrix} \tag{3.20}$$

The radial component of the obtained stress vector is negative, i.e. it points from the stator to the air gap. As the magnetic field has been determined assuming a planar problem, no axial component of the stress occurs (since $B_z = 0$). In [68], [34] it is pointed out that the azimuthal component does not contribute to the noise behaviour of electrical machines. Furthermore, the structural response due to azimuthal forces is mainly determined by the vibration behaviour of the teeth of the machine which involves a very detailed structural model. Since the used analytical model does not reflect this behaviour the azimuthal component of the stress vector is neglected.

With $B_\varphi = \mu_0 H_\varphi \ll B_r$, the radial stress component is thus determined only by the radial magnetic flux density. Inserting (3.13) then results in:

$$\sigma_r(\varphi,t) = -\frac{B_r^2(\varphi,t)}{2\mu_0} = -\frac{\left[\sum_k \hat{B}_{r_k} cos(k\varphi - \omega_k t - \psi_k)\right]^2}{2\mu_0} \tag{3.21}$$

The subscript $r$ for the radial magnetic field components $\hat{B}_r$ shall be omitted from now on. With appropriate operations, this equation can be reformulated to determine the radial stress as a series of stress wave components. The relation for a radial stress wave component $\sigma_r(n,\varphi,t)$ in the air gap resulting from the two field components $B_i$ and $B_j$ with the field amplitudes $\hat{B}_{ki}$, $\hat{B}_{kj}$, the spatial ordinal numbers $k_i$, $k_j$ and the angular frequencies and phase angles $\omega_{ki}$, $\omega_{kj}$ and $\psi_{ki}$, $\psi_{kj}$ is obtained as:

$$\sigma_r(n,\varphi,t) = -\frac{\hat{B}_{ki}\hat{B}_{kj}}{2\mu_0}\cos(n\varphi - 2\pi f_n t - \psi_n), \tag{3.22}$$

with

$$n = k_j \pm k_i, \tag{3.23}$$

$$f_n = f_{k_j} \pm f_{k_i}, \tag{3.24}$$

$$\psi_n = \psi_{k_j} \pm \psi_{k_i} \tag{3.25}$$

where $n$, $f_n$ and $\psi_n$ are the corresponding spatial ordinal number, the frequency and the phase angle, respectively, see also [80],[49]. Two magnetic field wave components $B_i$ and $B_j$ therefore result in six stress components: two stress components composed only of $B_i$ with $n = 0$ and $n = 2k_i$ for the spatial ordinal numbers and $\omega = 0$ and $\omega = 2\omega_i$ for the frequencies. Further two stress components composed only of $B_j$ with $n = 0$ and $n = 2k_j$ for the spatial ordinal numbers and $f = 0$ and $f = 2f_j$ for the frequencies. The last two stress components are determined by $B_i$ and $B_j$ with the spatial ordinal numbers $n = k_i \pm k_j$ and the frequencies $f = f_i \pm f_j$.

As it will be shown in the next section, mainly the stress waves with spatial ordinal numbers up to 10 are relevant for the vibrations. Furthermore, the representation obtained shows that each stress wave has a distinct frequency. If this coincides with a structural resonance frequency, large vibration amplitudes will occur.

## 3.2 Structural Vibration Computation

The determined pressure waves revolving in the air gap with distinct frequencies, spatial ordinal numbers and amplitudes serve as input for the structural vibration computation.

A model to determine the deformation of the stator has been established by Jordan (see [42]). The stator has been considered as an infinitely long cylinder. To determine the radial deformation amplitude $Y_r$ resulting from a stress wave $\sigma_r(n, \varphi, t)$, the elastodynamic equations have been set up with Cauchy's law (2.31) and assuming linear material properties (2.27). To obtain a compact formulation, the influence of shear stresses on the deflection and the rotational inertia have been neglected. Furthermore, a linearization has been applied to discard terms of higher order.

The method assumes stationary behaviour, therefore the evaluation can be carried out in the frequency domain. Jordan's formula to determine the structural deformation amplitude $\hat{Y}_r(n)$ in radial direction of order $n = 0$ yields:

$$\hat{Y}_r(n=0) = -\frac{RN}{Eh}\frac{\hat{\sigma}_r(n=0)}{\gamma^2 - 1} \tag{3.26}$$

and for $n \geq 2$:

$$\hat{Y}_r(n) = -\frac{RN}{Eh}\frac{n^2 - \gamma^2}{\left(\gamma^2 - \left(\frac{f_b(n)}{f_0}\right)^2\right)\left(\gamma^2 - \left(\frac{f_l(n)}{f_0}\right)^2\right)}\hat{\sigma}_r(n). \tag{3.27}$$

This is a compact formulation depending on the characteristic excitation parameters $\hat{\sigma}_r$, the inner stator radius $R$, the radius $N$ of the elastic line, the bulk modulus $E$ of the dynamo sheets, the yoke height $h$ and the material-dependent resonance frequencies $f_l(n)$ in azimuthal direction, $f_b(n)$ in radial direction, $f_0$ for the pulsating eigenmode and $\gamma$ for the excitation frequency related to $f_0$. The determination of the resonance frequencies in azimuthal and radial direction can be derived from [42].

Therefore, for an excitation with an ordinal number $n$, two singularities (resonances) occur with the influence of $f_b(n)$ being more important since this frequency value normally lies in a more critical range for noise computations. The computed deformation amplitude in (3.27) has the same spatial ordinal number $n$ as the stress component acting on the ring and no other characteristics are excited due to the orthogonality of the excitation modes on the eigenforms of the ring. This is not the case for a 3D stator model as will be discussed in chapter 5.

To achieve better results for the resonance frequencies, a more authentic consideration of the material composition of the stator is necessary. This means that the influence of the windings, teeth and slot wedges has to be included more accurately. This can be achieved by an approach proposed by Eickhoff (see [25]) expanding Jordan's model by modified eigenfrequencies.

To consider windings, teeth and slot wedges, a mean value for the flexural stiffness $(EI)$, where $I$ is the 2nd moment of inertia, and for the extensional stiffness $(EA)$, where $A$ is the sectional surface of the stack, are introduced. In the following, the mean values are denoted with the subscript $m$. An adapted mean density $(\rho V)_m$, related to the mean radius $a_m$ corresponding to the radius of the elastic line of the ring model is determined, which is, due to the modifications, now different from Jordan's model.

With the modified material parameters, the eigenfrequencies are computed with the advanced circular ring model by Federhofer [27] for $n = 0$:

$$f_b(n=0) = 0, \qquad f_l(n=0) = \frac{1}{2\pi}\sqrt{\frac{(EA)_m}{a_m^2(\rho A)_m}}, \tag{3.28}$$

and for $n \geq 2$:

$$f_b(n) = \frac{1}{2\pi}\sqrt{\frac{\kappa(n)(EI)_m}{a_m^4(\rho A)_m}}, \qquad f_l(n) = f_{l_0}\sqrt{n^2-1}. \tag{3.29}$$

The factor $\kappa$ depends on the spatial ordinal number $n$ and can be derived from [27].

## 3.3 Acoustic Computation

The previous computations provide the deformation of the stator ring model. The linear structural computation is performed in the frequency domain. Thus the velocity $\hat{v}$, the time

derivative of the displacement with its components $\hat{v}_x$ in $x$-direction and $\hat{v}_y$ in $y$-direction, can be obtained by a multiplication by $j\omega$ in the frequency domain:

$$\hat{\mathbf{v}} = \begin{bmatrix} \hat{v}_x \\ \hat{v}_y \end{bmatrix} = j\omega \begin{bmatrix} \hat{u}_x \\ \hat{u}_y \end{bmatrix} \tag{3.30}$$

where $\omega$ is the angular frequency and $\hat{u}_x$ and $\hat{u}_y$ are the deformation amplitudes in the $x$- and $y$-directions. For acoustic computations, the normal component of the velocity to the radiating surface is needed, see section 2.5. In the present investigation, we consider the stator as the radiating surface. This seems not very practical due to the potentially large influence of the housing. But for cylindrical-like machines where the stator is encased by a cylindrical shell directly fixed to the stator and due to the fact that we are considering a plane model, this approximation seems to be acceptable. For the ring structure, the normal direction of the velocity is the radial direction. Hence follows

$$\hat{\mathbf{v}}(n,\omega)\mathbf{n} = \hat{v}_r = j\omega\hat{Y}_r(n) \tag{3.31}$$

with $\hat{Y}_r$ the deformation amplitude in the radial direction (see (3.27)), $\mathbf{n}$ as the surface normal vector and $\hat{v}_r$ the velocity normal component in the radial direction.

The sound radiating from the surface is described by the two state variables sound pressure $\hat{p}$ and the sound particle velocity $\hat{v}_r$. The general form of the acoustic wave equation has been derived in section 2.5.

For radiating cylinders, the sound pressure can be determined in cylindrical coordinates [22], [34]. The determination of the sound pressure in the frequency domain is thus given as:

$$\hat{p}(n,r,\omega) = -\frac{j\rho_0 c}{\frac{dH_n^{(2)}(k_r r_0)}{d(k_r r_0)}} H_n^{(2)}(k_r r)\hat{v}_n(n,\omega) \tag{3.32}$$

where $H_n^{(2)}$ is the $n$-th order Hankel function of the second kind, $k_r$ is the acoustic wave number in radial direction, $r_0$ is the radius of the radiating surface and $\rho_0$ and $c$ denote the density and the sonic speed in air, respectively.

The relation between sound particle velocity $\hat{v}_r$ and sound pressure $\hat{p}$ can also be expressed by a sound impedance $\hat{Z}$:

$$\hat{Z}(n,\omega) = \frac{\hat{p}(n,\omega)}{\hat{v}_r(n,\omega)} \tag{3.33}$$

i.e.

$$\hat{p}(n,\omega) = \hat{Z}(n,\omega)\hat{v}_r(n,\omega). \tag{3.34}$$

The sound intensity $\hat{I}$ and thus the sound power $\hat{S}$ are

$$\hat{I} = \hat{p}\hat{v}_r^* \qquad\qquad \hat{S} = \int_\Gamma \hat{I}\,\mathrm{d}\Gamma \tag{3.35}$$

where $\Gamma$ denotes the surface area and $*$ the complex conjugate. $\hat{S}$ is a complex value and, similarly to electrical power, it consists of an active and a reactive part. The reactive part is dominant in the near-field and is decreasing fast with the distance from the surface. The active part of the power is that emitted into the far-field and thus relevant for acoustical computations. The radiation factor

$$\sigma = \frac{\mathrm{Re}(\hat{S})}{\rho_0 c A \tilde{v}^2} \tag{3.36}$$

is a factor relating the active sound-power to the absolute value of the calculated sound-power with $\tilde{v}$ as the root mean square of $\hat{v}$.

The general radiation factor of an infinitely long cylinder can be calculated as

$$|\hat{\sigma}(n, k_r r)| = \begin{cases} 0 & \text{for } k_0 \leq k_z \\ \dfrac{2k_0^2}{\pi r k_r^3 \left| \frac{dH_n^{(2)}(k_r r)}{d(k_r r)} \right|} & \text{for } k_0 > k_z \end{cases} \tag{3.37}$$

where $k_z$ is the wavenumber in the axial direction. The acoustic wavenumber $k_0$ is derived from the two components in axial and radial direction, i.e. $k_0^2 = k_r^2 + k_z^2$. The radiation gauge $L_\sigma$ is determined by the relation

$$L_\sigma = 10 \log_{10}(\sigma). \tag{3.38}$$

The radiation factor (or gauge) is low until a characteristic frequency is reached, i.e. as long as low sound radiation occurs. For higher frequencies, the structure is generally fully radiating. The finite length of a cylinder leads to reflections on the boundaries and furthermore to a shift of the critical frequencies to higher ones of shorter cylinders can be observed [34].

# 4 NUMERICAL METHODS

This chapter presents the numerical methods for the electromagnetic, structural mechanic and acoustic simulations. First the finite element approach is briefly introduced followed by the application to the electromagnetic field and structural vibration computation. At last the boundary element method used for acoustic wave computations is presented along with the fast multipole method.

## 4.1 Finite element method - Ritz-Galerkin method with special basis functions

Electromagnetic field and structural problems which arise in engineering and physics are typically described with appropriate differential equations and boundary conditions, which lead to boundary value problems. The origin for the finite element method is not the classical formulation, i.e. the differential equations, but the variational formulation, i.e. an integral formulation, of such a problem [108].

A time independent partial differential equation $D(u) = D_1 u - f = 0$ with a differential operator $D_1$ and a function $f$ in a domain $\Omega$ with the unknown solution $u$ shall be defined. The integral or weak formulation can then be stated as

$$\int_{\Omega} v(D_1 u - f)\mathrm{d}\Omega = 0 \tag{4.1}$$

where $v$ is an arbitrary scalar or vector function (test function) which satisfies the homogeneous boundary conditions $v = 0$ on the boundary $\Gamma$ of the domain $\Omega$. This is an alternate formulation of the boundary value problem. For more complicated problems, finding an exact solution (analytically) can be difficult or even impossible. With the weak formulation it is possible to set up methods to obtain an approximate solution instead. This leads to the method of weighted residuals and, further, to Galerkin's method, which are briefly explained in the following.

To obtain an approximate solution of the weak formulation (4.1), the following ansatz for the unknown solution $u$ shall be applied:

$$u \approx u_h = u_D + \sum_{j}^{n} u_j p_j \tag{4.2}$$

where $u_h$ denotes the approximate solution, $u_D$ satisfies the inhomogeneous Dirichlet boundary conditions. $p_j$ are $n$ linearly independent functions that satisfy the homogeneous Dirichlet boundary conditions, i.e. $p_j = 0$ on $\Gamma$ and $u_j$ are the (constant) coefficients of $p_j$.

In a next step, the method of weighted residuals [108] is applied to the weak formulation. Therefore, instead of the function $v$, a finite set of weighting functions $w_i$ is introduced. The number of weighting functions is equal the number of coefficients $u_j$. With (4.2) this results in

$$\int_\Omega w_i(D_1 u_h - f)\mathrm{d}\Omega = 0 \qquad\qquad i = 1,2,\ldots n. \tag{4.3}$$

This is a set of algebraic equations from which the unknowns $u_j$ can be determined. The term $(D_1 u_h - f)$ denotes a residual and (4.3) is a weighted integral of this residual. This weighted residual is forced to zero with all weighting functions. For this method, any set of linearly independent weighting functions can be used. If $w_i = p_i$[1], i.e. the same test functions are used for the weighting as for the approximation of $u$, this leads to the Galerkin method:

$$\begin{aligned}
&\int_\Omega p_i(D_1 u_h - f)\mathrm{d}\Omega = 0, \\
&\sum_j^n u_j \int_\Omega p_i D_1 p_j d\Omega = \int_\Omega p_i f \mathrm{d}\Omega - \int_\Omega p_i D_1 u_D \mathrm{d}\Omega \qquad\qquad j = 1,2,\ldots n.
\end{aligned} \tag{4.4}$$

The obtained set of equations is the following linear equation system in matrix notation with the stiffness matrix $\mathbf{D_1}_h$, the vector $\mathbf{u}$ with the coefficients $u_i$ and the right hand side vector (load vector) $\mathbf{f}_h$:

$$\mathbf{D_1}_h\,\mathbf{u} = \mathbf{f}_h \tag{4.5}$$

For a differential equation $D(u,\dot{u},\ddot{u}) = D_1 u + D_2\dot{u} + D_3\ddot{u} - f = 0$ with the time derivatives $\dot{u} = \frac{du}{dt}$ and $\ddot{u} = \frac{d^2u}{dt^2}$, the following approximation functions

$$u_h(\mathbf{r},t) = u_d(\mathbf{r},t) + \sum_j^n u_j(t)p_j(\mathbf{r}), \tag{4.6}$$

$$\frac{du_h}{dt} = \dot{u}_D + \sum_j^n \frac{du_j}{dt}p_j, \tag{4.7}$$

$$\frac{d^2u_h}{dt^2} = \ddot{u}_D + \sum_j^n \frac{d^2u_j}{dt^2}p_j \tag{4.8}$$

where $\mathbf{r}$ denotes the space coordinates and the coefficients $u_j(t)$ are time functions, are applied to its variational formulation. The following Galerkin equations are obtained:

$$\int_\Omega p_i(D_1 u_h + D_2\dot{u}_h + D_3\ddot{u}_h - f)\mathrm{d}\Omega = 0 \qquad\qquad i = 1,2,\ldots n,$$

[1] Actually it is the derivative of the approximation function with respect to the unknowns $w_i = \frac{\partial u_h}{\partial u_i} = p_i$.

$$\sum_j^n \int_\Omega p_i D_1 u_j p_j d\Omega + \int_\Omega p_i D_2 \dot{u}_j p_j d\Omega + \int_\Omega p_i D_3 \ddot{u}_j p_j d\Omega = \int_\Omega p_i f \mathrm{d}\Omega - \int_\Omega p_i D_1 u_D \mathrm{d}\Omega - \int_\Omega p_i D_2 \dot{u}_D \mathrm{d}\Omega - \int_\Omega p_i D_3 \ddot{u}_D \mathrm{d}\Omega. \tag{4.9}$$

A system of second order ordinary differential equations is obtained of the form

$$\mathbf{D_{1}}_h \mathbf{u} + \mathbf{D_{2}}_h \dot{\mathbf{u}} + \mathbf{D_{3}}_h \ddot{\mathbf{u}} = \mathbf{f}_h \tag{4.10}$$

with the system matrices $\mathbf{D_{1}}_h$, $\mathbf{D_{2}}_h$ and $\mathbf{D_{3}}_h$ and the right hand side vector $\mathbf{f}_h$. For symmetric differential operators $D_1$, $D_2$ and $D_3$ the system matrices are symmetric as well.

## 4.2 Application of the finite element method

For the application of the finite element method, the test functions $p_i$ have to be defined in a special way. To obtain an efficient algorithm, the following aspects should be considered. The matrices $\mathbf{D_i}_h$ and the load vector $\mathbf{f}_h$ should be easily computed and an increase of the number of test functions should lead to a decrease of the discretization error $||u - u_h||$. The fundamental idea of the finite element method is to use finite functions, i.e. functions with local supports, as the test functions $p_i$.

A volume $\Omega$ is discretized with a distinct number of elements of e.g. tetrahedral or hexahedral shape. Each corner of an element is represented by a node. In special cases, nodes on the edges or in the inner domain of the element can be defined. Neighbouring elements have to have a common node, a common edge or a common facets. For each node a test function $p_i = N_i$ is defined. The nodal shape functions $N_i$ are chosen to be continuous and piecewise polynomial and non zero only in some limited domain, the support. They satisfy

$$N_i = \begin{cases} 1 & \text{at node i,} \\ 0 & \text{at all other nodes.} \end{cases} \tag{4.11}$$

When approximating vector functions, edge shape functions $\mathbf{N}_i$ satisfying

$$\int_{edge_j} \mathbf{N}_i \cdot \mathrm{d}\mathbf{r} = \begin{cases} 1 & \text{if } i = j, \\ 0 & \text{otherwise} \end{cases} \tag{4.12}$$

are used.

A common approach for the discretization is the use of isoparametric finite elements defined in a local coordinate system $({}_l\mathbf{e}_r, {}_l\mathbf{e}_s, {}_l\mathbf{e}_t)$ with the coordinates $r$, $s$, and $t$ ranging from $-1$ to 1. Furthermore, a global coordinate system $({}_g\mathbf{e}_x, {}_g\mathbf{e}_y, {}_g\mathbf{e}_z)$ is defined. The global

positions $x_i$, $y_i$ and $z_i$ for each node $n_i$ are then defined with the same shape functions as those used for the approximation of $u$:

$$x = \sum_{i=1}^{n} N_i(r,s,t)x_i \qquad y = \sum_{i=1}^{n} N_i(r,s,t)y_i \qquad z = \sum_{i=1}^{n} N_i(r,s,t)z_i \tag{4.13}$$

This way, the boundaries of the geometry are described with the same order as the shape functions. This reduces the discretization error when applying the finite element method to curvilinear boundaries.

The choice of piecewise polynomial functions leads to sparse system matrices $\mathbf{D}_{\mathbf{I}h}$. Their entries and those of the load vector $\mathbf{f}_h$ can be computed element-wise after performing a numerical integration - typically the Gauss quadrature [9] is used for this - for each element. The approximation error for $u_h$ is typically reduced by a finer discretization or the choice of higher order shape functions. However, the larger the number of elements the higher the required memory amount and thus the computational demand.

## 4.3 Finite element method for electromagnetic fields

In the following, the application of the finite element method to electromagnetic phenomena for low frequencies shall be presented [15]. Therefore, the magnetic vector potential $\mathbf{A}$ and the (modified) electric scalar potential $v$ shall be introduced, which satisfy the following relations:

$$\mathbf{B} = \boldsymbol{\nabla} \times \mathbf{A}, \qquad \mathbf{E} = -\frac{\partial \mathbf{A}}{\partial t} - \boldsymbol{\nabla}\frac{\partial v}{\partial t}. \tag{4.14}$$

Inserting these relationships into the equations (2.8) to (2.12) results in the following differential equations:

$$\boldsymbol{\nabla} \times (\frac{1}{\mu}\boldsymbol{\nabla} \times \mathbf{A}) = \mathbf{J}_0 \qquad \text{in } \Omega_n, \tag{4.15}$$

$$\boldsymbol{\nabla} \times \frac{1}{\mu}\boldsymbol{\nabla} \times \mathbf{A} + \frac{\partial}{\partial t}\sigma\,(\mathbf{A} + \boldsymbol{\nabla} v) = \mathbf{0} \qquad \text{in } \Omega_c, \tag{4.16}$$

$$-\frac{\partial}{\partial t}\boldsymbol{\nabla} \cdot \sigma\,(\mathbf{A} + \boldsymbol{\nabla} v) = 0 \qquad \text{in } \Omega_c \tag{4.17}$$

with the following Dirichlet or Neumann boundary conditions on $\Omega_n$ and $\Omega_c$:

$$\mathbf{A} \times \mathbf{n} = 0 \quad \text{or} \quad \frac{1}{\mu}\boldsymbol{\nabla} \times (\mathbf{A} \times \mathbf{n}) = \mathbf{0} \qquad \text{on } \Gamma_c \text{ and } \Gamma_n, \tag{4.18}$$

$$v = v_0 = \text{constant} \quad \text{or} \quad \mathbf{n} \cdot \left( -\frac{\partial \sigma \mathbf{A}}{\partial t} - \frac{\partial \sigma \boldsymbol{\nabla} v}{\partial t} \right) = 0 \qquad \text{on } \Gamma_c. \tag{4.19}$$

On the interface $\Gamma_{nc}$ of the conducting and non-conducting region the tangential component of **H** and the normal component of **B** are continuous and therefore follows:

$$\nabla \times \mathbf{A}_c \cdot \mathbf{n}_c + \nabla \times \mathbf{A}_n \cdot \mathbf{n}_n = 0 \qquad \text{and } \nu_c \nabla \times \mathbf{A}_c \times \mathbf{n}_c + \nu_n \nabla \times \mathbf{A}_n \times \mathbf{n}_n = 0 \tag{4.20}$$

For the definition of the quantities, refer to section 2.2. Two symmetric differential operator matrices $\mathbf{D}_1$ and $\mathbf{D}_2$ including the Neumann boundary conditions can now be set up and the boundary value problem can now be written as

$$\mathbf{D}_1 \left\{ \begin{array}{c} \mathbf{A} \\ \nu \end{array} \right\} + \mathbf{D}_2 \left\{ \begin{array}{c} \dot{\mathbf{A}} \\ \dot{\nu} \end{array} \right\} = \mathbf{b} \tag{4.21}$$

where **b** is the corresponding right hand side vector. The approximation of the vector potential **A** shall now be carried out with the linearly independent edge basis functions $\mathbf{N}_i$ and that of the scalar potential $\nu$ with the linearly independent nodal basis functions $N_i$:

$$\mathbf{A} \approx \mathbf{A}_h = \mathbf{A}_D + \sum_{i=1}^{n_e} a_k \mathbf{N}_k, \qquad \nu \approx \nu_h = \nu_D + \sum_{i=1}^{n_n} \nu_k N_k \tag{4.22}$$

which both satisfy the homogeneous Dirichlet boundary conditions. $n_e$ is the number of unknown edge shape functions $\mathbf{N}_i$ and $n_n$ the number of unknown nodal shape functions $N_i$. Setting up a variational formulation of (4.21) and inserting the approximations for **A** and $\nu$, the Galerkin equations can be obtained and a linear ordinary differential equation system can be set up as follows, cf. (4.9):

$$\mathbf{D}_{1_h} \mathbf{x} + \mathbf{D}_{2_h} \frac{d\mathbf{x}}{dt} = \mathbf{b}_h(t) \tag{4.23}$$

with the coefficient matrices $\mathbf{D}_{1_h}$ and $\mathbf{D}_{2_h}$ and the load vector $\mathbf{b}_h$. For a more detailed derivation see appendix A.3 or refer to [15]. The vector **x** shall be defined as a vector containing the coefficients $a_k$, $k = 1, \ldots, n_e$ and $\nu_k$, $k = 1, \ldots, n_n$, respectively. The coefficient matrices typically are symmetric and sparse and appropriate direct and iterative solvers exist to solve the equation system in (4.23). If the electromagnetic finite element problem is excited by an external electric circuit, as is the case e.g. for multi-slice models [24], then non-symmetric matrices arise. To account for the non-linear material behaviour, an iteration process has to be carried out at each time step. A solution of (4.23) in the time domain can be obtained for example with the backward Euler time discretization method.

The application of the finite element method to electrical machines is described in the following chapters, where the simulation models are presented, too.

## 4.4 Finite element method in structural mechanics

For the structural finite element approach it is typical to apply the principle of virtual work to Cauchy's law (2.31). The principle of virtual work demands that for any infinitesimal

variation of the displacement in harmony with the given constraints, the work of the impressed forces is zero at the state of equilibrium. Multiplying (2.31) with the weighting function $\delta\mathbf{u}$ and integrating over the domain $\Omega$ yields [108]

$$\int_{\Omega} \delta\mathbf{s} \cdot (\boldsymbol{\nabla} \cdot \overline{\boldsymbol{\sigma}} + \mathbf{f}_B - \rho\mathbf{a}) \mathrm{d}\Omega = 0. \tag{4.24}$$

Applying Green's formulae

$$\int_{\Omega} \frac{\partial u}{\partial x_i} v \mathrm{d}\Omega = -\int_{\Omega} \frac{\partial v}{\partial x_i} u \mathrm{d}\Omega + \int_{\Gamma} uv \mathrm{d}\Gamma \tag{4.25}$$

to the first integral statement, an integration by parts of the first integral term can be carried out. This results in

$$\begin{aligned} \int_{V} \delta\mathbf{s} \cdot (\boldsymbol{\nabla} \cdot \overline{\boldsymbol{\sigma}}) \mathrm{d}V = & \\ & -\int_{\Omega} \left[ \sigma_{xx} \frac{\partial}{\partial x}(\delta s_1) + \sigma_{xy}\left(\frac{\partial}{\partial y}(\delta s_2) + \frac{\partial}{\partial x}(\delta s_3)\right) + \dots \right] d\Omega \\ & + \int_{\Gamma} \left[ \delta s_1 (\sigma_{xx} n_x + \sigma_{xy} n_y + \sigma_{xz} n_z) + \delta s_2(\dots) + \delta s_3(\dots) \right] d\Gamma. \end{aligned} \tag{4.26}$$

Similarly to (2.26), a virtual strain tensor $\delta\overline{\boldsymbol{\varepsilon}}$ can now be introduced for the first term and for the second one a surface force density $\mathbf{f}_S$. For (4.24), the following equation is then obtained:

$$\underbrace{\int_{V} \delta\mathbf{s} \cdot \mathbf{f}_B \mathrm{d}V + \int_{S} \delta\mathbf{s} \cdot \mathbf{f}_S \mathrm{d}S}_{\delta W_{ext}} \underbrace{- \int_{V} \delta\overline{\boldsymbol{\varepsilon}} : \overline{\boldsymbol{\sigma}} \mathrm{d}V}_{\delta W_{int}} \underbrace{- \int_{V} \delta\mathbf{s} \cdot \rho\mathbf{a} \mathrm{d}V}_{\delta W_{inertia}} = 0 \tag{4.27}$$

where the single terms of the virtual work can be combined to the work of the external forces $\delta W_{ext}$, the inner forces $\delta W_{int}$ and the inertia forces $\delta W_{inertia}$. The tensors $\overline{\boldsymbol{\sigma}}$ and $\overline{\boldsymbol{\varepsilon}}$ shall now be arranged as column vectors $\boldsymbol{\sigma}$ and $\boldsymbol{\varepsilon}$ (Voigt notation):

$$\boldsymbol{\sigma} = \begin{pmatrix} \sigma_{xx} & \sigma_{yy} & \sigma_{zz} & \sigma_{xy} & \sigma_{yz} & \sigma_{zx} \end{pmatrix}^T \tag{4.28}$$

$$\boldsymbol{\varepsilon} = \begin{pmatrix} \varepsilon_{xx} & \varepsilon_{yy} & \varepsilon_{zz} & \varepsilon_{xy} & \varepsilon_{yz} & \varepsilon_{zx} \end{pmatrix}^T = \boldsymbol{\mathcal{D}}\mathbf{s} \tag{4.29}$$

where $\boldsymbol{\mathcal{D}}$ denotes a differential operator matrix and $\mathbf{s} = [s_1, s_2, s_3]^T$ the displacement vector defined in a Cartesian coordinate system $(\mathbf{e}_x, \mathbf{e}_y, \mathbf{e}_z)$. The tensor product $\overline{\boldsymbol{\sigma}}\,\overline{\boldsymbol{\varepsilon}}$ can now be written as the scalar product $\boldsymbol{\sigma} \cdot \boldsymbol{\varepsilon}$ which results in:

$$\int_{V} \delta\mathbf{s} \cdot \mathbf{f}_B \mathrm{d}V + \int_{S} \delta\mathbf{s} \cdot \mathbf{f}_S \mathrm{d}S - \int_{V} \delta\boldsymbol{\varepsilon} \cdot \boldsymbol{\sigma} \mathrm{d}V - \int_{V} \delta\mathbf{s} \cdot \rho\mathbf{a} \mathrm{d}V = 0. \tag{4.30}$$

This variational formulation is precisely the weak form of the equilibrium equations.

Introducing the shape functions $N_j$ for the node $j$ of a structural finite element, the displacement field can be approximated with the nodal displacements $u_{ij}$ for the $ith$ degree of freedom at node $j$, cf. (4.2):

$$s_i(x,y,z,t) \approx s_{i_h}(x,y,z,t) = s_{i_D} + \sum_{j=1}^{n} N_j(x,y,z)u_{ij}(t) \qquad i = 1,2,3. \tag{4.31}$$

For simpler notation, a matrix of shape functions can be defined as follows, for $n_m$ nodes at element $m$ with three degrees of freedom:

$$\mathbf{H}^{(m)} = \begin{bmatrix} N_1(x,y,z) & 0 & 0 & \dots & N_{n_m}(x,y,z) & 0 & 0 \\ 0 & N_1(x,y,z) & 0 & \dots & 0 & N_{n_m}(x,y,z) & 0 \\ 0 & 0 & N_1(x,y,z) & \dots & 0 & 0 & N_{n_m}(x,y,z) \end{bmatrix} \tag{4.32}$$

The displacement field $\mathbf{u}^{(m)}$ and the strains $\boldsymbol{\varepsilon}^{(m)}$ (assuming $\boldsymbol{\varepsilon}_D^{(m)} = 0$, i.e. no inhomogeneous strains) in element $m$ can then described with the matrix of the shape functions

$$\mathbf{s}_h(x,y,z)^{(m)} = \mathbf{s}(x,y,z)_D^{(m)} + \mathbf{H}(x,y,z)^{(m)}\mathbf{u}^{(m)}, \tag{4.33}$$

$$\boldsymbol{\varepsilon}_h(x,y,z)^{(m)} = \mathcal{D}\mathbf{H}(x,y,z)^{(m)}\mathbf{u}^{(m)} = \mathcal{B}(x,y,z)^{(m)}\mathbf{u}^{(m)}. \tag{4.34}$$

The stress-strain relationship according to Hook's law is obtained with the elasticity matrix $\mathbf{C}$ as follows:

$$\boldsymbol{\sigma} = \mathbf{C}\boldsymbol{\varepsilon}, \qquad \mathbf{C} = \begin{pmatrix} 1-\nu & \nu & \nu & 0 & 0 & 0 \\ \nu & 1-\nu & \nu & 0 & 0 & 0 \\ \nu & \nu & 1-\nu & 0 & 0 & 0 \\ 0 & 0 & 0 & \frac{1-2\nu}{2} & 0 & 0 \\ 0 & 0 & 0 & 0 & \frac{1-2\nu}{2} & 0 \\ 0 & 0 & 0 & 0 & 0 & \frac{1-2\nu}{2} \end{pmatrix}. \tag{4.35}$$

Inserting these relationships in the variational formulation of the elastodynamic equation (4.27) results in

$$\mathbf{M}\ddot{\mathbf{u}} + \mathbf{K}\mathbf{u} = \mathbf{F}. \tag{4.36}$$

S For a detailed derivation of the system matrices see appendix A.4. The obtained mass matrix $\mathbf{M}$ and stiffness matrix $\mathbf{K}$ are sparse and symmetric. Damping effects can be considered for example as Rayleigh damping [69], [33]. An investigation of a mechanical system of this form has been presented in section 2.4. For most structural application, as is the case in the investigation of noise behaviour of electrical machines, it is sufficient to focus on the stationary behaviour of the system, cf. (2.40). Assuming linear material behaviour and small displacements, the solution for the nodal displacement vector can then

be determined with appropriate iterative or direct solvers. With the determination of the homogeneous solution with an appropriate eigensolver, the eigenmodes and eigenfrequencies of the discretized body can be obtained. The application of the structural finite element method to electrical machines will be discussed in detail in the following chapters.

## 4.5 Boundary element method in acoustics

For problems involving unbounded domains, the boundary element method (BEM) is an alternative simulation method. The problem is solved by first determining the boundary variables on the boundary surface $\Gamma$ of the domain $\Omega$. In a next step, the field variables in the domain $\Omega\backslash\Gamma$ can be obtained by using the boundary surface results.

There exist two main types of formulations for the boundary integral equations, the direct and the indirect method. The first one can be applied either to interior or exterior problems. The domain $\Omega$ has to be a closed domain and relates the sound pressure in any field point $P \in \Omega\backslash\Gamma$ to the sound pressure and velocity on the surface $\Gamma$ of the domain. This method is applied using the collocation method and thus typically leads to fully populated and non-symmetric matrices. In contrast to this, the indirect formulation, using the Galerkin method, solves the interior and exterior problem simultaneously and does not require a closed surface. For this work, the focus lies on the use of the indirect method. For more details about the direct method refer to [21].

For the indirect method, an arbitrary surface $\Gamma$ shall be defined with the superscript $+$ defining quantities on the exterior of the surface and the superscript $-$ on the interior. Two potentials shall be introduced, the double layer potential $\mu = p^+ - p^-$, which stands for the jump of pressure $p$, and the single layer potential $\sigma = \frac{\partial p^+}{\partial n} - \frac{\partial p^-}{\partial n}$ which stands for the jump of the normal derivative of the pressure. Using the Green's function $G(\mathbf{r},\mathbf{r}')$, which satisfies the the inhomogeneous Helmholtz equation

$$\Delta G(\mathbf{r},\mathbf{r}') + k^2 G(\mathbf{r},\mathbf{r}') = \delta(|\mathbf{r}'-\mathbf{r}|), \qquad \mathbf{r},\mathbf{r}' \in \Omega. \tag{4.37}$$

where $\delta$ denotes the Dirac delta function, the sound pressure $p(\mathbf{r})$ at any point in $\Omega\backslash\Gamma$ can be defined as follows:

$$p(\mathbf{r}) = \int_\Gamma \left( \mu(\mathbf{r}') \frac{\partial G(\mathbf{r},\mathbf{r}')}{\partial n} - \sigma(\mathbf{r}') G(\mathbf{r},\mathbf{r}') \right) \mathrm{d}\Gamma \qquad \mathbf{r} \in \Omega\backslash\Gamma \tag{4.38}$$

This formulation relates the sound pressure at an observation point $\mathbf{r}$, that satisfies the homogeneous Helmholtz equation (2.54), the boundary conditions (2.56)-(2.58) and the Sommerfeld radiation condition (2.59), to the single and double layer potential at a source point $\mathbf{r}'$ in $\Gamma$.

Now for the boundary element method, an approximation of the boundary surface and the boundary variables, i.e. the single and double layer potential, with a set of nodal shape

functions $N_k$ is performed:

$$\mu \approx \mu_h = \sum_{k=1}^{n_n} \mu_k N_k, \qquad \sigma \approx \sigma_h = \sum_{k=1}^{n_n} \sigma_k N_k. \tag{4.39}$$

The set of shape functions is defined within small surfaces (elements) on the boundary. A solution for the potentials $\sigma_h$ and $\mu_h$ can be obtained by a variational formulation of (4.38) [21] and using the Galerkin method. A symmetric matrix equation can then be obtained as:

$$\begin{bmatrix} \mathbf{A} & \mathbf{C} \\ \mathbf{C}^T & \mathbf{B} \end{bmatrix} \begin{bmatrix} \boldsymbol{\sigma} \\ \boldsymbol{\mu} \end{bmatrix} = \begin{bmatrix} f_\sigma \\ f_\mu \end{bmatrix} \tag{4.40}$$

where **A**, **B** and **C** denote the submatrices, $\boldsymbol{\sigma}$ and $\boldsymbol{\mu}$ are the vectors with the nodal values $\sigma_i$ and $\mu_i$. The right hand side is represented by the vectors $\mathbf{f}_\sigma$ and $\mathbf{f}_\mu$. The boundary conditions according to (2.56)-(2.57) are expressed as follows:

$$p^+ = p^- = \overline{p} \quad \text{on } \Gamma_d \qquad \Rightarrow \mu = 0 \tag{4.41}$$

$$\frac{\partial p^+}{\partial n} = \frac{\partial p^-}{\partial n} = -j\rho_0 \omega \overline{v}_n \quad \text{on } \Gamma_n \qquad \Rightarrow \sigma = 0 \tag{4.42}$$

The double layer potential is therefore zero on the Dirichlet boundary and the single layer potential on the Neumann boundary. The imposed pressure and velocity distributions appear in the vectors $\mathbf{f}_\sigma$ and $\mathbf{f}_\mu$. The mixed boundary condition (2.58) results in a mixed form for the single and double layer potential and appears in the matrices **C** and **B**.

Summing up, the indirect boundary element method leads to fully populated, complex, frequency dependent but symmetric system matrices. For larger problems this method is therefore faster than the direct method which has unsymmetric matrices. If the excitation frequency is equal to a resonance frequency of the inner domain $\Omega^-$ then the exterior radiation problem has no unique solution. Spurious modes occur for both the direct and indirect boundary element method. Different approaches for both methods can be applied to overcome this problem [23]. With the indirect method this problem of inner resonances can be eliminated by applying an appropriate impedance boundary condition on the surface. After determining the results on the boundary, the sound pressure on the field can be determined at any point outside the surface.

As the system matrices are fully populated, the efficiency strongly decreases with the size of the model. A recently evolving method to overcome this deficiency of the boundary element method is the application of a fast multipole method (FMM), which can achieve near $O(N)$ computational complexity, where $N$ is the number of equations. For this, the obtained system matrix is decomposed into several levels of submatrices (hierarchical clustering). The created admissible blocks are then approximated with an appropriate method. One efficient method is the adaptive block approximation which constructs a degenerated approximation using nodal interpolation in points determined in an adaptive way while realizing the algorithm [62]. For a detailed description of the FMM refer to [62].

# 5 LIMITATIONS OF THE ANALYTIC COMPUTATION APPROACH

In the design process of electrical machines analytical computation methods play an important role since, once implemented, they allow fast computations with given machine parameters and, moreover, the variation of input parameters to obtain for example an optimal geometry. However, as such methods are typically based on simplified machine models, they may lack in accuracy.

The following section deals with the validation of the analytic computation results obtained with the approach presented in chapter 3. The investigated machine types are squirrel-cage and slip-ring induction machines. For each computation step, i.e. electromagnetic fields, structural vibration and noise computation, a comparison with numerical simulations and/or measurement results is carried out. The aim of this investigation is to outlay and discuss the occurring deviations and to list the limitations of the analytic approach. Moreover, some identified effects with a possible influence on the noise behaviour of electrical machines motivate the investigations carried out in the following sections.

This work has been presented at the XIX International Conference on Electrical Machines [100] and has been published in its full extent in [101].

## 5.1 Electromagnetic Field Computation

For noise computation purposes, the focus lies on the determination of the magnetic field components leading to problematic forces, i.e. those with large amplitudes as well as frequencies and spatial ordinal numbers which coincide with resonances. Note that each force component is caused by two magnetic field components, and the combination of these two may also result in problematic frequencies or spatial ordinal numbers. As proposed in [68],[29], only distinct sets of the winding and parametric fields, cf. (3.14) and (3.15), need to be computed. The sets are defined according to the origin of the harmonic components, i.e. winding, slotting, saturation and eccentricity. Furthermore, the sets are extended by an allocation to the stator and rotor components, which, as defined in section 3.1, are denoted with the subscripts $S$ and $R$. This allows the assignment of problematic noise peaks to the causing magnetic field components. Eventually, this is the key advantage of the analytic method enabling the machine design to be modified to handle the problematic harmonics.

In the following, the sets of magnetic field components computed for this investigation are presented. As the focus of this work lies on the noise behaviour of induction machines, the following computations are confined to this machine type only. In particular, two

types of induction machines have been investigated, namely squirrel cage and the slip ring induction machines. For other machine types refer to e.g [75].

**Winding fields** The winding field components are determined by the constant permeance $\Lambda_0$ and the harmonics of the current distribution $\alpha_\nu$, cf. (3.14). The assignment to the stator and rotor winding distribution results in the field components $B_{wind_S}$ and $B_{wind_R}$ with different spatial ordinal numbers and frequencies[1]:

$$\begin{aligned} B_{\mathrm{wind}_{S,R}}(\varphi,t) =& \Lambda_0 R \sum_{\nu_S} \xi_{\nu_S} \frac{\hat{\alpha}_{\nu_S}}{\nu_S} \cos(\nu_S \varphi - 2\pi f_{\nu_S} t - \psi_{\nu_S}) + \\ & \Lambda_0 R \sum_{\nu_R} \xi_{\nu_R} \frac{\hat{\alpha}_{\nu_R}}{\nu_R} \cos(\nu_R \varphi - 2\pi f_{\nu_R} t - \psi_{\nu_R}). \end{aligned} \tag{5.1}$$

- Stator winding fields:
  The amplitudes of the stator winding fields $B_{wind_S}$ are determined by the current distribution $\alpha_{\nu_S}$ on the stator. The spatial ordinal numbers $\nu_S$ for the stator winding fields depend on the number of stator cords and pole pairs and are determined according to (3.14). The frequency of the stator winding fields is the line frequency, typically $f_{\nu_S} = f_1 = 50Hz$.

- Rotor winding fields due to fundamental (stator) field:
  The field in the air-gap leads to a current distribution $\alpha_{\nu_R}$ on the rotor according to the number of rotor cords and slots. For this evaluation, only the current induced by the fundamental stator field $B_{p_S}$ is considered as the largest current arises for it. The following spatial ordinal numbers and frequencies of $B_{wind_R}$ for the squirrel cage induction machine occur:

  $$\nu_R = p + gN_R \qquad g = 0, \pm 1, \pm 2, \ldots, \tag{5.2}$$

  $$f_{\nu_R} = f_1 \left( 1 + g\frac{N_R}{p}(1-s) \right) \tag{5.3}$$

  and for the slip-ring induction machine:

  $$\nu_R = p(1+2mg) \qquad g = 0, \pm 1, \pm 2, \ldots, \tag{5.4}$$

  $$f_{\nu_R} = f_1 \left(1 + 2mg(1-s)\right). \tag{5.5}$$

  The field with $g = 0$ denotes the armature reaction on the fundamental field and has to be considered for the resulting fundamental wave $B_p$. In combination with the fundamental field, rotor fields with $g \geq 1$ result in forces with large amplitudes and problematic frequencies. For $s = 0$, i.e. the no load operating point, these field components are zero.

[1] The components with the same spatial ordinal number and frequency result in a superposition of the corresponding components to a resultant field wave (armature reaction).

**Parametric field components** The parametric field components are determined by the multiplication of the winding harmonics with the harmonics of the permeance vairations, see section 3.1.3. Permeance variations due to the slotting $\Lambda_{\lambda_{\mathrm{SL}}}$, saturation $\Lambda_{\lambda_{\mathrm{Sa}}}$ and eccentricity $\Lambda_{\lambda_{\mathrm{E}}}$, cf. (3.6), lead to magnetic field components categorized as follows:

- Slotting fields $\Lambda_{\lambda_{\mathrm{SL}}}$:
  The permeance variation due to the stator and rotor slotting is given in (3.7) and the resulting magnetic field components are determined according to (3.15) with the harmonics of the magneto-motive force waves $\alpha_{\nu_{S,R}}$, again due to stator and rotor currents. For this investigation only components with the fundamental current distribution $\alpha_p$, i.e. $\nu = p$, are considered. The magneto-motive force harmonics of higher order are neglected as either the amplitudes are too small, or the resulting field components contribute to force waves with very large frequencies only. The slotting field components are obtained by splitting the permeance variations given in (3.7) into stator, rotor and interacting components:

$$\begin{aligned} B_{SL} = R\frac{(\xi_{p_S}\hat{\alpha}_{p_S} + \xi_{p_R}\hat{\alpha}_{p_R})}{p} \Bigg( & \sum_{\mu_{SL_S}} \hat{\Lambda}_{SL_S} \cos(\mu_{SL_S}\varphi - 2\pi f_{\mu_{SL_S}} t - \psi_{SL_S}) + \\ & \sum_{\mu_{SL_R}} \hat{\Lambda}_{SL_R} \cos(\mu_{SL_R}\varphi - 2\pi f_{\mu_{SL_R}} t - \psi_{SL_R}) + \\ & \sum_{\mu_{SL_{SR}}} \hat{\Lambda}_{SL_{SR}} \cos(\mu_{SL_{SR}}\varphi - 2\pi f_{\mu_{SL_{SR}}} t - \psi_{SL_{SR}}) \Bigg). \end{aligned} \tag{5.6}$$

  The spatial ordinal number $\mu_{SL_S}$ for the stator slotting fields are therefore determined with $\mu_{SL_S} = p + g_S N_S$ for $g_S = \pm 1, \pm 2, \ldots$ and the frequency is the same as for the winding fields, i.e. $f_{\mu_{SL_S}} = f_1 = 50\mathrm{Hz}$. The amplitude of the resulting field for these spatial ordinal numbers is determined by an addition of the corresponding winding and slotting field components with the phases considered. The parametric fields due to the rotor slotting arise with the spatial ordinal numbers $\mu_{SL_R} = p + g_R N_R$ for $g_R = \pm 1, \pm 2, \ldots$ and the frequencies $f_{\mu_{SL_S}} = f_1 \left(1 + g_R \frac{N_R}{p}(1-s)\right)$ and also have to be superimposed to the corresponding winding fields $B_{wind_R}$.

  The permeance variation due to the interaction of the rotor and stator slotting in combination with the fundamental current distribution $\alpha_p$ leads to field components with the following spatial ordinal numbers $\mu_{SL_{SR}}$ and frequencies $f_{\mu_{SL_{SR}}}$:

$$\mu_{SL_{SR}} = p + g_S N_S + g_R N_R \qquad g_{S,R} = \pm 1, \pm 2, \ldots, \tag{5.7}$$

$$f_{\mu_{SL_{SR}}} = f_1 \left(1 + g_R \frac{N_R}{p}(1-s)\right). \tag{5.8}$$

- Stator saturation fields:
  Further parametric stator fields are caused by the permeance variation due to saturation, see section 3.1.1.

The permeance variation with $\lambda_{Sa}$ in combination with the higher harmonics of the current distribution, in particular the slot-harmonics with $\nu_S^* = 1 + gN_S$ for $g = \pm 1, \pm 2, \ldots$, lead to magnetic field components $B_{Sa_S}$ with spatial ordinal numbers $\mu_{Sa_S} = \nu_S^* \pm \lambda_{Sa}$ and a frequency of $f_{\mu_{Sa_S}} = (1+2g_3) f_1$:

$$B_{Sa_S}(\varphi,t) = R \sum_{\nu_S^*} \sum_{\lambda_{Sa}} \hat{\Lambda}_{\lambda_{Sa}} \xi_{\nu_S^*} \frac{\hat{\alpha}_{\nu_S^*}}{\nu_S^*} \cos(\mu_{Sa_S}\varphi - \omega_{\mu_{Sa_S}} t - \psi_{\mu_{Sa_S}}) \tag{5.9}$$

- Rotor fields due to fundamental saturation field:
  The saturation field $B_{Sa_S}$ with $\mu = 3p$ (the fundamental saturation field) gives rise to a current distribution $\alpha_{\nu_R}$ in the rotor with $\nu_R = 3p$ that, in combination with the permeance variation of the rotor slotting, causes field components $B_{Sa_R}$ with spatial ordinal numbers $\mu_{Sa_R} = 3p + gN_R$ and frequencies $f_{Sa_R} = f_1 \left(3 + g\frac{N_r}{p}(1-s)\right)$:

$$B_{Sa_R}(\varphi,t) = R \sum_{\mu_{Sa_R}} \hat{\Lambda}_{\lambda_{Sa}} \xi_{3p_R} \frac{\hat{\alpha}_{3p_R}}{3p} \cos(\mu_{Sa_R}\varphi - \omega_{\mu_{Sa_R}} t - \psi_{\mu_{Sa_R}}) \tag{5.10}$$

- Rotor fields due to eccentricities:
  The static and dynamic eccentricity of the rotor also cause a permeance variation as explained in section 3.1.1. Again, only the fundamental current distribution $\alpha_p$ in combination with the permeance variations with a spatial ordinal number $\lambda_E = \pm 1$ is considered, as those amplitudes are the largest. The arising field components $B_E$ are determined as follows

$$B_E = R \frac{(\xi_{p_S}\hat{\alpha}_{p_S} + \xi_{p_R}\hat{\alpha}_{p_R})}{p} \sum_{\mu_E} \hat{\Lambda}_{\lambda_E} \cos(\mu_E\varphi - \omega_{\mu_E} t - \psi_{\mu_E}) \tag{5.11}$$

  with the resulting spatial ordinal numbers $\mu_E$ and frequencies $f_{\mu_E}$:

$$\mu_E = p \pm 1 + gN_R, \tag{5.12}$$

$$f_{\mu_E} = 0 \qquad \text{for static eccentricity,} \tag{5.13}$$

$$f_{\mu_E} = f_1 \left(1 + g\frac{N_R}{p}(1-s)\right) \qquad \text{for dynamic eccentricity.} \tag{5.14}$$

The computation of the appropriate winding factors $\xi_\nu$ and amplitudes for the current distribution $\hat{\alpha}_\nu$ and permeance waves $\hat{\Lambda}_\lambda$ is taken from [68], [54]. For skewed induction machines a skewing factor has to be applied to account for the reduction of the induced voltage in the rotor [68].

### 5.1.1 Validation of the magnetic field results and the computed stress wave components

The validation of the computed magnetic field components is carried out for a squirrel cage induction machine with its rotor skewed one stator slot pitch. The machine parameters are listed in Table A.1 in the appendix. In order to validate the analytical results for the magnetic field components, a comparison with numerical simulation results is carried out. An electromagnetic finite element simulation has been performed for a 2D multi-slice model [24]-[74]. A nonlinear, transient simulation has been carried out for the nominal operating point with a stator current of 150 A and a rotational speed of 2991 rpm for the rotor. A detailed description of the finite element modelling and the evaluation of its results in the air gap is presented in chapter 6. There, the variation of the flux in axial direction due to the skewing is investigated. To be able to compare the numerical results with the analytical ones, the magnetic field along the air gap on the stator side is taken and its harmonics are computed with a two-dimensional Fourier transformation [58].

In Fig. 5.1, the amplitudes of the magnetic field components for 50Hz are depicted for each spatial ordinal number for the numerical and the analytical computations. Especially the fundamental field component $B_p$ and the stator slot harmonics with the spatial ordinal numbers of $\nu_S^* = p + g_S^* N_S$ are sticking out. In Fig. 5.2, the harmonics due to the rotor

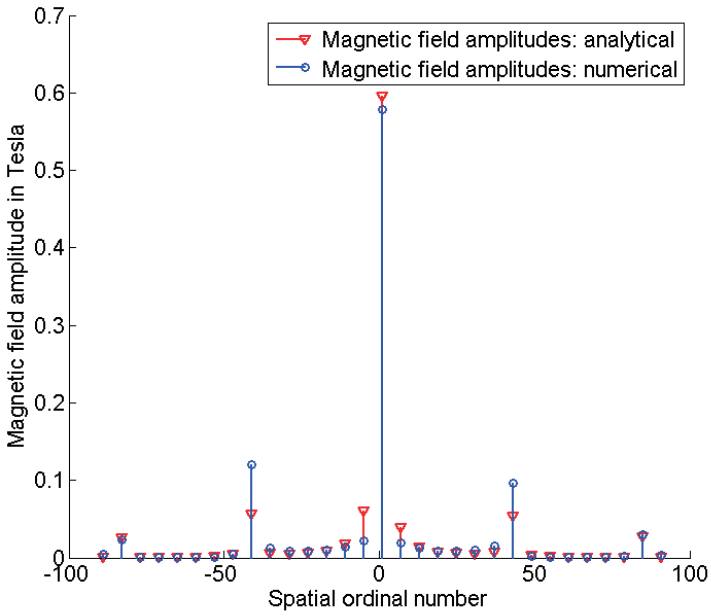


Figure 5.1: Comparison of the numerical and analytical results for the magnetic field amplitudes for $f = 50$ Hz

slotting, with the spatial ordinal numbers $\mu_{SL_R} = p(1 + gN_R)$ and frequencies $f_{\mu_{SL_R}}$, are depicted.

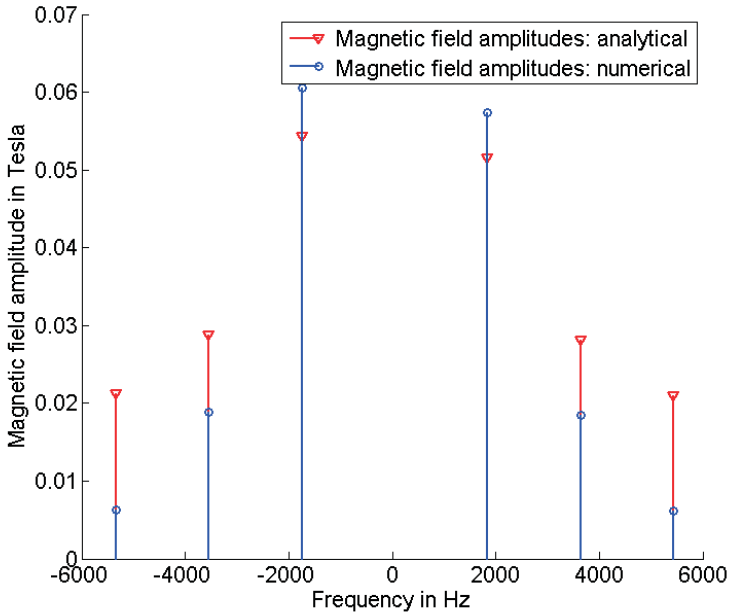


Figure 5.2: Comparison of the numerical and analytical results for the magnetic field amplitudes due to rotor slotting

The comparison of the frequencies and spatial ordinal numbers of the magnetic field components of the numerical and the analytical solutions shows a very good agreement especially for those due to the rotor slotting and the saturation. This is a very important result, since the prediction of the excitation frequencies of the forces is of great interest in order to determine an adequate offset to structural resonance frequencies.

The comparison of the magnetic field components shows discrepancies of the amplitudes and phases. The numerical solution for the first slot harmonics of the stator and the rotor fields yields larger amplitudes than the analytical solution. For the stator field the deviations are about 50%. However, the second slot harmonics for the stator fields match quite well, although their contribution to large force amplitudes is low. For the rotor slotting fields, the deviations increase with the spatial ordinal number and the frequency respectively. The main cause for these differences is the more detailed model of the finite element simulation where nonlinear and leakage effects are considered in a more accurate way. The multiplication of the field components, necessary for the determination of the stress wave components, therefore leads to even larger discrepancies which can also be seen in Figs. 5.3 and 5.4.

The stress waves acting on the stator teeth in the air gap are computed according to (3.22) with the previously obtained magnetic field components. In Figs. 5.3 and 5.4, the stress amplitudes at a frequency of 1794.7 Hz and 1894.7 Hz resulting from the rotor slot field harmonics are depicted with the corresponding mode numbers and are compared to

the numerical solution. Obviously the most striking component is the stress wave resulting

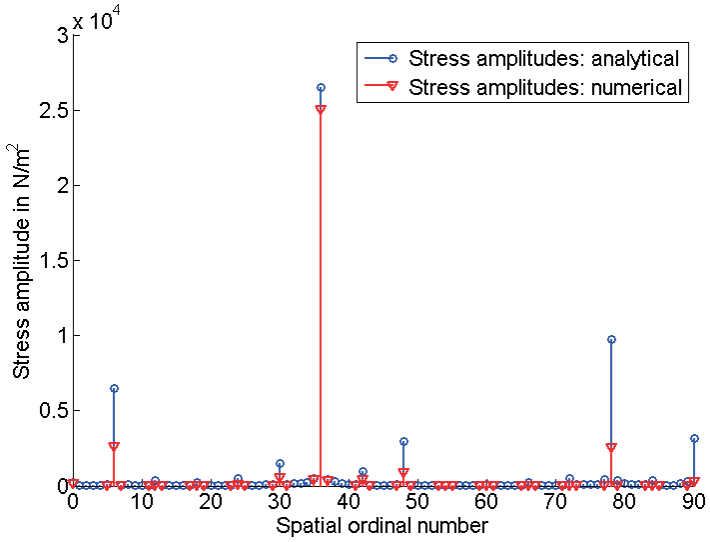


Figure 5.3: Comparison of the numerical and analytical results for the stress amplitudes for $f = 1794.7$ Hz

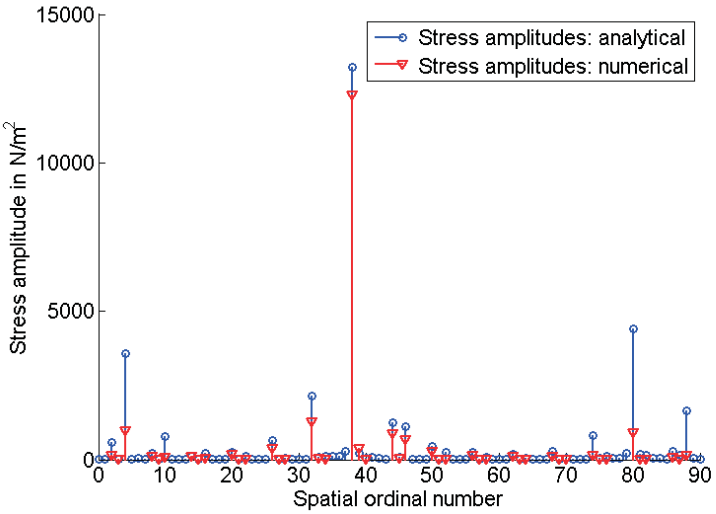


Figure 5.4: Comparison of the numerical and analytical results for the stress amplitudes for $f = 1894.7$ Hz

from the fundamental field $B_p$ and the rotor slot harmonics $B_{\nu_R^*}$. However, the corresponding spatial ordinal number is very large and, as mentioned in chapter 3, only forces with low spatial ordinal numbers are of interest, because those result in large bending deformations and thus problematic structural vibrations. The largest components with low spatial

ordinal numbers arise from the combination of the stator slot harmonics and the rotor slot harmonics. The comparison of the analytical with the numerical results shows large discrepancies for these components. The large deviations can be lead traced to the deviations of the field components which of course affect the amplitudes of the stress components as mentioned before.

In summary, the comparison shows a very good agreement for the frequencies and spatial ordinal numbers. The amplitudes of the field components yields adequate results, in particular for the stator and rotor slotting fields. The discrepancies of the forces are the largest for the lower spatial ordinal numbers. However, those are said to be the ones which lead to the largest structural vibrations and thus contribute most to the noise behaviour [16]. An investigation regarding the components with higher spatial ordinal numbers, which can have very large amplitudes, is presented in chapter 7. Another point shortly mentioned previously is the obvious change of the flux in axial direction due to the skewing. This also leads to forces with an axial variation. An approach to determine this variation is presented in chapter 6. An investigation of the influence of axially varying force distribution is shown in chapter 7.

## 5.2 Structural Vibration Computation

This section deals with the investigation of the analytically computed structural vibration results. Therefore, in a first step, a comparison with vibration amplitudes obtained with a three-dimensional finite element model of a cylinder is carried out. Following that, the influence of the modified eigenfrequencies on the structural response is analysed and discussed. After that, a comparison with measurement results is carried out and the eigenfrequencies and the computed structural responses are validated.

### 5.2.1 Comparison of the computation results

The computation of the structural response due to the electromagnetic force wave with an amplitude $\sigma_r(n)$, a frequency $f(n)$ and a spatial ordinal number $n$ is performed with the computation model presented in 3.2. In a first step, the influence of the teeth and windings is not considered. Therefore, the frequency dependent deformation amplitude of the ring is analysed with the eigenfrequencies $f_b(n)$ and $f_l(n)$ determined according to Jordan [42].

To validate the analytical solution, a comparison with a numerical structural simulation of a corresponding three dimensional cylinder model has been performed. The homogeneous cylinder is discretized with second order hexahedral elements and the mass matrix $\mathbf{M}$ and the stiffness matrix $\mathbf{K}$ are computed. A surface force distribution $\mathbf{f}_S = \hat{\sigma}_r e^{j(n\varphi-\omega t)}$ with $\hat{\sigma}_r = 1\,\mathrm{N/m^2}$ and $n = 4$ is applied to the structural finite element model, resulting in a nodal force vector $\mathbf{F}$. The mechanical stress is impressed on the inner side of the ring only and is uniformly distributed in axial direction. The solution for the nodal displacements $\mathbf{u}$ can then be obtained from (4.36) for the undamped mechanical system. As only

the stationary solution is of interest, a harmonic analysis, cf. (2.39), is performed for each angular frequency $\omega = 2\pi f$ for $f = 0$ to $3000Hz$:

$$(-\omega^2\mathbf{M}+\mathbf{K})\hat{\mathbf{u}} = \hat{\mathbf{F}}, \tag{5.15}$$

and the nodal displacements $\hat{\mathbf{u}}$ are obtained for the applied nodal force vector $\hat{\mathbf{F}}$ in the frequency domain. The normal (i.e. radial) component $\hat{v}_r$ of the surface velocity $\hat{\mathbf{v}}$ is then obtained for the numerical result as follows:

$$\hat{v}_r = \hat{\mathbf{v}} \cdot \mathbf{n} = j\omega\hat{\mathbf{u}} \cdot \mathbf{n}. \tag{5.16}$$

The result for the absolute value of the velocity amplitude on the surface of the cylinder is depicted in Fig. 5.5 along with the computation results from Jordan's model. It can be seen that the curve is nearly the same up to the first occurring resonance. The corresponding mode excited at this frequency has a spatial ordinal number of four in azimuthal direction. For higher excitation frequencies it can be seen from the results of the three dimensional model that further resonances occur. As presented in section 3.2, the radial deformation

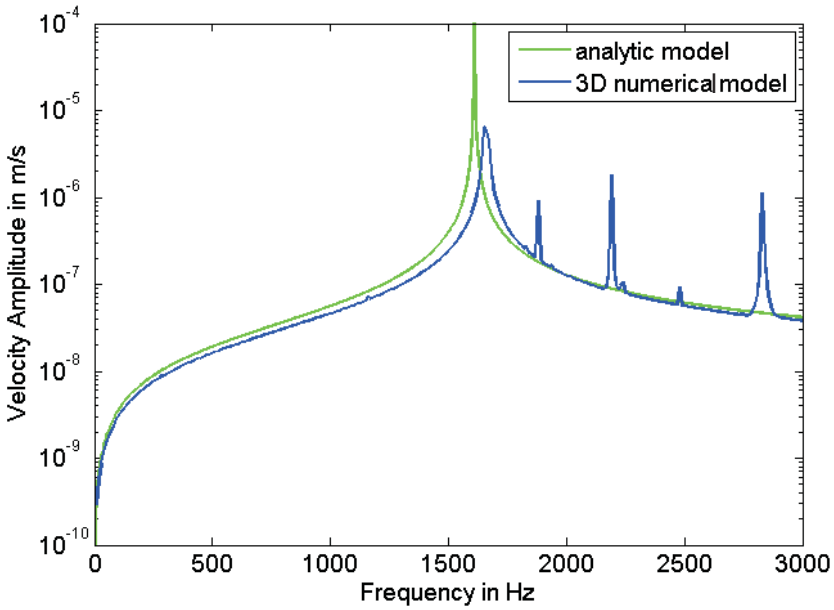


Figure 5.5: Analytical and 3D numerical solution of the velocity amplitude against excitation frequency

computed with the analytical model for the infinitely long cylinder also depends on the azimuthal material properties. Actually, the radial force component gives rise to a resonance at $f_l(n)$, which corresponds to an azimuthal mode shape. This fact is often neglected as the eigenfrequency $f_l(n)$ is much larger than $f_b(n)$ and mostly out of the considered frequency range. For the three-dimensional simulation model, the material properties are

coupled in the radial, azimuthal and axial directions. This leads to mode shapes with axial deformation characteristics with eigenfrequencies in the frequency range of interest for noise computations. This behaviour has also been confirmed by measurements, see section 5.2.2.

The deviation of the primal resonance is due to the simplifications conducted in the derivation of the analytic formulation for the deformation amplitude. The larger the spatial ordinal number, the larger are the discrepancies compared to a numerical simulation result. Generally, the analytic model results in higher eigenfrequencies for eigenmodes of higher order. For spatial ordinal numbers $n = 6$, the deviations are around $30Hz$.

In a further investigation step, the influence of the modified eigenfrequencies in (3.28) and (3.29) on the vibrational behaviour is analysed. This is done by comparing the frequency dependent deformation characteristics due to force waves with different spatial ordinal numbers. The modified computation of the structural deformation is performed with the modified resonance frequencies (see (3.28) and (3.29) in section 3.2). The comparison of the results is shown in Fig. 5.6. It can be seen that there is a good agreement for the

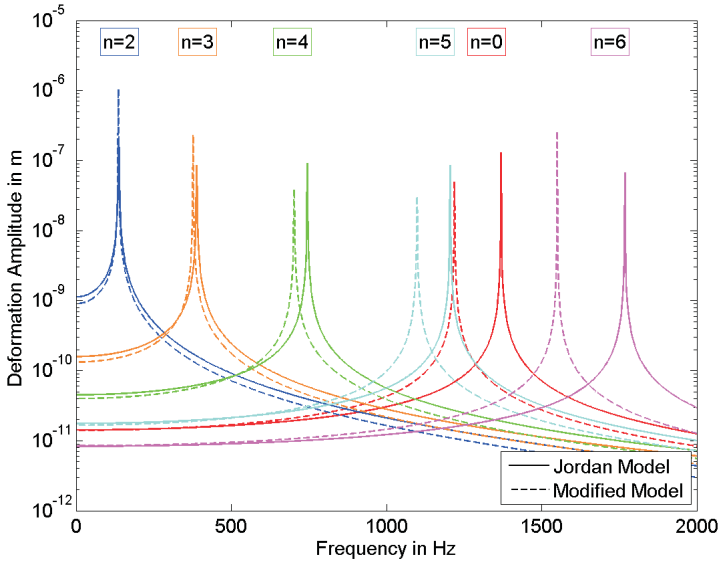


Figure 5.6: Comparison of the Jordan results and the adapted model for the harmonic responses of the structural deformation

excitations with the spatial ordinal numbers two and three. The higher the resonance frequencies of the excitation with distinct spatial ordinal number, the higher is the deviation of the deformation amplitude. The resonance frequencies are shifted to lower frequencies which is due, on the one hand, to the influence of the added masses, and, on the other hand, to the different method of computing the eigenfrequencies (3.28) and (3.29).

### 5.2.2 Comparison with measurements

A validation of the modified resonances (3.28) and (3.29) is carried out by a comparison with measurements on a laminated stator core stack. The eigenfrequencies for spatial ordinal numbers up to 5 have been determined by measuring the frequency response on the surface of the stator core when exciting the structure punctually with an electromagnetic shaker. Stacks with and without windings, slot wedges and impregnation have been investigated.

In Table 5.1 the measurement results for the eigenfrequencies of an impregnated stack without winding (model 1, outer diameter $DA = 0.4m$) and for an impregnated stator core with winding (model 2, outer diameter $DA = 1m$) are listed with the corresponding spatial ordinal numbers and the computed results. For some spatial ordinal numbers several measurements have been conducted and therefore the highest and the lowest frequency values are depicted only.

Table 5.1: Measured and computed eigenfrequencies of a laminated core

| | Model 1 (DA=0.4m) | | Model 2 (DA=1m) | |
|---|---|---|---|---|
| $n$ | $f_{meas}$ in Hz | $f_{comp}$ in Hz | $f_{meas}$ in Hz | $f_{comp}$ in Hz |
| 2 | 661.3 | 663.2 | 142.2/143.7 | 138.7 |
| 3 | 1767.4 | 1791.0 | 382.3/386.0 | 386 |
| 4 | 3107.5 | 3237.8 | 699.5 | 725 |
| 5 | - | 4897.2 | 1038/1052.4 | 1138 |

As model 1 has no windings, the computation of the eigenfrequencies according to (3.28) and (3.29) has been performed by adapting the mean density $(\rho V)_m$ to take into account the additional teeth mass. For model 2, the additional mass of the winding has also been included in $(\rho V)_m$. Furthermore the flexural stiffness $(EI)_m$ has been adapted to consider the influence of the slot wedges and the winding. The results for the resonance frequencies are given in Table 5.1 and show a good agreement with the measurements of these two different models.

The results above are related to spatial ordinal numbers for the azimuthal direction and a uniform characteristic in axial direction. However, for the three-dimensional model further resonances occur, as the previously presented simulation results have also shown. To analyse the vibration behaviour along the axial direction further measurements have been conducted on model 2. In Fig. 5.7, the frequency response function of the measurement results is depicted. This result has been obtained by measuring the accelerations at 60 points (12 azimuthal angles and 5 axial positions) on the surface of the laminated core. It can be seen in Fig. 5.7 that there are more resonances occurring besides the purely azimuthal modes. The corresponding eigenforms are characterized by additional axial characteristics (besides azimuthal). This three-dimensional behaviour cannot be estimated with the pre-

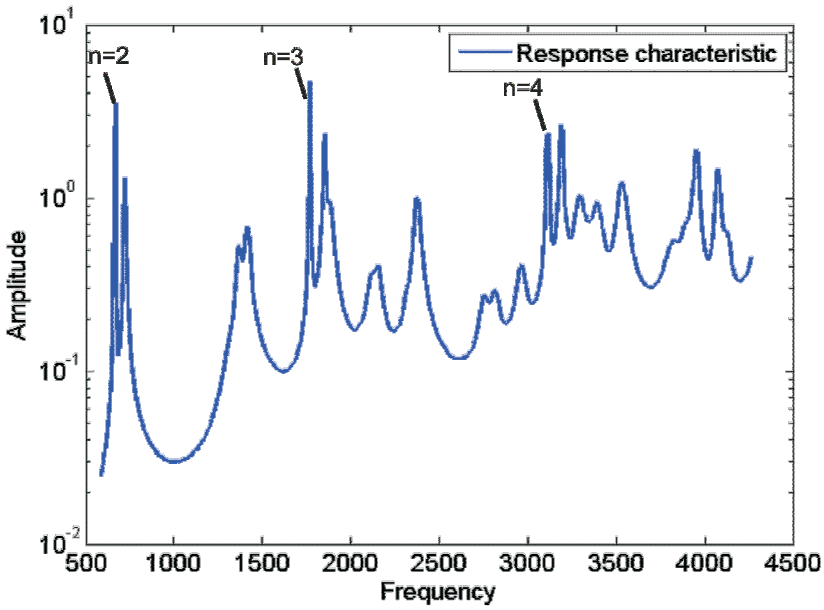


Figure 5.7: Measured frequency response on the surface of a stator core stack

sented computational method and the influences are therefore not considered in the whole noise computation approach. Additionally the mounting of the stator in the housing and the housing itself have an impact on the structural behaviour [72], and, depending on the construction design and complexity, their influences cannot be neglected.

As a further step in the validation of the analytical approach, a comparison of Jordan's amplitude function (3.27) with the eigenfrequencies according to (3.29) and measurements of the deformation of a stator core stack is presented. These measurements have been carried out on a machine where problems have arisen with the structural mode $n = 5$. This mode is dominantly excited at approximately 640 Hz for a stator frequency of 50 Hz. The investigated machine is a squirrel cage induction machine with a nominal power of 0.9 MW, a stator frequency of 50 Hz, 72 stator teeth, 89 rotor teeth and a pole pair number of 6. To get the characteristic behaviour of the excited mode, a variation of the stator frequency from 30 Hz to 55 Hz has been performed. The acceleration sensors are placed on the surface of the stator core stack as depicted in Fig. 5.8. First, steady-state measurements have been carried out followed by a transient measurement. The result for the velocity amplitude against the frequency is shown in Fig. 5.9 and compared with the simulation result of the modified analytical model for the velocity amplitude of the relevant mode. It can be seen that the measurement results yield very good agreement with the simulation result. Due to machine load limitations, the frequency sweep could not be continued, therefore the rise in the deformation amplitude could not be verified.

To sum up, the measurements have shown that the influence of the impregnated windings and the wedges leading to an increase in the stiffness of the laminated core, and of the

Figure 5.8: Measurement assembly - placement of the acceleration sensors on the surface of the investigated stator core stack

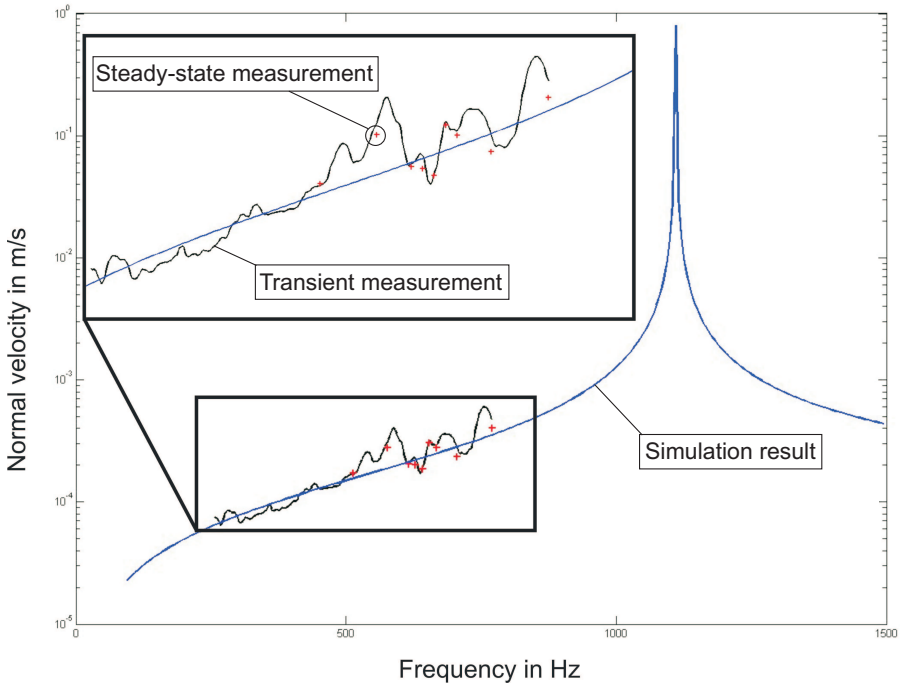


Figure 5.9: Comparison of the measured and analytically computed velocity amplitude

mass of the windings resulting in a decrease of the eigenfrequencies cannot be neglected, a fact also discussed in [83], [25]. Generally, the presented approach for the resonance frequencies works very well. However, it should be noted that problems may occur for stator sheets with a large tooth height compared to the yoke height. In this case the resonances of the teeth may occur near eigenfrequencies of the ring and thus result in larger errors for the computational results. Furthermore, the three-dimensional nature of the system leads to further resonances which cannot be determined with the two-dimensional model. This results in further uncertanties in the design of a low-noise induction machine. In addition, the coupling of the stator core stack to the housing and the housing itself may influence the structural vibration behaviour. An investigation regarding this topic is presented in chapter 8.

## 5.3 Acoustic Computation

The analytical approach takes an infinitely long cylinder to determine the radiation gauge, cf. section 3.3. With the determined velocity on the surface of the structure, the sound pressure can be computed according to (3.32). In a first step, the influence of the modified eigenfrequencies shall be investigated again, now for the emitted sound pressure. Therefore, the sound pressure for the results in Fig. 5.6 is computed according to (3.32). The resulting sound pressure level is depicted in Fig. 5.10. The results for the deviations are quite analogous to the results shown in Fig. 5.6. For lower excitation modes the variance is not larger than 4 dB. For excitations with higher mode numbers the deviation becomes quite large - up to 10 dB - due to the shift of the eigenfrequencies. This shows that a wrong determination of the eigenfrequencies can lead to large deviations regarding the computed sound pressure.

### 5.3.1 Comparison with measurements

In this section a comparison of the analytically determined sound pressure resulting from the magnetic field harmonics in the air gap with measurements is carried out. The analytical computation first yields the magnetic field component and, from these, the resulting stresses on the stator core stack are determined for each excitation frequency $f_i$. For all $k$ stresses with different spatial ordinal numbers $n$ at this excitation frequency $f_i$ the sound pressure components $\hat{p}_k(n, r, \omega_i)$ have to be computed. Finally, the resulting sound pressure at $f_i$ can be determined by summing up all sound pressure components. Hence, a noise spectrum is gained, which can be compared with measurements. These are taken at a distance of one meter from the investigated machine according to [1] and [2] respectively, see Fig. 5.11, and deliver the frequency spectrum of the A-weighted (see appendix A.2 or [34]) sound pressure levels. However, for comparing the measurement results with the computed ones, the A-weighting of the measurements has to be compensated. The measurement data of about thirty different induction machines have been investigated and

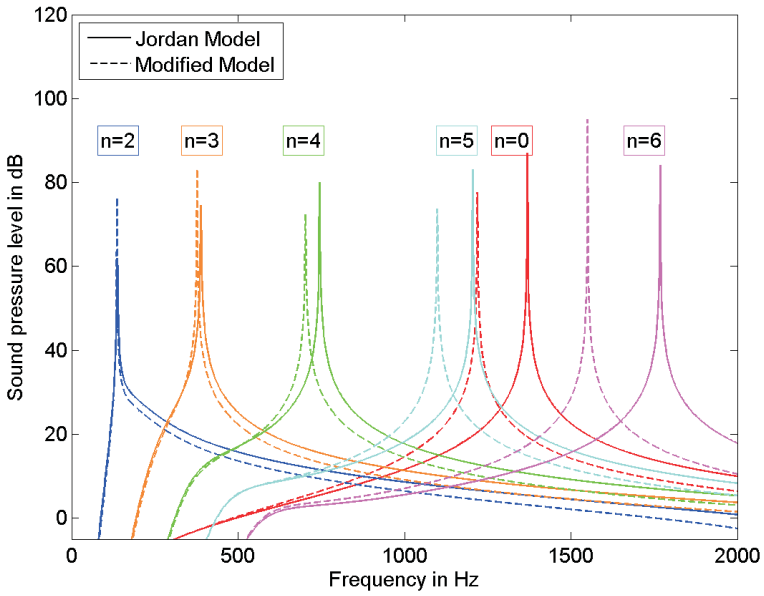


Figure 5.10: Comparison of the Jordan results and the adapted model for the sound pressure level

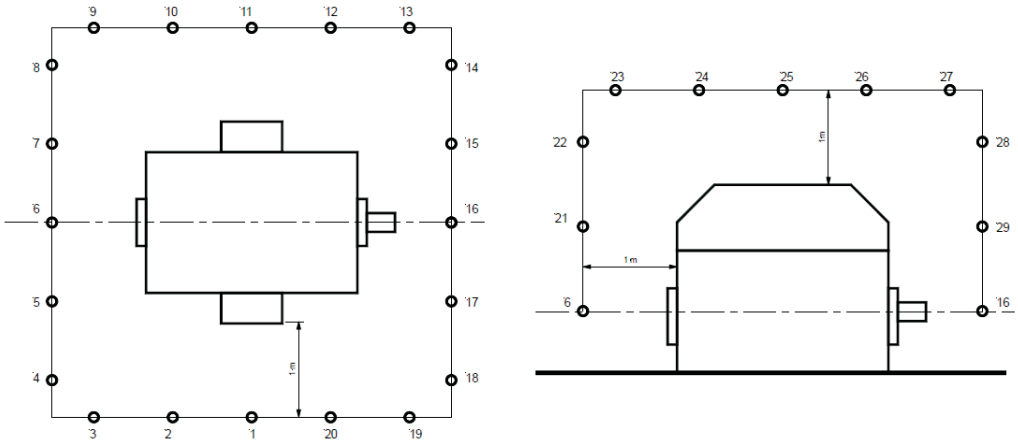

Figure 5.11: Acoustic measurement assembly

compared to the analytical results. To show all comparisons would be beyond the scope of this work, thus the results of two different induction machine types, presented in Fig. 5.12 and Fig. 5.13 and representing the major effects and problems that occur, shall be discussed in more detail.

In Fig. 5.12, the measurement results for the induction machine with squirrel cage rotor, see appendix A.5, and the results of the analytical computation for the nominal operating

point are shown. In Fig. 5.13, the comparison results of a double fed induction machine are shown for the cascade operating-point. The parameters for this machine are given in Table A.3. One striking difference between these machine types is the number of excitation frequencies of the rotating force waves. The rotor field harmonics of the squirrel cage rotor depend on the number of rotor slots whereas, for the double fed induction machine with the slip ring rotor, the rotor field harmonics depend on the number of windings in the rotor. Thus many more excitation frequencies exist for the latter machine type. This makes it very difficult to set up a proper design because, with the enormous amount of excitation frequencies, the probability to catch a structural resonance is very high.

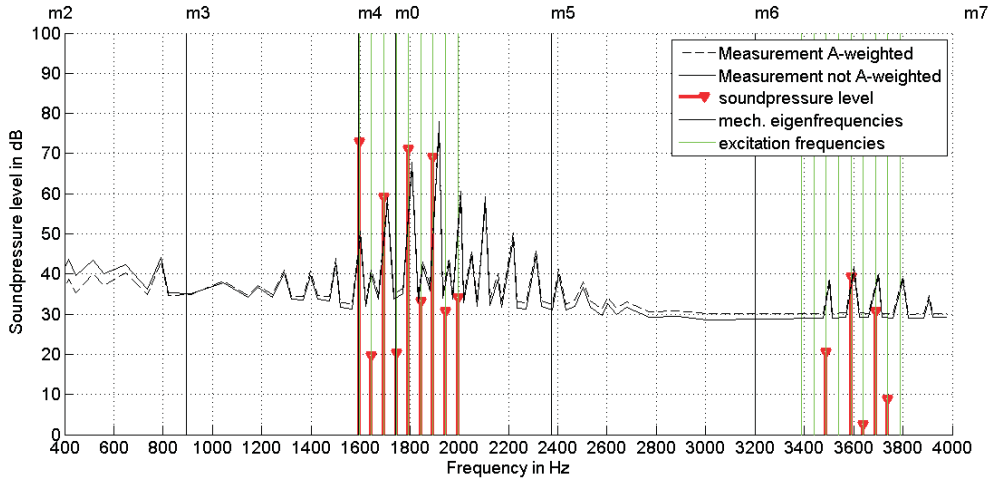


Figure 5.12: Comparison of the measurement results with the computation results of a squirrel cage induction machine

The measured sound pressure levels comprise the typical noise characteristics of electric machines. There exist striking peaks in the sound pressure levels. These can be clearly attributed to the exciting forces resulting from the electromagnetic fields. The comparison with the analytical results shows a good agreement of the computed excitation frequencies and the frequencies of the measured noise peaks. The sound pressure level amplitudes however do not agree at every peak, which is even more striking for the double fed induction machine.

The deviations can be explained by the differences of the magnetic field results as explained in section 5.1.1 leading to a different excitation of the structure. Furthermore, the two-dimensional structural model fails to mimic the complex machine behaviour since it lacks bearings, cooling devices etc. Especially the structural influence of the housing can be grave. The plates encasing the electrical machines have a dense distribution of the structural eigenfrequencies in the frequency range interesting for noise investigations [99], due to the flexural behaviour of the plates. If one of those structural eigenforms is excited, large deformation amplitudes due to the plate bending may occur and this will result in a high sound radiation.

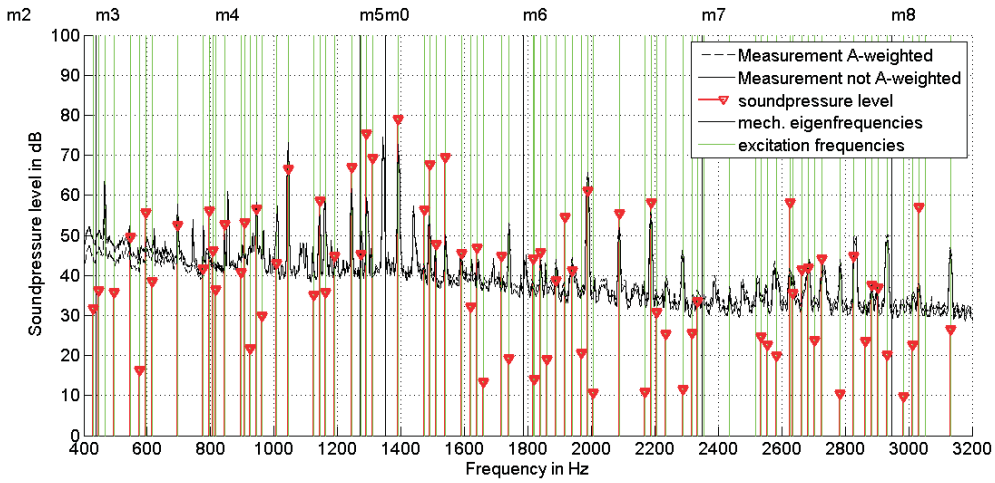


Figure 5.13: Comparison of the measurement results with the computation results of a double fed induction machine

Especially in Fig. 5.12, measured noise peaks can be seen that are not predicted by the presented analytical approach. The finite element simulation of this machine, see section 6.4, has shown that there are higher harmonics occurring due to saturation, in particular for the machine of Fig. 5.12. If saturation is considered, then most of the unassigned spectral lines of the noise peaks can be computed. A comprehensive approach where the radiated noise is determined with numerical means is presented in chapter 8. These frequencies are considered there and, again, the computed noise results are compared to measurement results. Note that this grave influence of the saturation fields on the noise spectrum is typically only present for two pole machines. A reliable analytical approach for the determination of the amplitude of these magnetic field components and thus the sound pressure values has not yet been found by the author. Other sources for the noise peaks are not quite clear yet and have to be determined in further investigations.

Nevertheless, a good match can be seen for critical noise peaks, meaning that the results from the analytical computation are good means to pinpoint induction machines with critical noise behaviour.

# 6 AXIAL RECONSTRUCTION OF STRESS WAVES

For three dimensional structural analyses of induction machines the stresses acting on the stator teeth in the air gap have to be determined. The skewing of the rotor bars, a common method to reduce harmonics of the torque, has influence on the characteristics of the magnetic field harmonics in the axial direction of the air gap and this also results in a variation of the stresses in axial direction. To consider its influence properly, a three-dimensional model of the electrical machine has to be set up [65]. However, extensive efforts are required to set up an adequate three-dimensional finite element model. As for noise investigations, the magnetic field and in particular its harmonics are of interest. Therefore, a very fine mesh is needed in the air gap, which leads to models that require a large amount of memory for the finite element simulation. The modelling of the air-gap mesh is even more complicated if the machine is skewed, especially if a consistent mesh is required in the simulation process. To compute the magnetic field for the nominal operating point, the rotor rotation has to be considered in a transient simulation. First of all, this requires an appropriate coupling of the rotating and non-rotating parts. Furthermore, for acoustic simulations mostly the steady state result is of interest. This is reached not until the transient effects have decayed. For this, and to obtain a proper frequency resolution of the steady state magnetic field, a large number of time steps is needed. This results in high computational costs and long simulation times.

An alternative method enabling faster simulations of skewed electrical machines, especially if considering rotor movement, is the multi-slice method. This method couples several two-dimensional models (slices) via an electric circuit. Hence, no fields in axial direction are computed and the end-region effects are not considered. However, for noise investigations this method is an adequate means as the most significant magnetic field components are those in radial and azimuthal direction. Hence, with this method the modelling of the machine can be carried out more easily and, beyond this, the computational costs to determine the magnetic field in the air gap are not as large as for three-dimensional models. After computing the magnetic field in the air gap, the stress acting on the stator teeth can be determined. However, a solution exists only at distinct axial position, i.e. where the slices are modelled. In this chapter, an investigation of the variation of the magnetic field and thus the forces in axial direction is carried out. This is necessary if the forces have to be applied to a three-dimensional structural model. A wrong characteristic may lead to a wrong result for the vibration.

In a first step, to get an idea of the variation of the flux in axial direction, the analytical approach presented in chapter 3 is taken and modified to account for the skewing. It is shown that spatial ordinal numbers in axial direction for each magnetic field component can be computed which determine their characteristic in axial direction.

In a next step the application of the multi-slice method to simulate skewed induction machines and compute the rotating force waves necessary for further investigations on the noise behaviour is presented. The results of multi-slice simulations with different numbers of slices and the problems of the interpolation in axial direction, resulting in a wrong estimation of the force distribution, will be discussed. It is then shown that by taking the analytically determined spatial ordinal numbers in axial direction this problem can be overcome. To validate this approach a three-dimensional model has been set up which will be shown in a last step. This novel approach has been presented at the 14th Biennial IEEE Conference on Electromagnetic Field Computation (CEFC) [102] and has been published in [105].

## 6.1 Analytic approach to determine the magnetic field distribution

The magnetic induction $B$ in the air gap for slotting and winding fields can be computed as follows, see also chapter 3:

$$B_r(\varphi,t) = \Lambda(\varphi,t)V_\delta(\varphi,t). \tag{6.1}$$

The magnetic field in the air gap shall be decomposed into its harmonics with a Fourier decomposition which leads to the following relation:

$$B(t,\varphi) = \sum_\nu \sum_\lambda \hat{V}_{\delta_\nu} cos(\nu\varphi - 2\pi f_\nu t - \gamma_\nu)\hat{\Lambda}_\lambda cos(\lambda\varphi - 2\pi f_\lambda t - \gamma_\lambda) \tag{6.2}$$

where $\hat{V}_{\delta_\nu}$ now denotes the amplitude of the magneto-motive force component. The subscript $\delta$ is omitted from now on. The affiliation of the amplitudes, angular frequencies and phase angles to the corresponding spatial orders is denoted by their indexing with the relevant spatial order numbers $\nu$ or $\lambda$, cf. chapter 3.

A breakdown to winding fields (3.14) and parametric fields (3.15), which has been introduced in 3.1.3, is not necessary for this investigation. This means that (6.2) denotes the sum of (3.14) and (3.15).

The following derivation only considers the permeance variations due to the rotor and stator slotting. For magnetic fields arising from nonlinear effects or eccentricities, appropriate formulations have to be derived.

The harmonics $V_\nu$ and $\Lambda_\lambda$ are now further split up according to their origin, either stator, specified by the subscript $S$, or rotor, stated by the subscript $R$:

$$V_S = \sum \hat{V}_{\nu_S} cos(\nu_S\varphi_S - 2\pi f_{\nu_S} t - \gamma_{\nu_S}), \tag{6.3}$$

$$V_R = \sum \hat{V}_{\nu_R} cos(\nu_R\varphi_R - 2\pi f_{\nu_R} t - \gamma_{\nu_R}), \tag{6.4}$$

$$\Lambda_S = \sum \hat{\Lambda}_{\lambda_S} cos(\lambda_S\varphi_S - \gamma_{\lambda_S}), \tag{6.5}$$

$$\Lambda_R = \sum \hat{\Lambda}_{\lambda_R} cos(\lambda_R\varphi_R - 2\pi f_{\lambda_R} t - \gamma_{\lambda_R}). \tag{6.6}$$

Since, due to the skewing, the azimuthal coordinate $\varphi$ is different for stator and rotor permeance and magneto-motive force waves, appropriate coordinates $\varphi_S$ and $\varphi_R$ are introduced. The skewing is defined as the twisting of the stator or the rotor bars along the axial direction, denoted with the coordinate $z$, at a distinct angle. Depending on whether the stator or the rotor bars are skewed, either $\varphi_S$ or $\varphi_R$ is a function of the axial coordinate. The machine that has been investigated here has a rotor that is skewed for one stator slot pitch. The variation of the rotor angle $\varphi_R$ in $z$-direction can be stated by the following relation

$$\varphi_R = \varphi_S - \gamma' z \tag{6.7}$$

where $\gamma'$ stands for the slope, a function of the number of stator teeth $N_S$ and the length $l_{Fe}$ of the iron core stack, and is computed by

$$\gamma' = \frac{2\pi}{N_S l_{Fe}} \tag{6.8}$$

for the investigated machine, as there the rotor is skewed for one stator slot pitch. This relation indicates that the harmonics of the permeance and the magnetomotive force arising from the skewed rotor part are characterized by an additional spatial order in axial direction.

The resulting harmonics of the magnetic flux density are now computed by the product of the permeance waves with the magnetomotive force waves of the stator or of the rotor. E.g. the product of the magnetomotive force wave $V_S$ and the permeance wave $\Lambda_R$ results in the magnetic induction for the stator-rotor fields with index $SR$. Thus, after applying the addition theorem, the following results are obtained:

stator-stator fields $B_{SS}$

$$\begin{aligned} B_{SS} = \sum_{\nu_S}\sum_{\lambda_S} \hat{V}_{\nu_S}\hat{\Lambda}_{\lambda_S}\frac{1}{2}[&\cos((\nu_S-\lambda_S)\varphi_S - (2\pi f_{\nu_S} - 2\pi f_{\lambda_S})t - (\gamma_{\nu_S}-\gamma_{\lambda_S})) \\ &+\cos((\nu_S+\lambda_S)\varphi_S - (2\pi f_{\nu_S} + 2\pi f_{\lambda_S})t - (\gamma_{\nu_S}+\gamma_{\lambda_S}))] \end{aligned} \tag{6.9}$$

stator-rotor fields $B_{SR}$

$$\begin{aligned} B_{SR} = \sum_{\nu_S}\sum_{\lambda_R} \hat{V}_{\nu_S}\widehat{\Lambda}_{\lambda_R}\frac{1}{2}[&\cos((\nu_S\varphi_S-\lambda_R\varphi_R) - (2\pi f_{\nu_S} - 2\pi f_{\lambda_R})t - (\gamma_{\nu_S}-\gamma_{\lambda_R})) \\ &+\cos((\nu_S\varphi_S+\lambda_R\varphi_R) - (2\pi f_{\nu_S} + 2\pi f_{\lambda_R})t - (\gamma_{\nu_S}+\gamma_{\lambda_R}))] \end{aligned} \tag{6.10}$$

rotor-stator fields $B_{RS}$

$$\begin{aligned} B_{RS} = \sum_{\nu_R}\sum_{\lambda_S} \hat{V}_{\nu_R}\hat{\Lambda}_{\lambda_S}\frac{1}{2}[&\cos((\nu_R\varphi_R-\lambda_S\varphi_S) - 2\pi f_{\nu_R}t - (\gamma_{\nu_R}-\gamma_{\lambda_S})) \\ &+\cos((\nu_R\varphi_R+\lambda_S\varphi_S) - 2\pi f_{\nu_R}t - (\gamma_{\nu_R}+\gamma_{\lambda_S}))] \end{aligned} \tag{6.11}$$

and rotor-rotor fields $B_{RR}$

$$B_{RR} = \sum_{\nu_R} \sum_{\lambda_R} \hat{V}_{\nu_R} \hat{\Lambda}_{\lambda_R} \frac{1}{2} [\cos((\nu_R - \lambda_R)\varphi_R - (2\pi f_{\nu_R} - 2\pi f_{\lambda_R})t - (\gamma_{\nu_R} - \gamma_{\lambda_R})) + \cos((\nu_R + \lambda_R)\varphi_R - (2\pi f_{\nu_R} + 2\pi f_{\lambda_R})t - (\gamma_{\nu_R} + \gamma_{\lambda_R}))] \quad (6.12)$$

The sum of these magnetic field harmonics yields the resulting magnetic induction in the air gap:

$$B(t, \varphi, z) = B_{SS} + B_{SR} + B_{RS} + B_{RR} \quad (6.13)$$

which now also describes its variation in axial direction.

The frequencies and spatial orders in azimuthal direction of the rotor and stator magnetomotive forces and the corresponding slotting fields are obtained by known relations, which can be taken from [68], [80] and have also been presented in chapter 3. With the relation for the rotor angle specified in (6.7), the spatial ordinal number in axial direction can now be computed for each harmonic. For example, for the stator-rotor fields, the term $(\nu_S \varphi_S \pm \lambda_R \varphi_R)$ can be transformed as follows

$$(\nu_S \varphi_S \pm \lambda_R \varphi_R) = (\nu_S \pm \lambda_R)\varphi_S \mp \lambda_R \gamma' z. \quad (6.14)$$

Thus the spatial ordinal number $k$ in azimuthal direction, with the index $SR$ for the stator-rotor fields, yields

$$k_{SR} = \nu_S \pm \lambda_R \quad (6.15)$$

and the spatial order $k_z$ in axial direction is computed as

$$k_{z_{SR}} = \mp \lambda_R \gamma' \quad (6.16)$$

For the other fields, the transformation has to be applied accordingly which results in the following spatial ordinal numbers in axial direction:

$$k_{z_{RS}} = \mp \nu_R \gamma', \quad (6.17)$$

$$k_{z_{RR}} = -(\nu_r \mp \lambda_R)\gamma'. \quad (6.18)$$

For the investigated machine, stator-stator fields do not have any dependencies in axial direction.

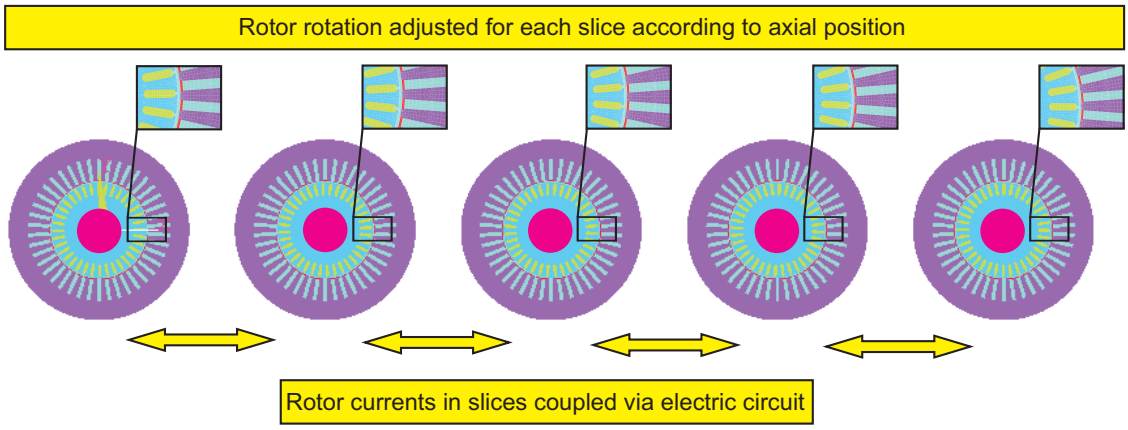


Figure 6.1: FEM multi-slice model of squirrel cage induction machine with five slices

## 6.2 Finite element simulation with the multi-slice method

The electromagnetic field computation to determine the magnetic flux density $B$ is carried out with a finite element simulation using the multi-slice method [24], [57]. This method is an established and improved technique for investigations of skewed electrical machines, e.g. the estimation of the load-dependent mean torque. End effects and effects in axial direction cannot be taken into account with this model but these are negligible for noise computation purposes. Investigations on end-winding leakage and axial flux confirming this assumption are presented for example in [48].

For multi slice simulations, the axial dimension is divided into several slices, each represented by a two-dimensional model with the corresponding rotor teeth position due to the skewing. The currents in the rotor bars of each slice are coupled with an electric circuit. A schematic overview for a five slices multi-slice model is shown in Fig. 6.1. The investigated induction machine is skewed for one stator slot pitch.

The electromagnetic simulation with the multi-slice method delivers the magnetic flux density in the air gap of each slice, which is needed to compute the mechanical stress acting on the stator core stack.

The skewing of the rotor leads to variations of the magnetic flux in axial direction. For the fundamental wave, this is linear with the skewing. For higher harmonics of the magnetic field, the variations can have a multiple periodicity of the skewing determined with the spatial ordinal numbers derived in the previous section.

However, the multi-slice method only delivers the results for the magnetic field for a few number of slices at distinct axial positions, which can be denoted as the sampling points of the magnetic field characteristic in axial direction. Due to the low number of these sampling points, aliasing and leakage effects occur [58]. Therefore, common interpolation techniques deliver wrong results for the force distribution. The problem can be avoided, if the exact spatial ordinal numbers in axial direction are known.

## 6.3 Reconstruction of the magnetic field distribution

With the introduced analytic determination of the spatial orders and frequencies of the magnetic induction and the results of the multi-slice simulation, the distribution of the magnetic field and thus the mechanical stress in the air gap can now be reconstructed.

The variation of the magnetic field in axial direction can be determined by a harmonic superposition

$$\hat{B}(k, f_k, z) = \sum_{i=1}^{m} C_{1_i} cos(k_{z_i} z) + C_{2_i} sin(k_{z_i} z) \tag{6.19}$$

with the known spatial orders $k_{z_i}$ , the unknown amplitudes $C_{1_i}$ and $C_{2_i}$, and $m$ denoting the number of spatial orders occurring at a distinct harmonic. Regarding the higher harmonics only the stator-rotor and rotor-rotor fields have the same frequencies. This is the case e.g. for the rotor slot harmonics for which

$$f_{\nu_S} = f_p = f_{\nu_R}. \tag{6.20}$$

The resulting frequencies $f_k$ of the magnetic field $B_k$ are then obtained as:

$$f_{k_1} = f_p + f_{\lambda_R} \qquad \text{or} \qquad f_{k_2} = f_p - f_{\lambda_R}. \tag{6.21}$$

For $f_{k_1}$, the following two spatial ordinal numbers arise:

$$k_{z_1} = -\lambda_R \gamma' \qquad k_{z_2} = (\nu_R - \lambda_R)\gamma' \tag{6.22}$$

and thus

$$\hat{B}(k_1, f_{k_1}, z) = C_{1_1} cos(k_{z_1} z) + C_{2_1} sin(k_{z_1} z) + C_{1_2} cos(k_{z_2} z) + C_{2_2} sin(k_{z_2} z) \tag{6.23}$$

For the the multi-slice results, a two-dimensional Fourier transformation has to be carried out, the first according to time and the second according to the azimuthal coordinate. As a result, the amplitudes $\hat{B}_{k_j}(k, f_k)$ for specific frequencies $f_k$ and spatial orders $k$ in azimuthal direction are obtained for each slice $j$ and thus in discrete points in axial direction. The frequencies and spatial orders can now be related to the analytically determined frequencies and spatial orders in azimuthal direction. This enables the correlation of the spatial orders in axial direction to the computed amplitudes of the magnetic flux density of the multi-slice solution.

With the computed amplitudes of the multi-slice simulation, the unkown coefficients can be determined with a least square method [44]. To get a unique solution, a multi-slice model of at least four slices is necessary. With this method the signal can be reconstructed from non equidistant points, too. This can be important, because first of all it is not always possible to model equidistant slices and, furthermore, it is beneficial to shift the slices at distinct positions to avoid sampling at points where a zero-crossing of a magnetic field harmonic can occur making the reconstruction problematic.

To sum up, this approach enables the reconstruction of the magnetic field in the air gap to obtain the variation in axial direction with the help of analytical solutions. For this approach, the field components taking into account either stator or rotor slotting have been considered. The interaction of the slotting permeance waves also leads to distinct magnetic field components. However, their spatial ordinal numbers and frequencies are included in those of the stator-rotor and rotor-stator components, respectively. The reconstruction therefore also takes these components into account.

## 6.4 Numerical example

The electromagnetic simulation of an induction machine with 42 stator slots, 36 rotor slots, a pole pair number $p = 1$ and skewed for one stator slot pitch is carried out with a 2D multi-slice model. A non-linear, transient simulation has been carried out for the nominal operating point with a stator current of 150 A ($f_1 = 50$ Hz) and with a rated slip $s = 0.3\%$ (rotor speed of 2991 rpm). This is the same machine introduced in section 5.1. More detailed machine parameters are listed in appendix A.5.

The electromagnetic simulation has been carried out with two models, one with four slices and one with five slices in order to compare the results and thus validate the introduced analytic approach.

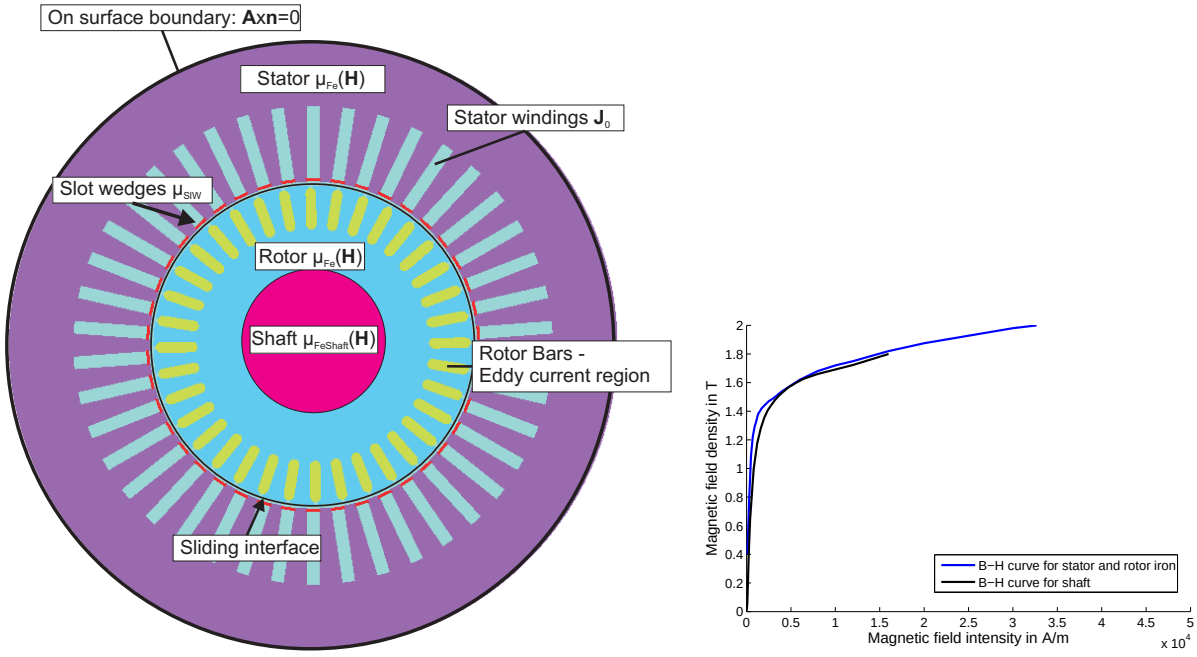


(a) FEM material parameter (b) B-H curves

Figure 6.2: Material parameters for FEM multi-slice model

The model is discretized with quadrilateral and triangular elements of second order and

the $\mathbf{A}, v-\mathbf{A}$ formulation see section 4.3 is used to solve the nonlinear transient eddy current problem for the nominal operating point. The applied materials and boundary conditions are sketched in Fig. 6.2. For the stator and rotor the permeability $\mu_{Fe}$ is defined as a function of the magnetic field intensity $\mathbf{H}$. For the shaft, the nonlinear permeability $\mu_{FeShaft}(\mathbf{H})$ is used and the permeability of the slot wedges is set to a constant $\mu_{SlW}$. At the stator windings, the current density $\mathbf{J}_0$ is applied for a three phase system with two layers. The rotor bars are defined as the eddy current region. On the boundary of the stator no flux is entering the surface and therefore $\mathbf{A} \times \mathbf{n} = \mathbf{0}$. To consider the rotor movement, a sliding interface is applied in the air gap between the rotating and non-rotating parts. In every time step, the geometry modification due to the rotation is considered by linear constraint equations [47], [60].

For each time step, the stator currents are applied appropriately and the rotor movement is considered by adjusting the rotor position according to the rotational velocity. Only steady state results are relevant and in order to reduce the transient oscillation and thus to reach the steady state with less computation efforts, an approximate frequency domain technique [74] is used to estimate the initial conditions for the simulation.

The time step $\Delta t$ and the number of time steps to be computed depend on the desired frequency resolution and the corresponding period $T$. A method to reduce the number of time steps and therefore the computational costs has been introduced in [61]. The transient simulation is truncated and leakage and aliasing effects are allowed. The correct spectrum of the magnetic flux density is reconstructed by determining the spectral lines analytically and computing the corresponding amplitude values. The simulation delivers the magnetic flux density in the air gap of each slice. In Fig. 6.3, the interpolated and reconstructed variation of the magnetic induction in axial direction for the second slot harmonic with 3639.3 Hz and a spatial ordinal number of $p+gN_R = 73$ in azimuthal direction are depicted. The direct interpolation has been performed with a cubic spline method. The analytic approach delivers the spatial ordinal numbers $k_{z_{SR}} = -2\pi \cdot 2.0555$ 1/m and $k_{z_{RR}} = -2\pi \cdot 2.084$ 1/m in axial direction for the reconstruction algorithm. The maximal detectable spatial ordinal number $k_{z_{4Sl}}$ for the model with four slices is, applying the Shannon theorem, $2\pi \cdot 1.7986$ 1/m and for five slices $2\pi \cdot 2.398$ 1/m. The aliasing effect that occurs for the four slices multi-slice model can be seen for the interpolated solution in Fig. 6.3. The variation yields a completely different axial behaviour as compared to the directly interpolated solution for five slices. The reconstructed results themselves, also depicted in Fig. 6.3, match very well. The slight deviations that occur arise from the different accuracy of the multi-slice models due to the different number of slices. The deviations compared to the direct interpolated solution, however, are strong. It is interesting to note that the direct interpolation of the five slices results also delivers a wrong variation, although no aliasing occurs.

After determining the magnetic field harmonics, the surface force distribution on the stator side of the air gap is computed from (A.2) and (A.2) in appendix A.1 in the frequency domain. Thus, the errors occurring with the direct interpolation method result in a wrong estimation of the force distribution as can be seen in Fig. 6.4 showing the surface force distribution for the second slot harmonic at 3589.3 Hz for the interpolated multi-slice

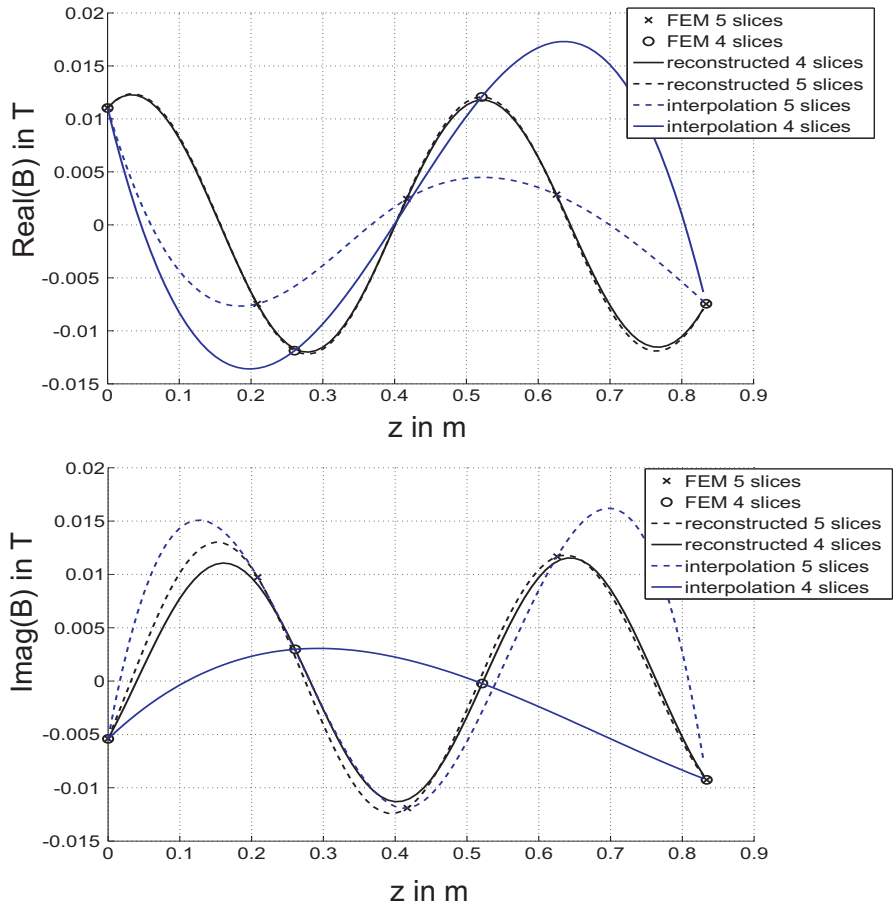


Figure 6.3: Characteristic of the magnetic flux density at a frequency of 3639.3 Hz and with a spatial order in azimuthal direction of 73 for the interpolated and reconstructed simulation results

results and for the reconstructed results of the four slice model.

## 6.5 Validation with 3D model

To validate the previously introduced method, a nonlinear, transient electromagnetic simulation of a three-dimensional model of the induction machine has been carried out, since measurements of the flux density in the air gap are very complex. A sketch of the model is depicted in Fig. 6.6.

The model has been set up with a consistent mesh with an element division of 12 in axial direction. In the air gap, special elements connect the skewed rotor and the stator. A hexahedral element has therefore been divided into a pyramid element with the nodes (2,6,7,3,8) and tetrahedral elements with the nodes (1,4,5,2), (2,8,5,6) and (2,4,8,3) as

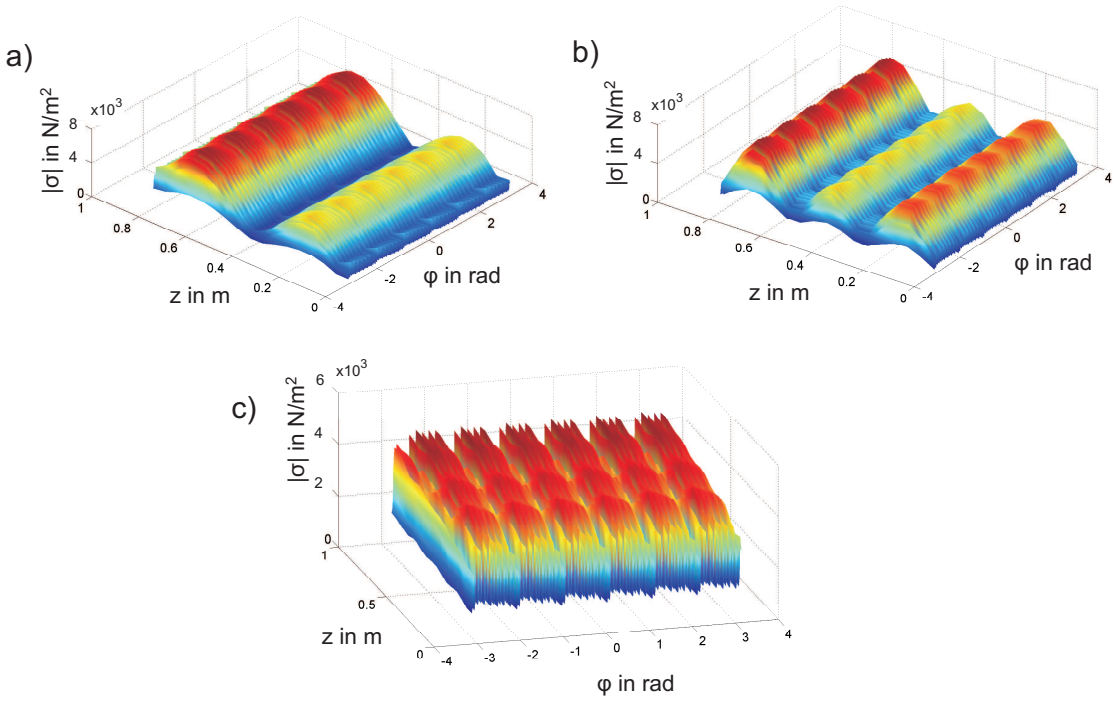


Figure 6.4: Surface force distribution at the stator side of the air gap for a frequency of 3589.3 Hz a) direct interpolated solution for 4 slices b) direct interpolated solution for 5 slices c) reconstructed solution for 4 slices

depicted in Fig. 6.5. In particular, only second order edge elements have been used, and the simulation has been carried out applying the $\mathbf{A}, v - \mathbf{A}$ formulation, see section 4.3. The same material properties as for the multi-slice model are used. On the boundary of the model again $\mathbf{A} \times \mathbf{n} = \mathbf{0}$ as no flux passes the surface. The rotor bars have been modelled together with the end ring to account for end region effects and both are part of the eddy current domain. On both ends of the machine, a layer of air encloses the machine model. The influence of the shaft has been neglected for this investigation, since, at short circuit operation, very low flux is going through it. Hence, this part is omitted and the outer boundary surface is comprised by the inner rotor surface.

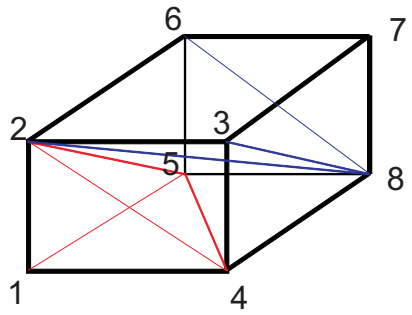


Figure 6.5: FEM multi-slice model of squirrel cage induction machine with five slices

Since the consideration of the rotor rotation in 3D is problematic (mesh interface be-

tween skewed rotor and stator), the simulation has been conducted for a short circuit operating point, with fixed rotor. Thus the effects of the rotor currents and therefore of the resulting fields are taken into account. To reduce the computation time, the method in [61] has been applied.

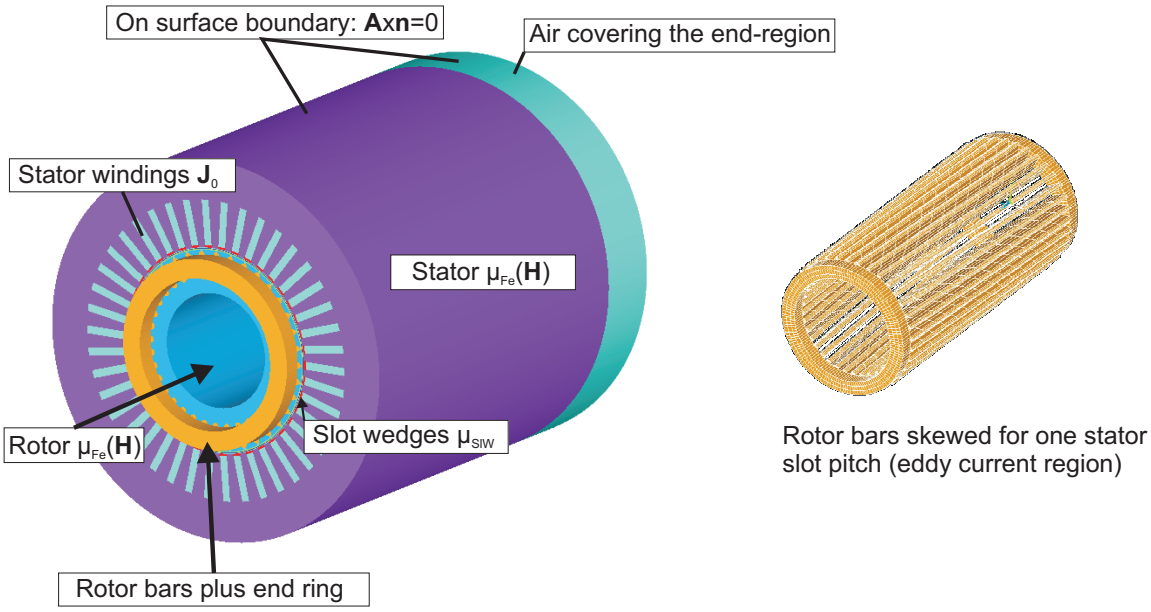


Figure 6.6: FEM multi-slice model of squirrel cage induction machine with five slices

Besides the 3D simulation, a multi-slice simulation with 5 slices at short circuit operation has also been performed and the introduced reconstruction method has been applied, thus enabling a comparison of the two results. In Fig. 6.7, the magnetic flux density of the 3D solution along the axial direction for the spatial ordinal number of 73 in azimuthal direction are depicted. For the reconstruction of the multi-slice results, the spatial orders $k_{z_{SR}} = \pm 2\pi \cdot 2.033$ 1/m and $k_{z_{RR}} = \pm 2\pi \cdot 2.068$ 1/m have been computed with the analytic approach. The result is also depicted in Fig. 6.7. It can be seen that the 3D results yield the same variation. The slight deviation of the amplitude can be explained by the coarser mesh, the consideration of the end rings and the occurrence of an axial flux component in the 3D model.

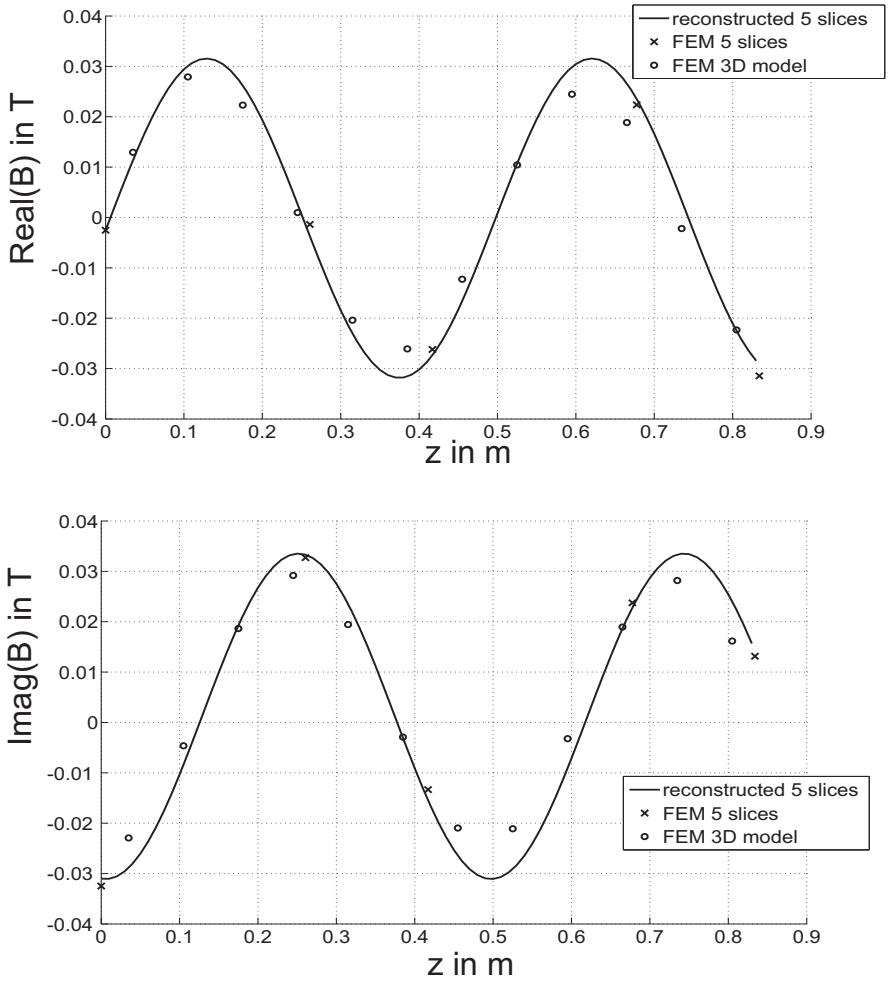


Figure 6.7: Reconstructed characteristic and results of 3D simulation of the magnetic flux density in axial direction for a frequency of 50 Hz and a spatial order in azimuthal direction of 73

# 7 INFLUENCE OF DIFFERENT ROTATING STRESS WAVES ON THE 3D VIBRATIONAL BEHAVIOUR

As presented in chapter 5, the analytical approach for noise computation is based on the decomposition of the air gap field into its harmonics and the stress wave components can then be determined with Maxwell's stress tensor. The vibration and noise are then computed with simple structural and acoustical models by the contributions of each stress wave. With this decomposition, the assignment to the causes (slotting, saturation, etc.) of problematic noise peaks can be retained. This idea of investigating the structural and then acoustical response of distinct force wave components has also proved to be of value when using numerical methods to compute three dimensional machine models [79], [17].

One weak point of the analytical structural models is that they typically do not comprise all structural details (stator, rotor, housing, etc.) and they are mainly derived for two-dimensional considerations. It has been shown in chapter 5, that such models do not account for all vibrations, since additional resonances and mode shapes occur for three-dimensional structures.

In the following an investigation of the influence of distinct unit stress wave components on the three-dimensional structural vibration behaviour of a squirrel cage induction machine is investigated. The analysis shows how different stress wave components affect the structural vibration behaviour. The machine is the same as the one introduced for the electromagnetic field simulation in chapter 6 and the results obtained from the electromagnetic field simulation determine the frequencies and spatial ordinal numbers taken for this investigation.

The chapter is arranged into two main parts. First, the stress wave components which are of interest in the course of this analysis are defined. In a next step, the three-dimensional structural model is presented and the computed structural responses to the different stress wave components are compared and discussed.

This work has been presented at [103] and will be published in [104]. A special focus lies on components with large spatial ordinal numbers which may have large amplitudes as shown in section 5.1 and chapter 6. Following up on the findings of [97], it is shown in this chapter that, for stresses with spatial ordinal numbers near the number of teeth, an undersampling occurs and new components with lower spatial ordinal numbers arise. These components contribute to the vibration and need to be considered in the noise computation of electrical machines. In a next step, the influence of the variation of the stresses in axial direction is investigated. The obtained structural response is compared to that with a uniform distribution in axial direction. Furthermore, stress waves with a spatial ordinal number of one are investigated, as this may lead to significant vibrations, especially when acting on the rotor side. For this, some considerations regarding the frequency of the forces

acting on the rotating rotor have to be made.

## 7.1 Definition of stress wave components

The forces crucial for the noise computation of electrical machines are those acting on the tooth tips of the stator or rotor teeth. These arise from the magnetic field in the air gap and can be determined with the Maxwell stress tensor (2.21). Forces acting in the iron (magnetostriction) or at the inner side of the teeth are neglected, because their influence is considered to be small compared to the forces acting on the tooth tips, especially for small machines [10].

For this investigation, the simulation results of the magnetic field in the air gap (along the whole circumference) are taken from the numerical analysis presented in chapter 6. The magnetic fields have been obtained by a transient finite element multi-slice simulation of the squirrel cage induction machine for the nominal operation point. The skewing of the machine and the rotor rotation have been considered by the application of a multi-slice model.

As only the stationary problem is of interest for the structural analysis, a Fourier transformation of the transient solution along the peripheral angle $\varphi$ from the time domain to the frequency domain $B(t,\varphi) \rightarrow \hat{B}(\omega,\varphi)$ is performed. The mechanical stresses $\hat{\sigma}_r(\omega,\varphi)$ and $\hat{\sigma}_\varphi(\omega,\varphi)$ can then be determined by a convolution in the frequency domain for the radial and azimuthal direction, cf. (A.2) and (A.3).

A common approach is to further decompose the mechanical stress into stress wave components

$$\sigma(n,\varphi,t,z) = \hat{\sigma}(n)cos(n\varphi - 2\pi f_n t - \psi_n(z) - \overline{\psi_n}) \tag{7.1}$$

by carrying out a second Fourier transformation $\hat{\sigma}(\omega,\varphi) \rightarrow \hat{\sigma}(\omega,n)$ [80] with respect to the peripheral angle $\varphi$. This way, a relation between the cause - the magnetic field component - and the effect - the deformation of the structure - can be obtained [42], [79]. The notation also considers the axial variation with the phase angle $\psi_n(z)$. As shown in chapter 6, for the force waves related to the slotting fields, the phase angle $\psi_n(z)$ is determined by the spatial ordinal numbers $k_z$ of the contributing magnetic field components.

As the second Fourier transformation is carried out along the whole azimuthal perimeter, stresses are computed at positions where actually no stresses can occur, i.e. at the positions of the slots where no material (only air) is present. To evaluate the stress wave component acting on the teeth only, a periodic rectangular signal $w(\varphi,z)$ is defined with a period determined by the number of slots, which is zero at the slot positions and one at the teeth positions. The rectangular signal is then multiplied with the stress wave component $\sigma(n,\varphi,t,z)$ leading to a new component $\underline{\bar{\sigma}}(\omega,\varphi,t,z)$

$$\bar{\sigma}(n,\varphi,t,z) = \sigma(n,\varphi,t,z)w(\varphi,z) \tag{7.2}$$

This operation sets the obtained stress values at the position of the slots to zero. These may be nonzero because the field there is not exactly zero (leakage fields). In Fig. 7.1, the stress values $\hat{\sigma}(n)$, not considering the influence of the slots, and the stresses $\hat{\sigma}(n)$, considering the slots, at a frequency $f_n = 1894.6$ Hz with the spatial ordinal numbers $n$, that arise, are depicted. The results in Fig. 7.1 are obtained from the first slice. The spatial

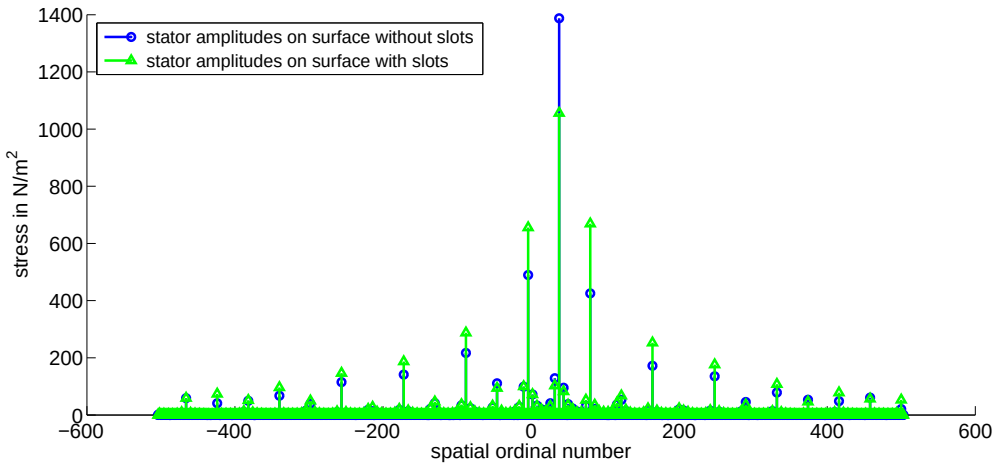


Figure 7.1: Spatial spectra of mechanical stresses at a frequency of 1894.6 Hz

ordinal numbers with or without slots considered are the same. It can be seen that the most striking amplitudes arise for the spatial ordinal number $n = 38$, $n = -4$ and $n = 80$. The multiplication with the rectangular signal $w(\varphi, z)$ now leads to a change of the amplitudes of up to 20%. In particular, an increase of the amplitude for the spatial ordinal number of 4 and a decrease of the spatial ordinal number of 38 can be noted. This phenomenon is discussed in more detail in the following section.

### 7.1.1 Higher order stress waves

In the following, the influence of the sampling of the teeth on distinct stress wave components is investigated. The computed spectrum depicted in Fig. 7.1 for the first slot harmonic at $f_n = 1894.6$ Hz shows that the largest component has a spatial ordinal number of $n = 38$. For the slot harmonic at $f_n = 1794.6$ Hz this would be $n = 36$.

The mechanical stress waves according to (7.1) are now set up and impressed on the structural finite element model. For the further investigations, only stress waves with amplitudes of one are considered. In order to impress this signal appropriately on the finite element mesh, first of all the element division in azimuthal direction has to be set appropriately. In Fig. 7.2 the stress wave with the spatial ordinal number $n = 38$ applied on a mesh with six times the number of stator teeth is depicted. The number of sample points is sufficient to avoid aliasing effects, however performing a linear interpolation of the resulting points of the stress signal, as is the case in FEM with linear shape functions,

results in the modulated amplitude shown in Fig. 7.2. This effect is well known, however

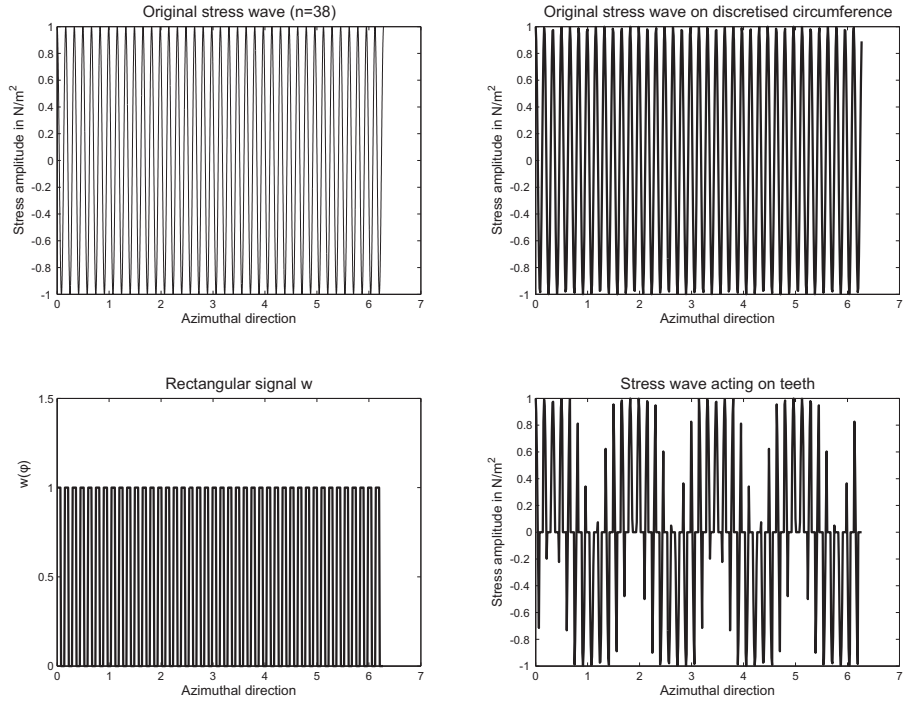


Figure 7.2: Stress wave with a spatial ordinal number n=38 on discretized surface with and without slots

it should be mentioned here because it plays a role especially for higher ordinal numbers. A compromise between computational effort and the occurring error has to be made.

The second and more interesting effect occurring is, as explained above, due to the slots, where no forces are acting. In Fig. 7.2 the resulting stress wave impressed on the 42 stator teeth is depicted. Interestingly, the resulting signal resembles a wave with a spatial ordinal number of $n = 4$. This can be explained by studying the spectra of $\bar{\sigma}$, $\sigma$ and $w(\varphi)$.

In Fig. 7.3 the Fourier transform of the stress wave assuming no slots and the rectangular signal $w(\varphi)$ are shown along with the resulting stress wave acting on the teeth. The multiplication of the two signals in the time domain, thus a convolution in the frequency domain, means that the stress wave with $n = 38$ acting on the teeth now also contains lower and higher ordinal numbers depending on the number of slots. In this special example where $n = 38$ and the number of stator teeth is 42, the effective stress wave has a fundamental wave with the wave number 4 superimposed with higher harmonics. In general, when stress waves with spatial ordinal numbers $n = N_S + \overline{n}$ are applied on the stator teeth, a subharmonic with a spatial ordinal number of $\overline{n}$ arises. If that is low, i.e. $\overline{n} < 6$ the contribution of this stress wave component can not be neglected. When impressing

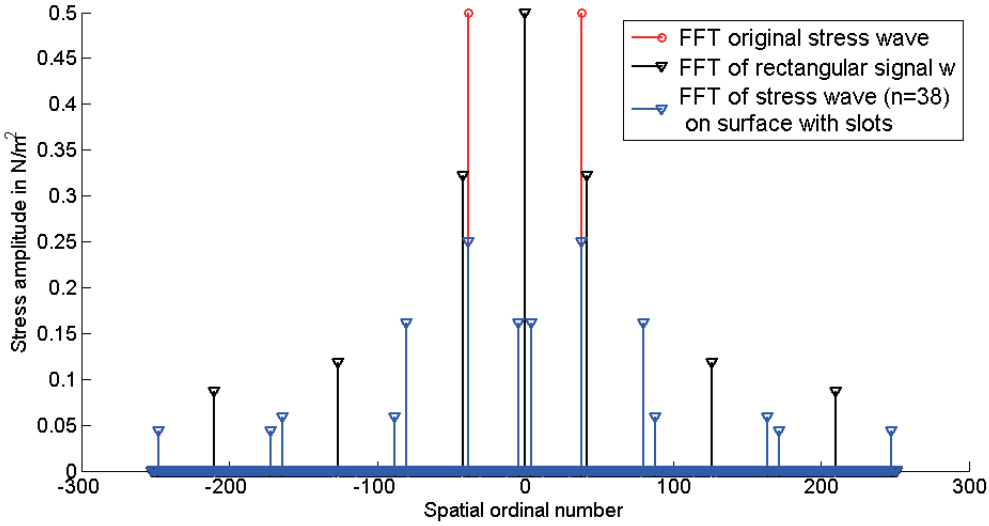


Figure 7.3: Fourier transform of periodic rectangular signal $w(\varphi)$ , of the original stress wave with $n = 38$ and of the stress wave effectively acting on teeth

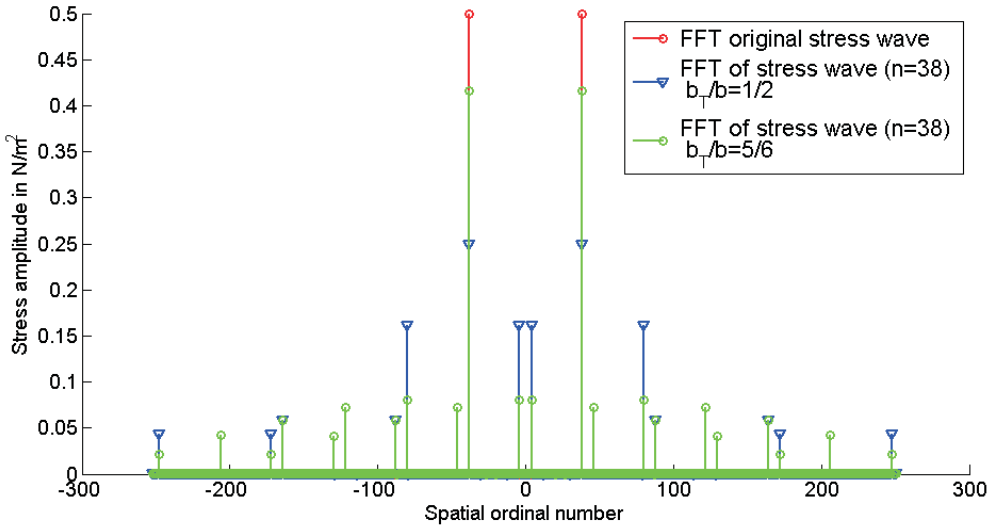


Figure 7.4: Fourier transform of periodic rectangular signal $w(\varphi)$ , of the original stress wave with $n = 38$ and of the stress wave effectively acting on teeth

force waves on the stator core, the main deformation is due to the bending of the yoke and, as outlined in [42], lower ordinal numbers in azimuthal direction thereby result in larger deformation amplitudes than higher ordinal numbers. This means that, because of the fundamental wave occurring, the higher spatial ordinal numbers are of interest when investigating the structural vibration behaviour.

The amplitude of the subharmonic is influenced by the width $b_T$ of the teeth. The broader the teeth compared to the slot width $b$, the more of the higher harmonics occur and the less the amplitude and thus the influence of the fundamental wave is. This is shown in Fig. 7.4 where the resulting stress harmonics for $b_T/b = 1/2$ and $b_T/b = 5/6$ are depicted. The amplitude is nearly halved for the broader teeth.

### 7.1.2 Stress waves with axial variation

A further aspect that influences the force distribution along the teeth not only in azimuthal but also in axial direction is the skewing of the rotor bars where the winding and the permeance vary in axial direction according to the skewing angle. This influences the field and therefore the stress distribution in axial direction. In chapter 6, an approach has been presented to account for the axial variation of the field. There, spatial ordinal numbers in axial direction are determined and a reconstruction method to obtain a valid axial field distribution of the magnetic field is presented.

For the analysis presented here, the field components with an azimuthal spatial ordinal number of $n = 37$ and $n = -41$ are considered. Those lead to a stress component with an azimuthal spatial ordinal number of $n = -4$ (and $n = 78$, which is not of interest here). The field component with $n = -37$ is a rotor slotting field that has spatial ordinal numbers in axial direction of $k_{z1} = -2\pi 1.021$ 1/m and $k_{z2} = -2\pi 1.05$ 1/m. In Fig. 7.5, the results

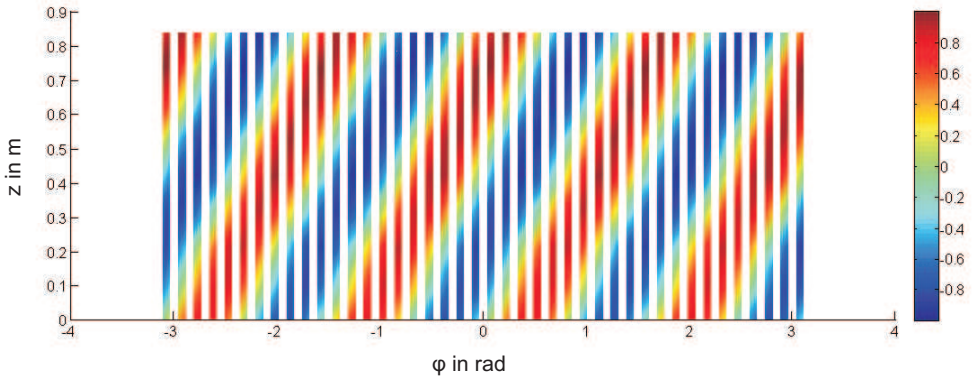


Figure 7.5: Real part of the stress wave with spatial order of four and consideration of skewing

for the mechanical stress wave is depicted. A striking variation in axial direction can be detected. The application of this force distribution may result in a bending of the core stack in axial direction or excite distinct eigenmodes and thus may influence the structural behaviour in a critical way.

### 7.1.3 Stress waves acting on rotor

For the noise computation of electrical machines, mainly the forces acting on the stator teeth play an important role. However some force components on the rotor core may excite the structure to critical vibrations. This is the case, if resulting forces acting on the bearings of the machine appear, which is the case for stress waves with a spatial ordinal number of one.

Due to the even number of slots and the pole pair number of one, force waves with a spatial ordinal number of one only will arise due to the eccentricities of the rotor, see section 3.1.1, which however are unavoidable. Furthermore, slotting leads to subharmonics with $\overline{n} = 1$ for a stress wave with the spatial ordinal number of $n = 37$ acting on 36 rotor teeth.

Due to the rotational movement of the rotor, the frequencies of the stress wave components acting on the rotor have to be determined accordingly. The frequency $f_l^R$ of a mechanical stress wave acting on the rotor surface with a wave number $n_l$ is given as follows:

$$f_l^R = f_{n_l}^S - n_l \, f_m \tag{7.3}$$

where the superscript $R$ denotes the moving coordinate system on the rotor, the superscript $S$ the fixed coordinate system, $f_m$ is the mechanical speed in Hz and $l$ indexes the spatial ordinal number and the frequency in the moving coordinate system. The mechanical stress wave acting on the rotor side, therefore, results in

$$\sigma_l = \hat{\sigma}_l cos(k_l \varphi^R - 2\pi(\, f_i^S - n_l \, f_m)t - \psi_l) = \hat{\sigma}_l cos(n_l \varphi^R - \bar{s_l} 2\pi \, f_i^S t - \psi_l) \tag{7.4}$$

where $\bar{s_l}$ can be derived as

$$f_l^R = f_i^S \frac{f_i^S - n_l \, f_m}{f_i^S} = \bar{s_l} \, f_i^S. \tag{7.5}$$

With the finite element method, the equation of motion in the frequency domain for the rotating part yields the following equation:

$$(-\Omega_R^2 \mathbf{M}_R + \mathbf{K}_R)\hat{\mathbf{u}}_R = \hat{\mathbf{F}}_R \tag{7.6}$$

where $\Omega_R = 2\pi \, f_l^R$ is the excitation frequency. Inserting (7.5) in (7.6) then yields

$$(-\Omega_S^2 \bar{s_l}^2 \mathbf{M}_R + \mathbf{K}_R)\hat{\mathbf{u}}_R = \hat{\mathbf{F}}_R \tag{7.7}$$

with $\Omega_S = 2\pi \, f_i^S$. This means that the mass, i.e. the density, of the rotating structure has to be modified if a rotating force is acting there.

## 7.2 Structural simulation

As mentioned in the introduction, the resonances and the structural response have to be predicted by the structural simulation as accurately as possible to enable a low noise design. In the following, the finite element method, see section 4.4, is used to analyse the structural response of the modelled induction machine. This method enables detailed vibration investigations of complex structures. Although existing computational and memory resources enable simulations of very large models, compromises have to be made between the degree of accuracy of the model, e.g. the heterogeneous composition of the stator core stack, and the computation time, depending on the focus of the simulation. The investigated machine is the squirrel cage induction machine already presented in chapter 6. The machine parameters are listed in appendix A.5.

A three-dimensional model of the squirrel cage induction machine with a cylindrical cooling jacket has been set up. The effect of the water flowing in the cooling jacket is neglected. The stator is mounted via a tight fit in the housing of the machine. Since this work does not focus on rotor-dynamical problems, the modelling of the brush bearings has been simplified and the rotor and housing are connected via a fixed support, i.e. the rotor is supported in the end shields of the housing. The structure is meshed with 20-node hexahedral elements for extensive volumes, and 2nd order solid-shell elements for thin plates, respectively, i.e. the housing of the machine. In Fig. 7.6, a sectional drawing of the discretized model is depicted. The main parts of the machine are of steel, and linear

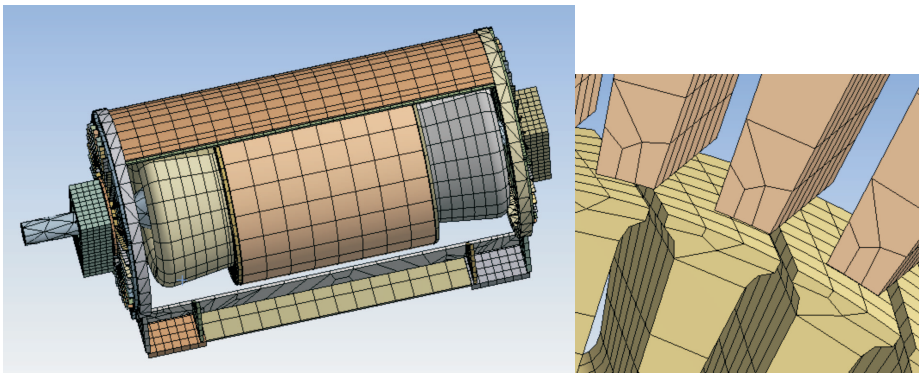

Figure 7.6: Meshed structural model and meshed stator and rotor teeth

mechanical material properties are assumed, since the deformations are small. To consider the influence of the lamination of the stator and rotor core stack, a homogenization with an orthotropic material model has been applied according to [50]. The corresponding material parameters are listed in Table A.4. The insulation of the windings is neglected and linear copper material properties have been chosen.

The simulations are performed in the frequency domain, since only steady state results are of interest. Stress distributions with different wave numbers are set up and the resulting nodal forces $\widehat{\mathbf{F}}$ acting on the stator and rotor teeth are computed and applied as boundary

conditions for the finite element simulation (see section 4.4). The system equation

$$(-\Omega^2\mathbf{M}+\mathbf{K})\hat{\mathbf{u}}=\widehat{\mathbf{F}} \tag{7.8}$$

with the mass matrix $\mathbf{M}$ and the stiffness matrix $\mathbf{K}$ then has to be solved for an excitation frequency $\Omega$ to obtain the nodal displacements $\hat{\mathbf{u}}$. The frequency range of interest is from 1000 Hz to 2200 Hz, because, as shown in section 5.3.1, this is where most problematic excitation frequencies occur. The quasi-static simulations are carried out every 30 Hz. Thus, fourty computations are necessary to get the structural response resulting from one stress wave component. The computational demands are, therefore, very high. Because of this, the structural finite element model is meshed rather coarsely. A more detailed structural modelling is presented in chapter 8 where the vibrations are analysed more closely and afterwards are applied as boundary conditions for an acoustic simulation.

### 7.2.1 Simulation results

The structural investigation focuses on the effect of the possible occurring excitations explained above. Therefore, distinct stress waves with amplitudes of one and with different wave numbers are impressed on the stator and rotor teeth. In Fig. 7.7 and Fig. 7.8, the results for the root mean square velocities on the surface of the investigated machine are plotted against the excitation frequency.

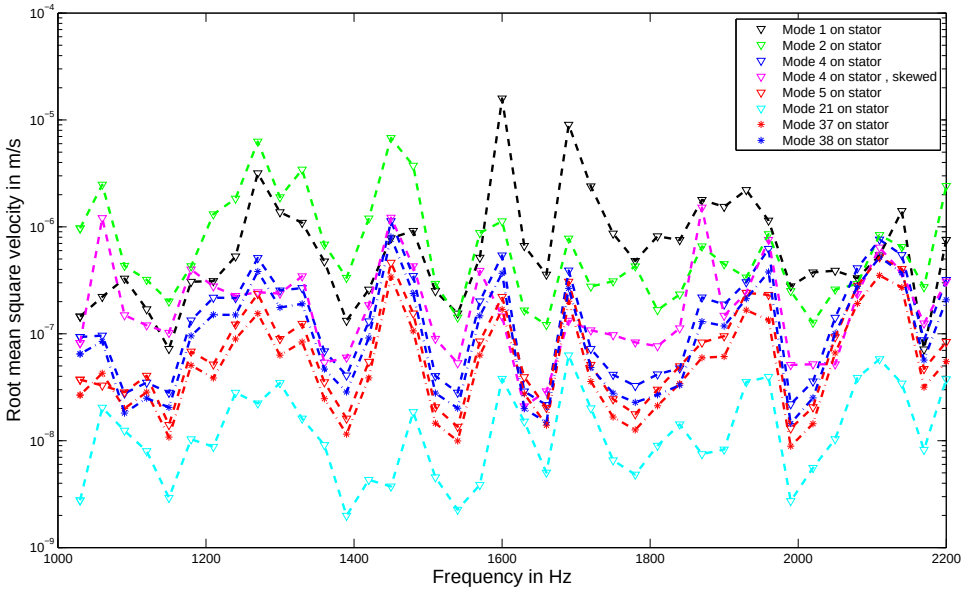


Figure 7.7: Simulation results for the mean square velocity on the surface of the machine due to different stress waves acting on the stator

Generally, it can be said that the higher the order of the force waves, the less is the deformation, i.e. the velocity amplitude on the surface of the machine. The consideration of skewing leads to an axial variation of the force distribution, which results in forced axial bending modes of the stator. In Fig. 7.7 it can be seen that, especially at 1060 Hz and at 1840 Hz, the velocity peaks are larger than for $n = 4$ without skewing. Furthermore, it is striking that the frequency responses of stress waves with $n = 38$ and $n = 37$ resemble the responses for $n = 4$ and $n = 5$, respectively. This can be attributed to the fact that the effective stress wave acting on the teeth consists of a fundamental wave and higher harmonics as explained previously. For $n = 38$ a fundamental wave number of $\overline{n} = 4$ arises and for $n = 37$ a fundamental wave number of $\overline{n} = 5$.

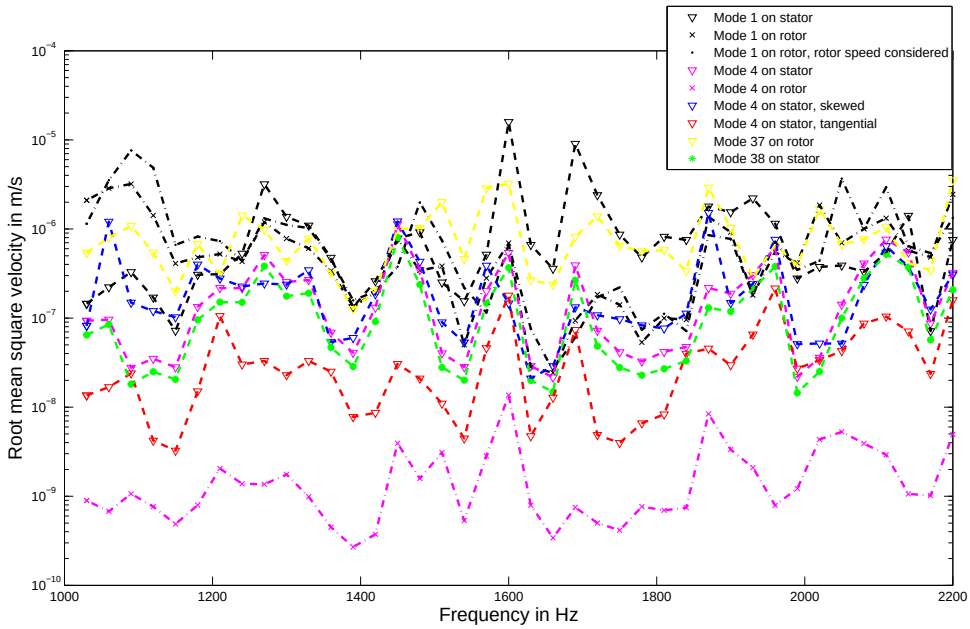


Figure 7.8: Simulation results for the root mean square velocity on the surface of the machine due to different force waves acting on the rotor

Very large velocity values arise from the excitation with a wave number of one, both for excitations on the stator and on the rotor teeth. In Fig. 7.8, the root mean square velocity on the surface for forces acting on the rotor side is depicted. Considering the rotor rotation with a rotor speed of 2991 $\text{min}^{-1}$ for nominal operating point and taking (7.5) into account results in $\overline{s_l} = 0.953$ for an excitation frequency of 1060 Hz and $\overline{s_l} = 0.976$ for 2060 Hz, respectively, for a spatial ordinal number of one. The eigenfrequencies of the rotor are shifted by 49.85 Hz, which can be seen in Fig. 7.8 for example at the excitation frequencies between 1400 and 1500 or between 2000Hz and 2150 Hz, where resonance peaks can be detected.

Stress waves with spatial ordinal number larger than one on the rotor result in velocity

amplitudes three orders of magnitude smaller than those acting on the stator teeth, which can be seen in Fig. 7.8 for a spatial ordinal number of $n = 4$ applied without considering the rotor rotation. Thus, stress waves acting on the rotor may be neglected in the noise computation process. However, for $n = 37$, without considering the rotor rotation, the structural response is in the same order of magnitude as the results for $n = 1$. The same effect occurs, as described above, for $n = 38$ and $n = 37$ impressed on the 42 stator teeth, which results in force waves resembling $\overline{n} = 4$ and $\overline{n} = 5$. The 36 rotor teeth result in an effective stress wave with a fundamental wave with $\overline{n} = 1$. Due to the skewing of the rotor slots, the function $w(\varphi, z)$ now varies in $z$-direction, too and therefore so does the resulting stress distribution. This will result in forced axial bending, similar as for the stress wave $n = 4$ where skewing is considered.

In Fig. 7.8, the structural response for for tangential stress component with $n = 4$ is depicted, too. As shown in [16], too, its contribution to the vibrations is one order of magnitude lower than that of the radial component. The same velocity peaks occur for them as for the radial component, except at 1220 Hz which is caused by the azimuthal component only.

The velocity peaks arising at distinct frequencies lead to the conclusion that eigenfrequencies are excited at these positions. A modal analysis of the structural model, which has been conducted separately, delivers the eigenfrequencies and eigenforms of the mechanical system, describing the structural behaviour at distinct frequencies. The modal simulation delivers more than 300 eigenfrequencies from 1000 Hz to 2400 Hz, i.e., on average, a resonance occurs every 5 Hz.

If the structure is split into three parts - namely stator part (stator core stack with winding), rotor part (rotor core stack and rotor shaft) and the housing part - the overall deformation characteristic can be composed by the contributions of the three parts. The high modal density, for example, can be traced back to the plate bending modes of the housing part. In Fig. 7.7, approximately 8 striking peaks can be identified. More detailed studies of the modal simulation results supported the expectations that these peaks can be attributed to a strong contribution of the stator part at these frequencies. In chapter 8, a more detailed analysis of the modal results is presented.

Summing up, it has been shown that stress waves with higher ordinal numbers in azimuthal direction or with a varying distribution in axial direction can not necessarily be neglected. For further investigations, the influence of the rotor rotation should be considered for higher harmonics that may be problematic when acting on the rotor teeth.

# 8 INFLUENCE OF COMPLEX STRUCTURAL BEHAVIOUR ON THE ACOUSTIC NOISE RADIATION

In the chapter 6, the electromagnetic field computation with the multi-slice method has been presented. An investigation of a skewed induction machine showed that the magnetic field in the air gap leads to stresses with an axial variation of the stresses acting on the stator (and rotor teeth). The influence of such stress distributions as well as stress distributions with larger spatial ordinal numbers has been analysed. In this chapter, the computed stresses of chapter 6 are applied to the stator teeth and detailed structural and acoustic investigations of the skewed induction machine are carried out. The computations for three-dimensional models are carried out with both the finite element method and the boundary element method.

In a first step, the modelling of the structural finite element mesh is presented and the used material parameters are discussed. In a next step, the structural vibration behaviour is analysed with a modal analysis. It is shown that, due to the plate structure, a high modal density occurs, in particular at the housing. It is then shown that, the eigenmodes near the excitation frequency and especially those with the stator contributing to the deformation, obviously influence the surface vibrations of the machine.

To determine the emitted sound pressure, a boundary element model of the induction machine has been set up. Special issues, in particular fictitious eigenfrequencies that may arise are shortly discussed and a workaround is presented. For each excitation frequency, the sound pressure on the surface of the machine and on field points surrounding the machine is computed. At last, the measured noise spectrum introduced in Fig. 5.12 in chapter 5 is compared with the computed numerical results.

This work has also been presented at [98] and has been published in [99]. The aim has been to show the influence of the three-dimensional vibration of the housing on the radiated noise. In the scope of this investigation, some problematic issues are discussed, for example the modelling of the structure and the applied simplifications as well as the used material properties.

## 8.1 Structural vibration computation

To determine the structural vibration results, an appropriate structural model of the investigated induction machine has to be set up first of all. Similarly to the investigations carried out in 7, all relevant structural components are included: the housing of the induction machine comprises the cylindrical cooling jacket of the machine with the water guide rails; the front and back of the machine are encased by plates containing the bearings mounting

the rotor shaft and lamination stack; the laminated stator core is embedded in the cylindrical housing; furthermore the feet of the machine and plates and ribs influencing the stiffness and thus the structural behaviour are modelled. To model the end-windings, some simplifications have been made. They are not modelled separately, but as a homogeneous body connected to the stator core. Not all structural effects concerning the end-windings are considered thereafter, but it is assumed that their influence on the whole machine model can be neglected in the simulation of the noise radiation. Hence, the modelling efforts are reduced enormously.

### 8.1.1 Finite Element Modelling

For the following structural computations a detailed structural model of the induction machine, comprising stator core stack with windings, rotor shaft and core stack with rotor bars and end rings and the housing encasing the structure, is set up. The structural investigations are carried out with 3D finite element simulations. The different parts of the induction machine are dicretized separately. For the finite element mesh of the geometry, solid elements (hexaedra and tetraedra), are used for volumina, i.e. the stator and rotor core stack and the rotor shaft, as well as solid-shell elements for plates. The end-windings, again, are considered as homogeneous bodies. The resulting non conforming meshes are then connected via contact and target elements [6]. This approach enables a much easier set up of the finite element model, because it is not necessary to build consistent meshes between the machine parts with different geometry sizes, which would result in high modelling efforts and a large number of elements and thus computational costs. In Fig. 8.1, the

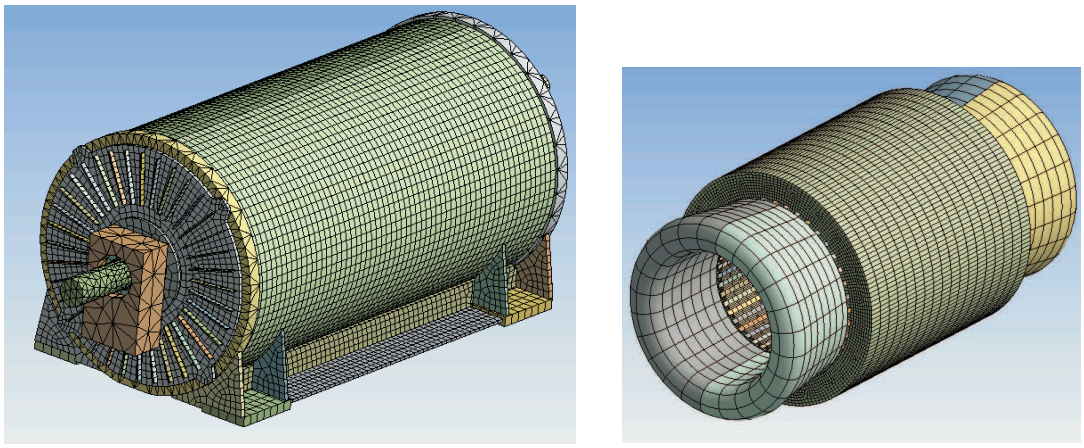

Figure 8.1: Meshed structural model and meshed stator with end windings

structural mesh is shown. It can be seen, that the discretization is much finer compared to the model in chapter 7 (cf. Fig. 7.6), especially for the housing plates but also for the stator core stack to catch all the bending modes. This is important especially for the housing, as the vibration characteristic on the surface influences the emitted sound pressure. The struc-

tural finite element model comprises 419,926 nodes and 155,376 elements, thereof 39,554 are contact elements. Only second order elements are used and the number of degrees of freedom is 1,258,218.

### Material Properties

After discretizing the geometry, proper material models for the different parts of the machine have to be defined. The main parts of the housing are common steel plates and ribs, therefore, a linear, isotropic material model is sufficient for the material assignment.

For the modelling of the laminated stacks some simplifications have to be made, as it is not adequate to model each sheet and connect them via contact models. Recent investigations in [31] and [92] have shown that an orthotropic material model, i.e. with a decreased Young's and shear modulus in axial direction are necessary. These assumptions are supported by experimental investigations carried out in the course of this work [50]. For laminated stacks with and without teeth, structural experimental investigations have been carried out and the eigenfrequencies and mode shapes, in particular in axial direction, have been identified. The resulting frequency response has been presented in Fig. 5.7. This investigation has shown that resonance peaks with eigenmodes that also show an axial deformation characteristic, occur.

To account for this structural behaviour, an investigation of a structural finite element stator model with homogeneous but anisotropic material properties has been carried out, similarly to [77]. A variation of the material parameters, especially the Young's modulus and shear modulus in axial direction, has shown that, with a proper adjustment of these parameters, the measured response could be reproduced with sufficient accuracy.

However, this adjustment has to be carried out for each laminated stack individually. For the investigated squirrel cage induction machine in this work no such investigation has been possible. Nevertheless, to consider the influence of the lower stiffness in axial direction due to the lamination, the anisotropic material parameter set obtained from the investigation in [50] is taken. In the radial and azimuthal directions, the material properties of common steel are used. In axial direction, the Young's modulus and the modulus for shear in this direction have been set accordingly, see Table A.4. Furthermore, for the laminated stacks, a constant damping is assumed. The corresponding damping coefficient has been set to 1%. This is in acceptable agreement with the damping values obtained by the measurements.

Although in [92] it is stated that modelling the windings, embedded in the stator core stacks, as additional masses is sufficient, linear isotropic stiffness of copper has been defined for them. The influence of the insulation and the resin has been not yet been investigated in detail. This is a task for future work on this topic. This is also the case for the end-windings. For this investigation it is assumed that the end-windings mainly influence the structure as additional mass. Their density has been set to $5810\,\mathrm{kg/m^3}$ for the modelled volume (65% copper). The Young's modulus of the end-windings is set to $1.1 \cdot 10^{10}$ Pa.

### 8.1.2 Investigation of the structural behaviour

After setting up the finite element model, the mass matrix $\mathbf{M}$ and the stiffness matrix $\mathbf{K}$ can be computed, see also 4.4. A proper means to investigate the structural behaviour, and get insight in the deformation behaviour of the structure at distinct frequencies, is to perform a modal analysis. For this, the homogeneous solution of (2.38) has to be determined, which leads to an eigenvalue problem for a slightly damped system. One method to determine the appropriate eigenfrequencies is the so-called *QRDAMP* method implemented in *ANSYS* [3], [6]. For this, in a first step, the eigenvalues $\lambda_i$ and eigenvectors $\mathbf{r}_i$ of the undamped problem

$$(\lambda_i \mathbf{M} + \mathbf{K})\,\mathbf{r}_i = 0. \tag{8.1}$$

are computed with the Block-Lanczos method [9]. With the obtained results, a modal transformation, see section 2.4.2 of the damped equation system can be carried out and the following system equations are obtained:

$$\begin{pmatrix} \mathbf{0} & \mathbf{I} \\ \mathbf{I} & \mathbf{R}^T\mathbf{D}\mathbf{R} \end{pmatrix} \begin{pmatrix} \ddot{\mathbf{z}} \\ \dot{\mathbf{z}} \end{pmatrix} + \begin{pmatrix} -\mathbf{I} & \mathbf{0} \\ \mathbf{0} & diag(\omega_i^2) \end{pmatrix} \begin{pmatrix} \dot{\mathbf{z}} \\ \mathbf{z} \end{pmatrix} = \begin{pmatrix} \mathbf{0} \\ \mathbf{0} \end{pmatrix}. \tag{8.2}$$

The eigenvalues and eigenvectors of this problem can then be determined with a general eigenvalue solver ([9], pp. 887ff). With this approach, complex frequencies are obtained. However, the eigenvectors are real since they are derived from (8.1).

A modal analysis computed with this method at a frequency range of 1880 Hz to 1975 Hz showed around thirty eigenvalues and eigenvectors. This high modal density can be attributed to the complex structural geometry model, but especially to the structural behaviour of the plates of the housing which form a wide range of bending modes.

In Fig. 8.2, the modal solution for the structural model is depicted for the computed eigenfrequency of 1588.1 Hz. For the stator, a mode $n = 4$ in azimuthal direction can be identified. This is in accordance with the analytical solution which yields 1592.7 Hz, see appendix A.5. However, plate bending modes occur on the housing with amplitudes five times larger than for the stator.

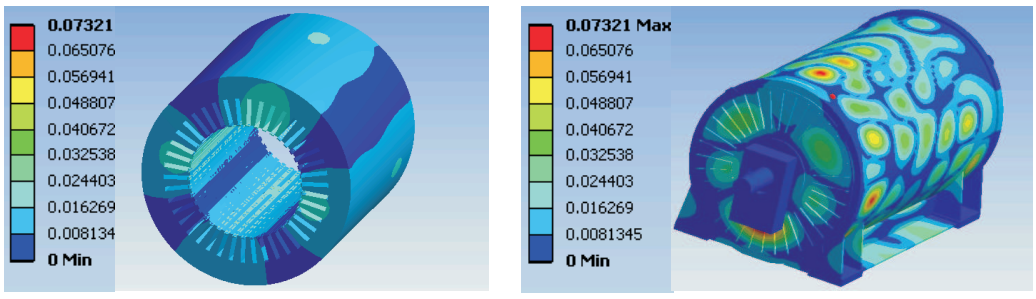


Figure 8.2: Eigenform of the structure at a frequency of 1588.5 Hz

In Fig. 8.3, the deformation characteristic at 1894.6 Hz is depicted. It can be seen that, at this eigenfrequency, the deformation is also dominated by plate bendings of the housing, i.e. the cooling jacket and the plates connecting the feet of the induction machine. These bendings are much more dominant than the deformation of the stator core stack. The

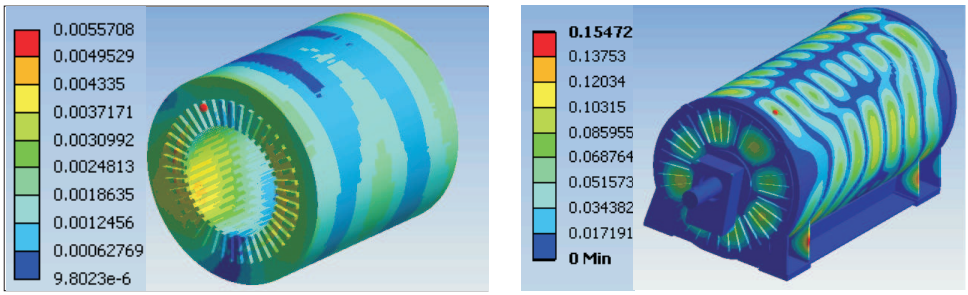


Figure 8.3: Eigenform of the structure at a frequency of 1894.6 Hz

deformation characteristic of the stator itself shows that bending, with two maxima in axial direction occurs. This behaviour can be attributed to the material properties taken for the stator core stack, i.e. the rather low elastic modulus in axial direction compared to the radial and azimuthal directions. This eigenfrequency is particularly problematic, as it coincides with an excitation frequency. The obtained structural response is analysed in the following section.

Summing up, the results of the modal investigation show that strong bending of the plates occurs near the excitation frequencies. For some of these eigenfrequencies, for example at 1588.1 Hz, the stator is also contributing to the eigenform. This fact and its consequence is discussed in the next section, where the structural response due to forces on the stator is computed.

The eigenforms, especially the plate bending modes are influenced very much by the set of chosen material properties. Small changes in the material parameters may lead to different eigenmodes. For future works, further investigations on the material properties and comparisons with measurements are necessary. In particular, these bending modes occurring on the surface of the machine influence the noise radiation strongly, because the surface oscillations result in pressure fluctuations in air and thus in sound. This is discussed in the last section of this chapter.

### 8.1.3 Harmonic analysis at excitation frequencies

The modal analysis has shown that the structural behaviour is dominated by eigenfrequencies with housing deformations as eigenforms. In the following, the structural response to different excitations is computed with the structural finite element model. The deformation characteristic is then analysed and compared to the modal solutions.

Again, only the stationary result is of interest. As the material properties for this structural model include damping, e.g. for the laminated stacks, the following equation for the

quasi-static problem has to be solved with respect to $\hat{\mathbf{u}}$, see also section 2.4.2:

$$(-\Omega^2\mathbf{M} + j\Omega\mathbf{D} + \mathbf{K})\hat{\mathbf{u}} = \hat{\mathbf{F}}. \tag{8.3}$$

As a boundary condition, zero displacement constraints are again assigned to the feet of the induction machine. As a second boundary condition, the electromagnetic stresses acting on the stator teeth are applied with the corresponding frequencies. In Fig. 8.4, the spectrum of the radial stresses in the frequency domain obtained with the approach presented in chapter 6 is shown. It can be seen that the largest stress amplitude arises at 1694.6 Hz, 1794.6 Hz and 1894.6 Hz. The fields contributing the most to this stress components are the fundamental field together with the first slot harmonic field components. For them, spatial ordinal numbers of 34, 36 and 38 arise, cf. appendix A.5. As shown in chapter 7,

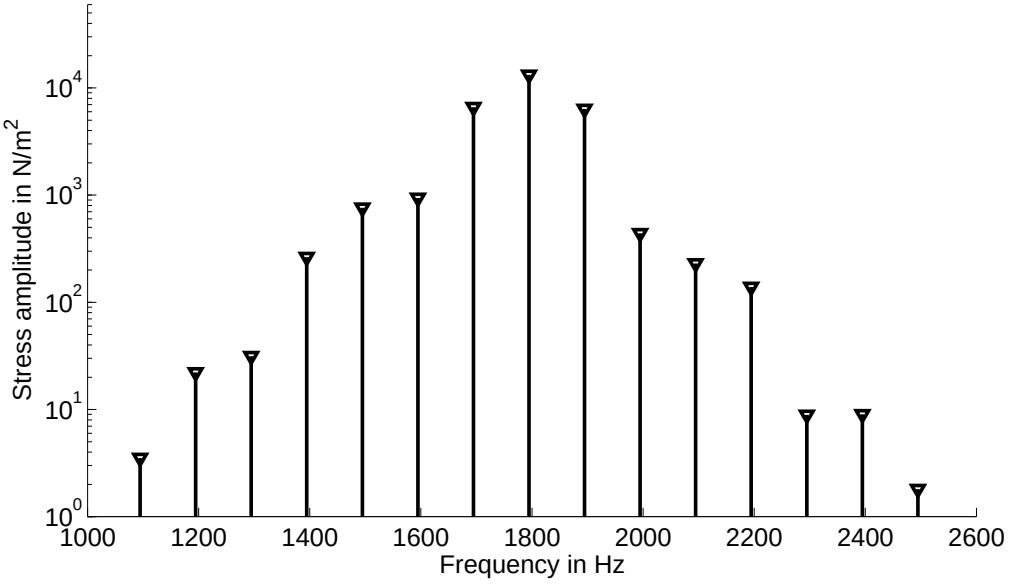


Figure 8.4: Absolute values of the stress amplitudes in radial direction acting on a tooth

the large spatial ordinal applied on the 42 stator teeth leads to sub-harmonics with spatial ordinal numbers of $\overline{n} = 8$ 6 and 4. Thus, at 1894.6 Hz, a larger deformation is expected, since a stress wave component with a large amplitude and a low spatial ordinal number occurs which dominates the stress spectrum.

The structural analysis is carried out for the excitation frequencies $\Omega_i$ =1594.6 Hz, 1694.6 Hz, 1794.6 Hz, 1894.6 Hz, 1994.6 Hz, 2094.6 Hz and 2194.6 Hz. Along with the radial stress components, also the azimuthal ones are applied to the structural model. In Fig. 8.5, the displacement results of the induction machine at 1794.6 Hz and 1894.6 Hz are now depicted, i.e. the real part of the sum of the displacement vectors. It can be seen that the largest displacements occur at the outer cooling jacket and at the plates connecting the feet. As suspected, the deformation amplitude at 1894.6 Hz is larger than that

for 1794.6 Hz. On the one hand, this can be attributed to the stress wave components with lower spatial ordinal numbers (subharmonics). On the other hand, the excitation frequency of 1894.6 Hz coincides with a resonance at 1894.6 Hz.

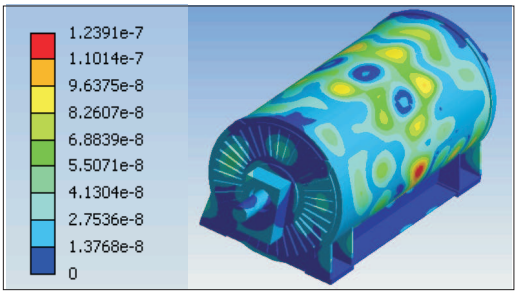


(a) Deformation at 1794.6 Hz in m

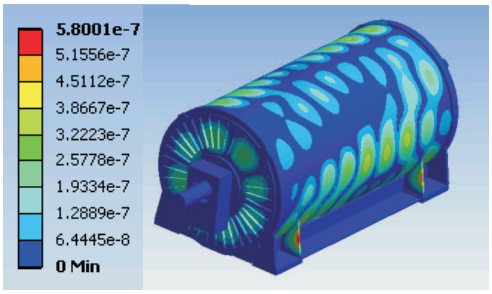


(b) Deformation at 1894.6 Hz in m

Figure 8.5: Real part displacement solution of the harmonic analysis for the induction machine

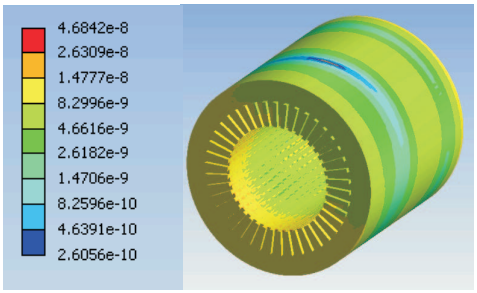


(a) Deformation of stator at 2094.6 Hz in m

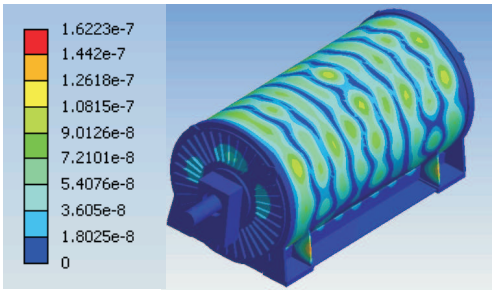


(b) Deformation of housing at 2094.6 Hz in m

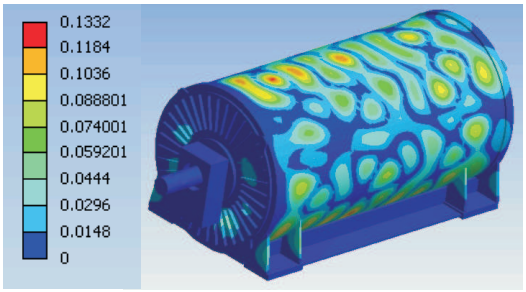


(c) Eigenmode at 2097.3

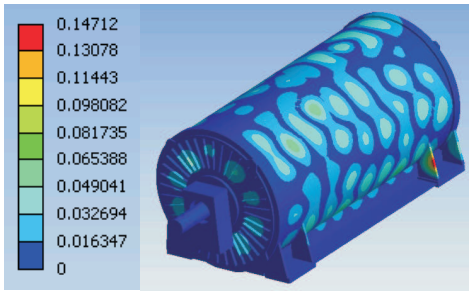


(d) Eigenmode at 2103.5 Hz

Figure 8.6: Real part displacement solution of the harmonic analysis for the induction machine at 2094.6 Hz

In Fig. 8.6, the deformation of the stator and the housing at an excitation frequency of 2094.6 Hz is displayed along with two modal solutions near the excitation frequency. The stator amplitudes are small compared to the deformation of the housing, however it

can be seen that there is a specific characteristic in the axial direction with two minima. Comparing the deformation of the housing with the modal results in Fig. 8.6, it can be seen that the plate bendings, especially those on the feet plates, resemble more the eigenmode at 2103.5 Hz than that at 2097.3 Hz, although the latter one is nearer to the excitation frequency.

Considering (2.46), two terms are identified that determine the structural response. One term is determined by the inverse of the difference of the excitation frequency $\Omega$ and the eigenfrequencies $\omega_i$. If the excitation frequency is near to or even coincides with the eigenfrequency, as is the case at 1894.6 Hz, the deformation amplitude will be large. The second term, and the one that may be the reason for the results in Fig. 8.6, is the product of the force vector with the transposed modal matrix. The stress distribution at 2094.6 Hz seems to be orthogonal to the eigenvector at 2097.3 Hz and to resemble more the eigenvector at 2103.5 Hz.

Summing up the deformation mainly depends on the eigenforms near the excitation frequency and thus these eigenvectors determine the deformation characteristic. The results for the other excitations are depicted in appendix A.8.

## 8.2 Noise computation

In a last step of this analysis, the noise radiated by the machine vibrations, in particular the surface oscillations, is computed. Due to the interaction of the solid with the fluid, the surface vibrations excite the acoustic fluid, i.e. air, enclosing the machine. This leads to pressure fluctuations in the form of acoustic waves, thus sound is radiated from the machine.

The exterior radiation problem that has to be solved is an exterior Neumann problem. The compatibility condition on the surface of the machine requires the velocity of the solid and the fluid to be equal. The normal component of the given surface velocities $\hat{\mathbf{v}}_n$

$$\hat{\mathbf{v}}_n = j\Omega\hat{\mathbf{u}} \cdot \mathbf{n}. \tag{8.4}$$

with the normal vector $\mathbf{n}$ and the displacement value $\hat{\mathbf{u}}$, leads to the Neumann boundary condition (4.42) for this problem. To determine the sound pressure field in the exterior domain $\Omega^+$ the indirect boundary element method is chosen, see section 4.5.

A surface model has been set up and disctretized with 103554 triangular elements, see Fig. 8.7. The average element size has been set to 0.01 m. This means, that for the maximum frequency of 2194.6 Hz around 10 elements per wave length $\lambda = c/f$ exist. Thus, the wave can be represented with sufficient accuracy.

As mentioned in section 4.5, the solution for the exterior radiation problem is polluted by fictitious eigenfrequencies. This issue is of pure mathematical nature due to the boundary element formulation. For the indirect BEM, one approach to overcome this problem is to apply an impedance boundary condition over the inner side of the cavity. As described in [23], prescribing a constant value of $-413.3kg/m^2/s$ $(= -c\rho$

at a temperature of 20°*C*) as impedance on the internal surface allows to completely damp the spurious frequencies polluting the solution over the whole frequency range. The simulation has been carried out with LMS Virtual.Lab Rev.11 [5], which also contains a fast multipole BEM solver, see section 4.5. This has been used to increase the efficiency, in particular regarding the amount of memory. To consider the reflections of the sound waves at the ground, a half space solution is computed. Therefore, a rigid plane is inserted representing the floor on which the machine is mounted.

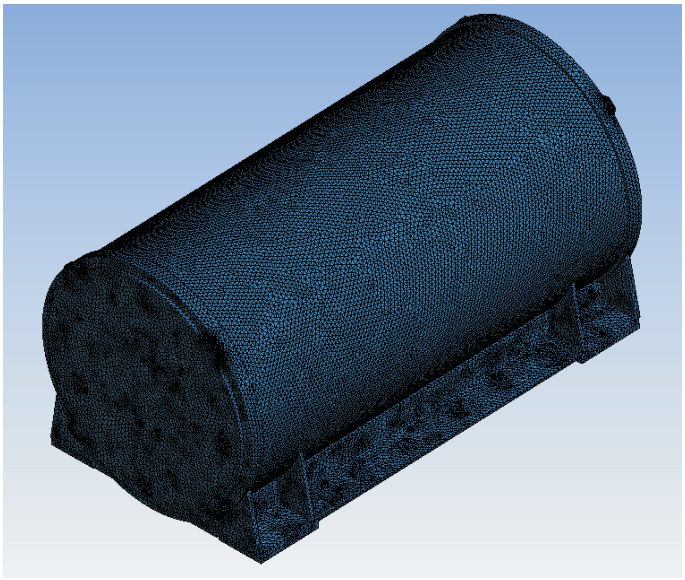

Figure 8.7: Surface mesh for boundary element simulation

In Fig. 8.8 and Fig. 8.9 the results for the sound pressure on the machine's surface are depicted. It can be seen that the maxima of the sound pressure, especially on the cooling jacket, correlate to the deformation characteristics obtained in section 8.1.3. The obvious influence of the structural deformation on the sound radiation can thus clearly be seen. Also at the plates of the bottom of the machine a high sound

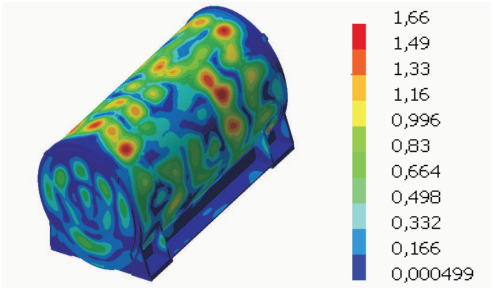


(a) Sound pressure in Pa

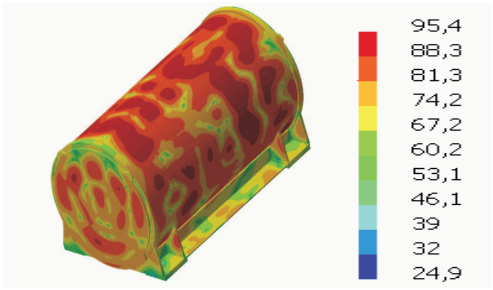


(b) Sound pressure level in dB

Figure 8.8: Sound pressure distribution on the surface of the induction machine at 1794.6 Hz

pressure level can be detected. On the one hand, this can be traced back to the high structural deformation occurring at the vertical plate connecting the feet. On the other hand, however, at the horizontal plate, reflections of the radiated sound pressure must occur, which lead to a high sound pressure level there, although the structural deformation is low compared to the vertical plate, see also Fig. 8.5. The results for the other excitations are

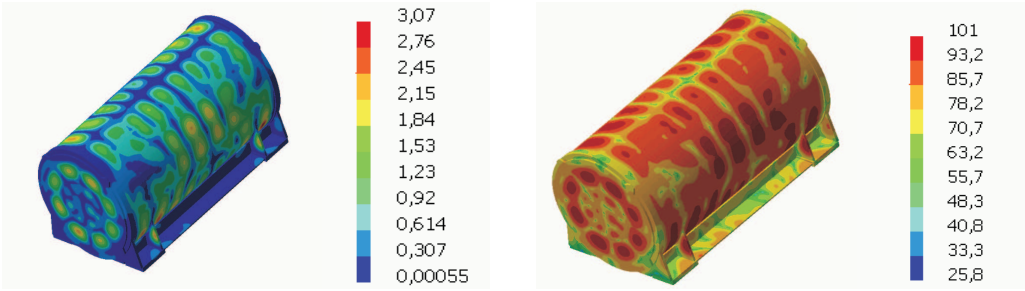


(a) Sound pressure in Pa (b) Sound pressure level in dB

Figure 8.9: Sound pressure distribution on the surface of the induction machine at 1894.6 Hz

depicted in appendix A.9.

To investigate the radiation from the surface into air, an evaluation grid has been set up, discretized with quadrilateral surface elements. The sound pressure is computed in these points and the noise radiation can be investigated. The evaluation grid consists of three planes each perpendicular to one of the coordinate axes.

In Fig. 8.11, the radiation characteristic of the noise spreading from the machine is depicted. It can be seen how the maximum sound pressure occurring at the cylindrical housing spreads out radially and decreases with the distance. Depending on the vibration, the maximal sound pressure occurs at different positions. The results for the other excitations are depicted in appendix A.10.

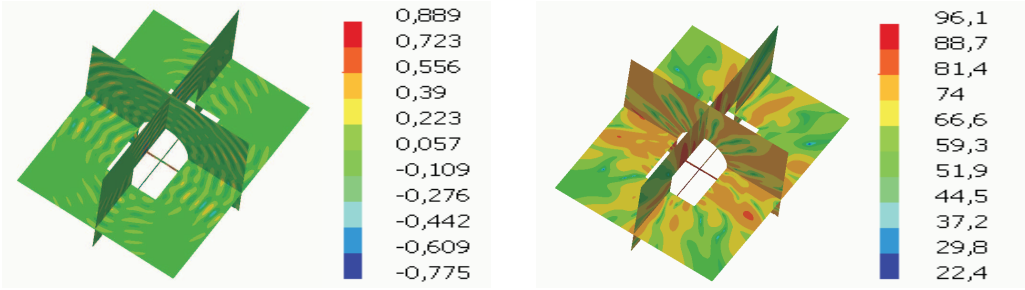


(a) Sound pressure in Pa (b) Sound pressure level in dB

Figure 8.10: Sound pressure distribution at the field points surrounding the induction machine at 1794.6 Hz

### 8.2.1 Comparison with measurement

In section 5.3.1, acoustic measurements have been presented and compared with analytical computation results. To compare the numerical results with the measurements, a cuboid field has been modelled that encloses the machine at a distance of 1 m. The A-weighted

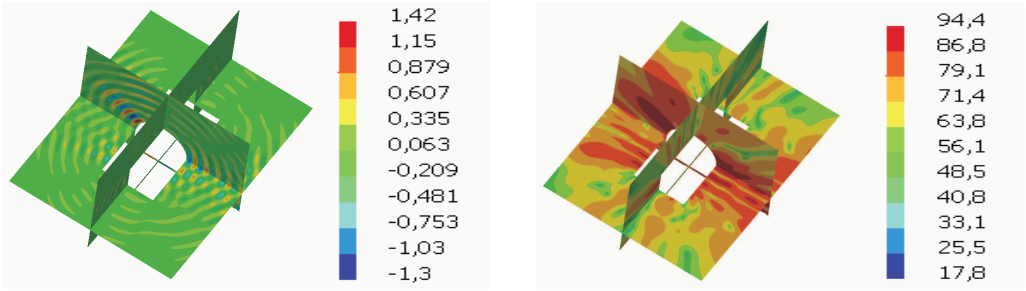


(a) Sound pressure in Pa (b) Sound pressure level in dB

Figure 8.11: Sound pressure distribution at the field points surrounding the induction machine at 1894.6 Hz

root mean squares of the sound pressure level are compared to the measurement results in Table 8.1. The results show no clear tendency. The largest sound pressure level occurs

Table 8.1: Squirrel cage induction machine - Measured and Computed Sound pressure levels (SPL)

| Excitation Frequency | Measured SPL | Computed SPL |
|---|---|---|
| 1594.6 Hz | 52.5 dB(A) | 50 dB(A) |
| 1694.6 Hz | 61 dB(A) | 74 dB(A) |
| 1794.6 Hz | 68.3 dB(A) | 72 dB(A) |
| 1894.6 Hz | 80.5 dB(A) | 77 dB(A) |
| 1994.6 Hz | 64 dB(A) | 61 dB(A) |
| 2094.6 Hz | 61.5 dB(A) | 65 dB(A) |
| 2194.6 Hz | 50 dB(A) | 62 dB(A) |

at a frequency of 1894.6 Hz. However, compared to the measurements this is still an underestimation as is also the case at 1594.6 Hz, though not as grave, and at 1994.6 Hz. For other frequencies the computed sound pressure level exceeds the measured one, for some cases enormously.

One point that explains the deviations is of course the simplified structural modelling, in particular the laminated stack, the windings, the lack of the water in the cooling etc. Further detailed experimental and computational investigations are necessary to obtain proper approaches to consider the complex composition of electrical machines.

# 9 CONCLUSION

The computation of audible noise of electrical machines has been an issue for a long time. However, in recent days, the increase of the applications for electrical machines and the rising sensitivity towards noise leads to more severe regulations to decrease the exposure of human beings to noise. This demands comprehensive computation methods to provide low noise designs.

The review of literature in the first chapter has shown that there are several causes leading to audible noise of electrical machines, namely, aerodynamic, mechanical and electromagnetic causes. The latter ones are the most problematic ones, since they lead to a noise spectrum with large noise peaks at distinct frequencies. The overview is structured according to the computation chain, i.e. electromagnetics, structural mechanics and noise radiation. Each topic comprises first of all the computation methods, i.e. analytical and numerical or, more recently, combinations of the two, and, secondly, experimental investigations especially concerning the structural modelling.

The fundamentals and theoretical background along with analytical and numerical noise computation methods are presented in the chapters 2 to 4. Chapter 3 deals explicitly with the noise computation of induction machines and presents a comprehensive analytic noise computation method. The main advantage of this approach is the possibility to retain the relationship of the noise peaks to the causing electromagnetic fields. Failure to provide this is a disadvantage of the numerical approaches, whose application to electromagnetics, structural mechanics and acoustics is shown in chapter 4. On the one hand, those methods enable a more detailed modelling and, thus, more reliable results may be obtained. On the other hand, the more detailed the model, the larger are the computational efforts as well as the computation times. This makes the analytical methods still an important tool in the design process of electrical machines.

Therefore, an investigation concerning the reliability of a comprehensive analytical approach has been carried out in chapter 5. For each computation step, the results have been compared to numerical and/or experimental results. The comparisons have shown that the analytical approach yields very good results for the frequencies of the magnetic fields and thus the frequencies of the noise peaks. However, discrepancies may occur for the computed amplitudes, in particular of the magnetic fields. These results are well known in the literature, however, some effects occur that have not yet sufficiently been paid attention to. First of all, the comparisons have shown that stress harmonics with large spatial ordinal numbers may have large amplitudes, however, their influence on the structural vibrations is mostly neglected in the literature. This is because it is assumed that those stress wave components do not contribute to the vibrational behaviour. A further point that is derived from the comparisons is the variation of the magnetic field along the axial direction of the air

gap for skewed machines. This results in a variation of the forces along the axial direction, too. Along with the three-dimensional vibration behaviour, also presented in this chapter, this may result in problematic vibrations. Thus, with the outcome of this validation several objectives have been identified to which attention has been paid in the following chapters.

The axial variation of the magnetic field in the air gap has been investigated in detail in chapter 6. For a squirrel cage induction machine, a finite element multi-slice simulation has been carried out at the nominal operating point. The magnetic field components in each slice have been analysed for a model with four and five slices. It has been shown that a cubic spline interpolation in axial direction, which is typically carried out to obtain the field along the axial direction, leads to completely different distributions. A more detailed analysis of the magnetic field components also considering the analytic approach has shown that the variation in axial direction is proportional to the skewing angle. The magnetic field components for the two multi-slice models have been reconstructed and the comparisons have shown a clear agreement. A comparison with a three-dimensional model supported the validity of this approach.

The influence of the axial variation of the obtained stresses on the structural vibration behaviour has been analysed in the chapter 7. The focus has lain on the investigation of stress waves with large spatial ordinal numbers. Therefore, a three-dimensional structural finite element model has been set up and different stress waves applied to the stator and rotor teeth. The results have shown that for stress waves with spatial ordinal numbers in the magnitude of the number of teeth (either stator or rotor, depending on which of them the stress acts) lead to sub harmonics of large amplitudes and low spatial ordinal numbers. This again results in large deformation amplitudes on the stator and thus large vibrations on the housing. Regarding the stresses varying in axial direction, it has been shown that certain eigenmodes of the stator may be excited and thus resonances may occur. Besides that also analyses for stress waves with a spatial ordinal number of one have been carried out and have shown that those lead to the most critical vibrations, either if applied to the stator teeth or to the rotor teeth.

The vibration structure, especially the housing, excites the surrounding air and leads to pressure fluctuations and thus audible noise. The influence of the housing on the noise radiation has been mentioned in the literature, however, only few works exist which explicitly deal with this phenomenon. This is the topic presented in chapter 8 of this work. Therefore, a very detailed three-dimensional finite element model has been set up. The main problem thereby is the setting of the material parameters especially for the laminated stacks and their insulated windings. To obtain an efficient model, some assumptions have been made and a homogeneous body assumed. A modal analysis of the structure has shown a high modal density, mainly due to the plates of the housing. In a next step the structural responses due to the stress harmonics acting on the stator teeth at nominal operating point are computed. In addition to the structural model, a boundary element model has been set up to determine the noise radiation. The results show that the noise radiation clearly corresponds to the plate bending of the housing. A comparison of the stress spectrum, obtained after the electromagnetic field computation, and the computed noise spectrum also shows

different characteristics. One obvious reason for this are the structural eigenfrequencies that may lead to large vibration amplitudes even for forces with small amplitudes. A further reason may be the cancellation of acoustic waves. This can be seen for some field results, however, their effect on the noise reduction can not be easily be determined. The main problem that has arisen in this work is the determination of the material parameters of the laminated stator core. More detailed investigations on the vibrational behaviour of such stacks with the aim of obtaining a proper parameter set for the vibration computation is a task for future work.

# A APPENDIX 1

## A.1 Supplements to the Maxwell stress tensor

In cylinder coordinates the following time dependent stress vector is obtained in air with $\mu = \mu_0$ and for $B_z = 0$:

$$\boldsymbol{\sigma}_m(r,\varphi,z,t) = -\frac{1}{2\mu_0}\begin{pmatrix} B_r^2 - B_\varphi^2 \\ 2B_rB_\varphi \end{pmatrix} \tag{A.1}$$

In the frequency domain the relation for the surface force density is computed by a convolution of the frequency spectra of the corresponding components of the magnetic flux density $\hat{B}(j\omega)$ as

$$\hat{\sigma}_r(j\omega) = -\frac{1}{2\mu_0}\left(\hat{B}_r(j\omega) * \hat{B}_r(j\omega) - \hat{B}_\varphi(j\omega) * \hat{B}_\varphi(j\omega)\right) \tag{A.2}$$

$$\sigma_\varphi(j\omega) = -\frac{1}{\mu_0}\left(\hat{B}_r(j\omega) * \hat{B}_\varphi(j\omega)\right) \tag{A.3}$$

where $\omega$ is the angular frequency.

## A.2 Physiological acoustics

A healthy human ear typically covers a frequency range from 16Hz to 16KHz. However, humans' physiological sensation of loudness is varying with the frequency [52]. Statistical investigations have been carried out according to DIN 45633 and DIN EN 60651, respectively, to determine the sensation of loudness in relation to frequency and sound level. In Fig. A.1a the equal-loudness contour is depicted. With this diagram it is possible to determine the loudness for a corresponding sound level and frequency. The loudness level is measured in phon and equals the sound level in dB for a frequency of 1000Hz. For technical applications, the non-linear physiological sensation is typically accounted for with valuation curves. According to DIN 45 634, four weighting functions/curves denoted with A, B, C and D are determined, which are depicted in Fig. A.1b. The most important for industrial applications is the A-weighting function, which corresponds to the inverse of the loudness curve for 30Hz. The A-weighted sound pressure level is then denoted with $dB(A)$.

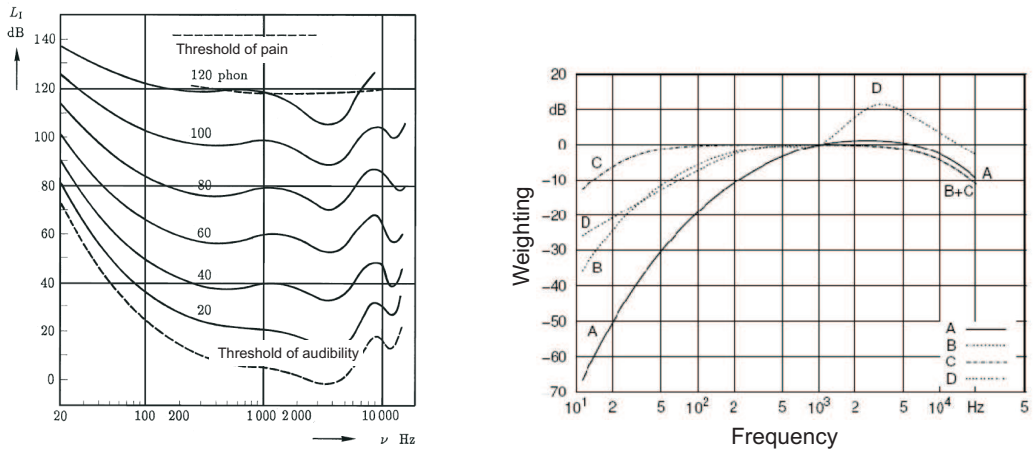


(a) Auditory sensation area (b) A-,B-,C- and D-Weighting curves

Figure A.1: Noise level and weighting curves [52]

## A.3 Galerkin equations for quasi static fields

In the non-conducting domain $\Omega_n$ the following Galerkin equations arise:

$$\int_{\Omega_n} \nabla \times \mathbf{N}_i \; \nu \nabla \times \mathbf{A}_h \mathrm{d}\Omega = \int_{\Omega_n} \mathbf{N}_i \; \mathbf{J}_0 \mathrm{d}\Omega \qquad i = 1,2\ldots,n_e \qquad \text{in } \Omega_n \tag{A.4}$$

In the conducting domain $\Omega_c$ the Galerkin equations are as follows:

$$\int_{\Omega_c} \nabla \times \mathbf{N}_i \; \nu \nabla \times \mathbf{A}_h \mathrm{d}\Omega + \int_{\Omega_c} \frac{\partial}{\partial t} \mathbf{N}_i \; \sigma \mathbf{A}_h \mathrm{d}\Omega + \int_{\Omega_c} \frac{\partial}{\partial t} \mathbf{N}_i \; \sigma \nabla v_h \mathrm{d}\Omega = \mathbf{0} \qquad \text{in } \Omega_c \tag{A.5}$$

$$\int_{\Omega_c} \frac{\partial}{\partial t} \nabla N_j \; \sigma \mathbf{A}_h \mathrm{d}\Omega + \int_{\Omega_c} \frac{\partial}{\partial t} \nabla N_j \; \sigma \nabla v_h \mathrm{d}\Omega = 0 \tag{A.6}$$

$$i = 1,2\ldots,n_e \qquad j = 1,2\ldots,n_n \tag{A.7}$$

$n_e$ is the number of unknown edge based shape functions $\mathbf{N}_i$ and $n_n$ the number of unknown nodal based shape functions $N_i$. Both, the shape functions $\mathbf{N}_i$ for the vector potential $\mathbf{A}$ and $N_i$ for the scalar potential $v$ are linearly independent. However, there are linear interdependences between the edge based shape functions and the nodal based shape functions as the gradient of the nodal based functions are in the function space of the edge based shape functions [15]:

$$\nabla N_i = \sum_{i=1}^{n_e} c_{ik} \mathbf{N}_k, \qquad i = 1,2,\ldots,n_n - 1 \tag{A.8}$$

$$\tag{A.9}$$

By taking the curl of (A.8), the linear combinations of the equations in (A.5) result in the same equations as in (A.6). Thus, the obtained system matrix is singular.

## A.4 Derivation of system matrices of mechanical finite element system

Inserting the approximation functions (4.33) and (4.34) and the constitutive law (4.35) in the formulation for the virtual work (4.30) the Galerkin equations are obtained as follows:

$$\left[\sum_m \int_{V^{(m)}} \mathbf{H}^{(m)^T} \rho \mathbf{H}^{(m)} \mathrm{d}V^{(m)}\right] \ddot{\mathbf{u}} + \left[\sum_m \int_{V^{(m)}} \mathbf{B}^{(m)^T} \mathbf{C}^{(m)} \mathbf{B}^{(m)} \mathrm{d}V^{(m)}\right] \mathbf{u} = \sum_m \left( \int_{V^{(m)}} \mathbf{H}^{(m)^T} \mathbf{f}_B^{(m)} \mathrm{d}V^{(m)} + \int_{A^{(m)}} \mathbf{H}^{(m)^T} \mathbf{f}_S^{(m)} \mathrm{d}A^{(m)} \right) \quad \text{(A.10)}$$

for

$$\delta \mathbf{s}(x,y,z)^{(m)} = \mathbf{H}(x,y,z)^{(m)}, \qquad \delta \boldsymbol{\varepsilon}(x,y,z)^{(m)} = \boldsymbol{\mathcal{B}}(x,y,z)^{(m)}. \quad \text{(A.11)}$$

The obtained terms can now be gathered in a mass matrix $\mathbf{M}$

$$\mathbf{M} = \sum_m \int_{V^{(m)}} \mathbf{H}^{(m)^T} \rho \mathbf{H}^{(m)} \mathrm{d}V^{(m)}, \quad \text{(A.12)}$$

a stiffness matrix $\mathbf{K}$

$$\mathbf{K} = \sum_m \int_{V^{(m)}} \mathbf{B}^{(m)^T} \mathbf{C}^{(m)} \mathbf{B}^{(m)} \mathrm{d}V^{(m)} \quad \text{(A.13)}$$

and a nodal force vector $\mathbf{F}$

$$\mathbf{F} = \sum_m \left( \int_{V^{(m)}} \mathbf{H}^{(m)^T} \mathbf{f}_B^{(m)} \mathrm{d}V^{(m)} + \int_{A^{(m)}} \mathbf{H}^{(m)^T} \mathbf{f}_S^{(m)} \mathrm{d}A^{(m)} \right). \quad \text{(A.14)}$$

## A.5 Machine parameters

Table A.1: Squirrel cage induction machine - Machine Parameters

| | | |
|---|---|---|
| Nominal Power | $P$ | 1.25 MW |
| Feeding voltage | $f$ | 5.5 kV |
| Stator current for nominal operating point | $I_1$ | 150.5 A |
| Slip at nominal operating point | $s$ | 0.3% |
| Rotor speed at nominal operating point | $n$ | 2991.1 rpm |
| Line frequency | $f_1$ | 50 Hz |
| Number of stator slots | $N_S$ | 42 |
| Number of rotor slots | $N_R$ | 36 |
| Number of pole pairs | $p$ | 1 |
| Number of cords | $m$ | 3 |

Table A.2: Squirrel cage induction machine - Eigenfrequencies

| Mode 0 | Mode 1 | Mode 2 | Mode 3 | Mode 4 | Mode 5 | Mode 6 |
|---|---|---|---|---|---|---|
| 1744.9 Hz | 2461.9 Hz | 335.5 Hz | 894.2 Hz | 1592.7 Hz | 2374.5 Hz | 3201.6 Hz |

Table A.3: Slip-ring induction machine - Machine Parameters

| | | |
|---|---|---|
| Nominal Power | $P$ | 2.2 MW |
| Stator current for nominal operating point | $I_1$ | 2222.3 A |
| Slip at nominal operating point | $s$ | $-0.9683\%$ |
| Rotor speed at nominal operating point | $n$ | 1009.7 rpm |
| Line frequency | $f_1$ | 50 Hz |
| Number of stator slots | $N_S$ | 72 |
| Number of rotor slots | $N_R$ | 54 |
| Number of pole pairs | $p$ | 2 |
| Number of cords | $m$ | 3 |

## A.6 Frequencies and spatial ordinal numbers of magnetic field components for squirrel cage induction machine

### A.6.1 Rotor slot harmonics

$$k = p \pm N_R \qquad k_1 = 37 \qquad k_2 = -35$$

$$f_k = f_1(1 \pm (1-s)\frac{N_R}{p}) \qquad f_{k_1} = 1844,6 \text{ Hz} \qquad f_{k_2} = -1744.6 \text{ Hz}$$

### A.6.2 Stress components due to fundamental field

$$n = p \pm k \qquad n11 = p + k_1 = 38 \qquad n12 = p + k_2 = -34$$

$$n21 = p - k_1 = -36 \qquad n22 = p - k_2 = 36$$

$$f_n = f_1 \pm f_k \qquad f11 = f_1 + f_{k_1} = 1894.6 \text{ Hz} \qquad f12 = f_1 + f_{k_2} = -1694.6 \text{ Hz}$$

$$f21 = f_1 - f_{k_1} = -1794.6 \text{ Hz} \qquad f22 = f_1 - f_{k_2} = 1794.6 \text{ Hz}$$

## A.7 Material parameters for the structural simulation of the squirrel cage induction machine

Table A.4: Material parameters for the laminated stacks

| | | |
|---|---|---|
| Density | $\rho$ | $7525.7\ \text{kg/m}^3$ |
| Young's modulus in *x*-direction | $E_x$ | $2 \cdot 10^{11}$ Pa |
| Young's modulus in *y*-direction | $E_y$ | $2 \cdot 10^{11}$ Pa |
| Young's modulus in *z*-direction | $E_z$ | $2.5 \cdot 10^{10}$ Pa |
| Shear modulus in *xy*-direction | $G_{xy}$ | $7.7 \cdot 10^{10}$ Pa |
| Shear modulus in *yz*-direction | $G_{yz}$ | $1.1 \cdot 10^{10}$ Pa |
| Shear modulus in *xz*-direction | $G_{xz}$ | $1.1 \cdot 10^{10}$ Pa |
| Poisson ratio | $\nu$ | 0.31 |

## A.8 Deformations due to electromagnetic force excitation - Finite element simulation results

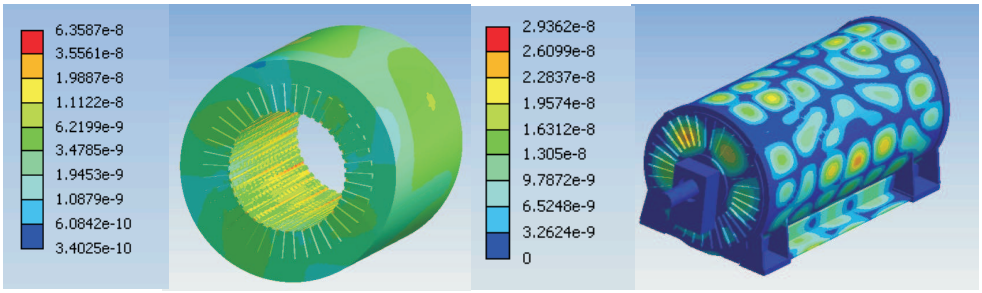


(a) Deformation of stator in m (b) Deformation of housing in m

Figure A.2: Real part displacement solution of the harmonic analysis for the induction machine at 1594.6 Hz

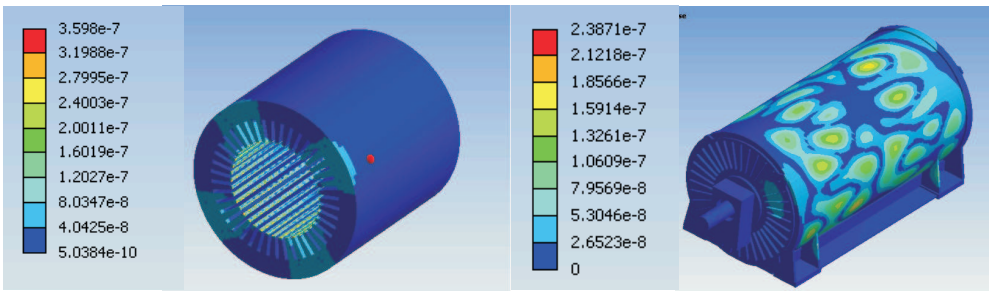


(a) Deformation of stator in m (b) Deformation of housing in m

Figure A.3: Real part displacement solution of the harmonic analysis for the induction machine at 1694.6 Hz

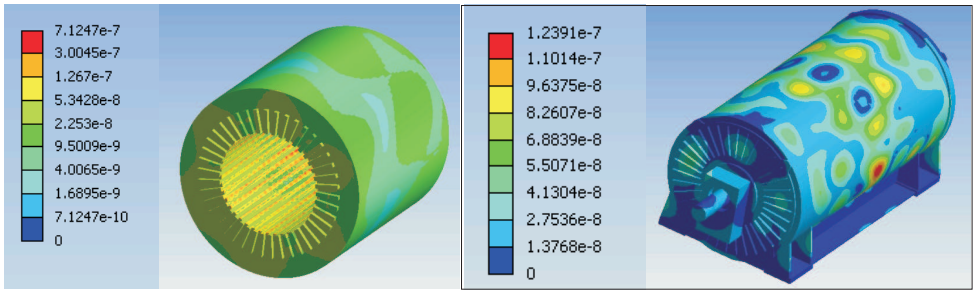


(a) Deformation of stator in m (b) Deformation of housing in m

Figure A.4: Real part displacement solution of the harmonic analysis for the induction machine at 1794.6 Hz

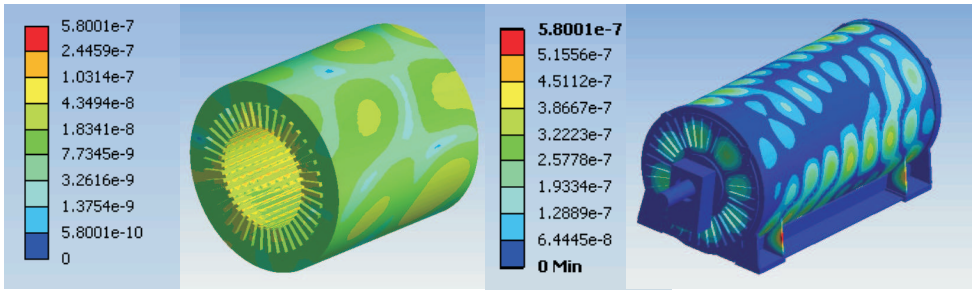


(a) Deformation of stator in m (b) Deformation of housing in m

Figure A.5: Real part displacement solution of the harmonic analysis for the induction machine at 1894.6 Hz

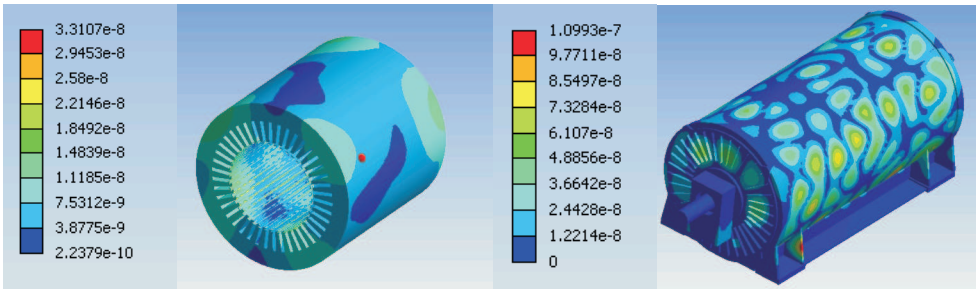


(a) Deformation of stator in m (b) Deformation of housing in m

Figure A.6: Real part displacement solution of the harmonic analysis for the induction machine at 1994.6 Hz

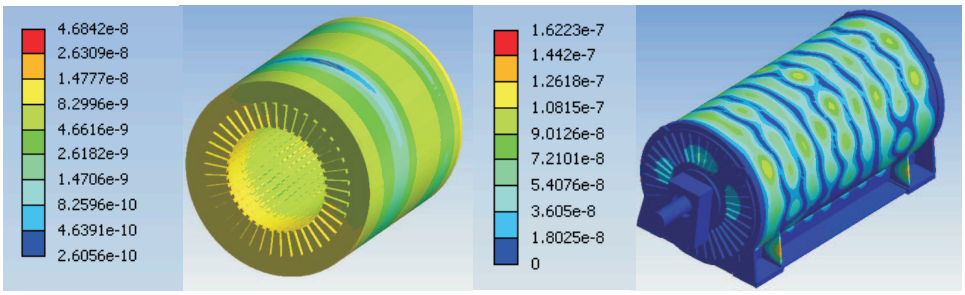


(a) Deformation of stator in m (b) Deformation of housing in m

Figure A.7: Real part displacement solution of the harmonic analysis for the induction machine at 2094.6 Hz

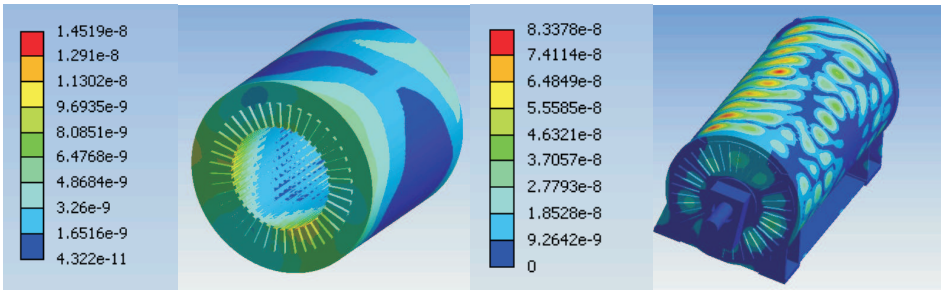


(a) Deformation of stator in m (b) Deformation of housing in m

Figure A.8: Real part displacement solution of the harmonic analysis for the induction machine at 2194.6 Hz

## A.9 Noise result on machine surface

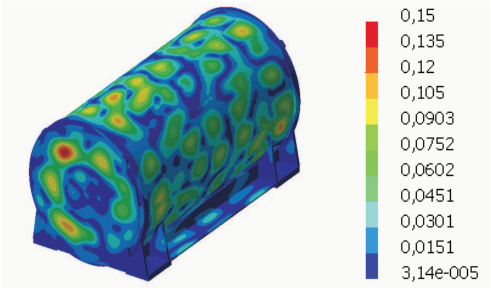


(a) Sound pressure in Pa

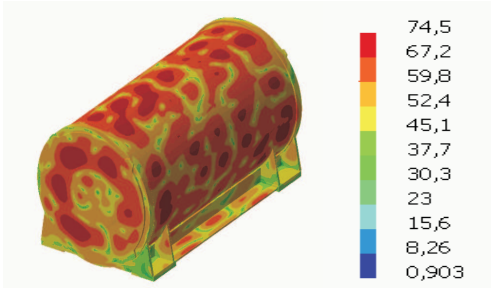


(b) Sound pressure level in dB

Figure A.9: Sound pressure distribution on the surface of the induction machine at 1594.6 Hz

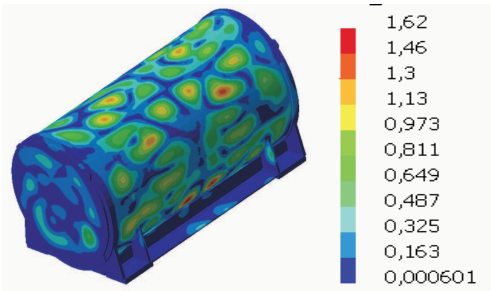


(a) Sound pressure in Pa

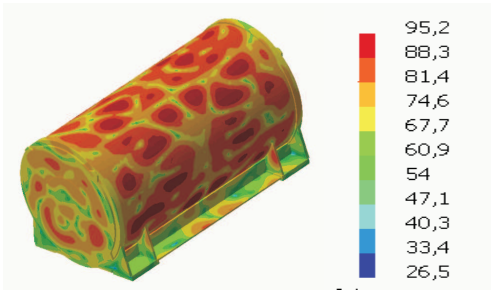


(b) Sound pressure level in dB

Figure A.10: Sound pressure distribution on the surface of the induction machine at 1694.6 Hz

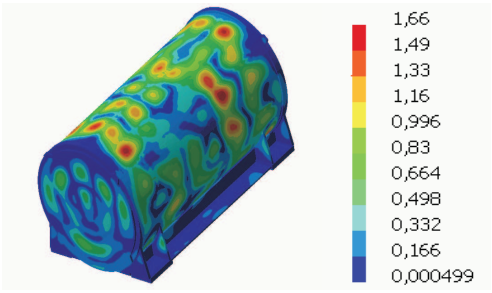


(a) Sound pressure in Pa

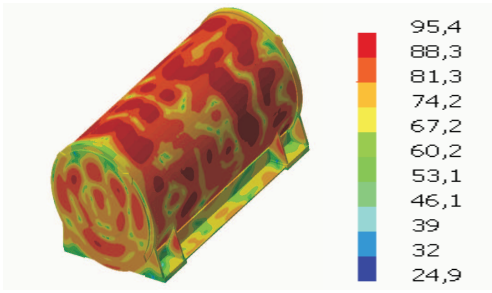


(b) Sound pressure level in dB

Figure A.11: Sound pressure distribution on the surface of the induction machine at 1794.6 Hz

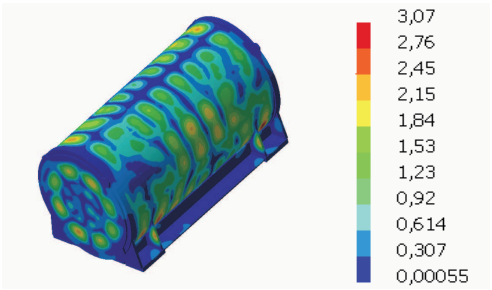


(a) Sound pressure in Pa

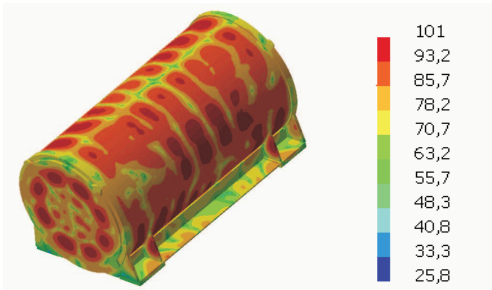


(b) Sound pressure level in dB

Figure A.12: Sound pressure distribution on the surface of the induction machine at 1894.6 Hz

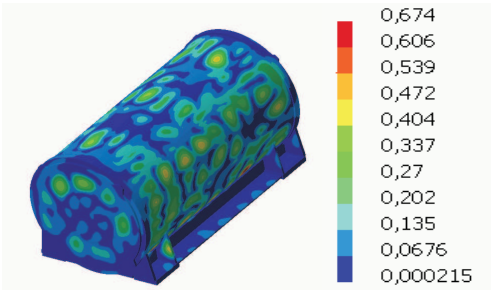


(a) Sound pressure in Pa

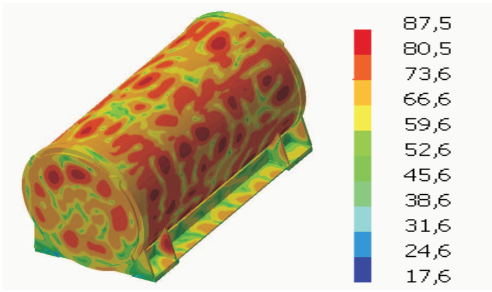


(b) Sound pressure level in dB

Figure A.13: Sound pressure distribution on the surface of the induction machine at 1994.6 Hz

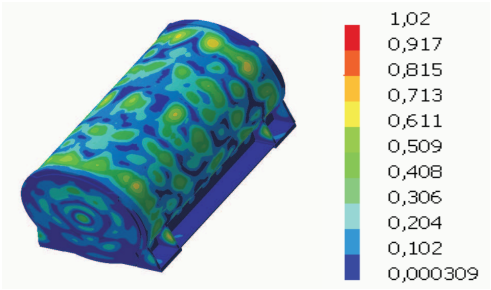


(a) Sound pressure in Pa

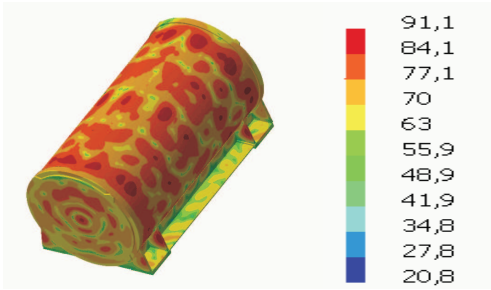


(b) Sound pressure level in dB

Figure A.14: Sound pressure distribution on the surface of the induction machine at 2094.6 Hz

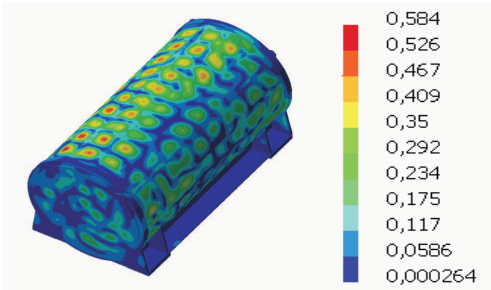


(a) Sound pressure in Pa

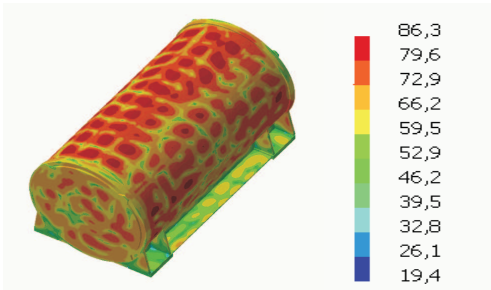


(b) Sound pressure level in dB

Figure A.15: Sound pressure distribution on the surface of the induction machine at 2194.6 Hz

## A.10 Noise result on field points

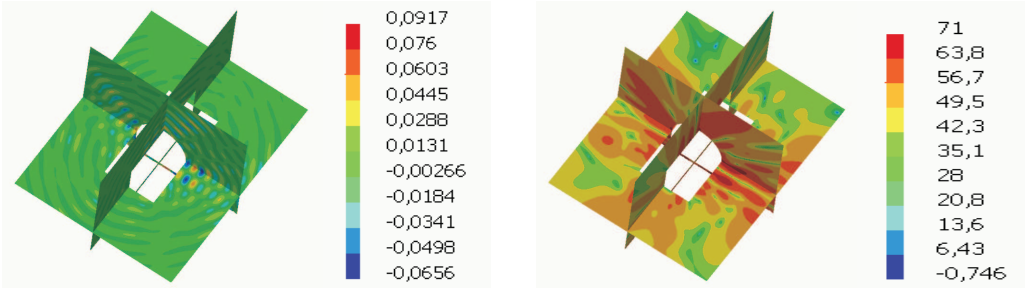


(a) Sound pressure in Pa (b) Sound pressure level in dB

Figure A.16: Sound pressure distribution at the field points surrounding the induction machine at 1594.6 Hz

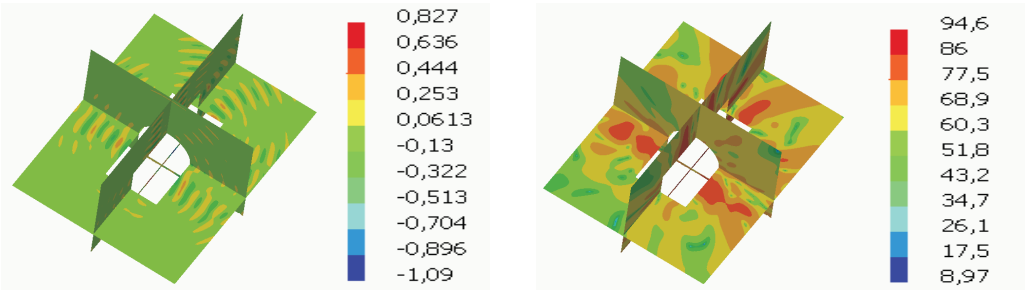


(a) Sound pressure in Pa (b) Sound pressure level in dB

Figure A.17: Sound pressure distribution at the field points surrounding the induction machine at 1694.6 Hz

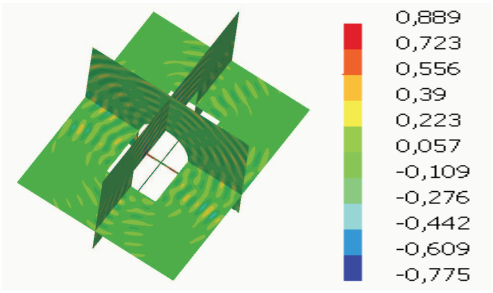


(a) Sound pressure in Pa

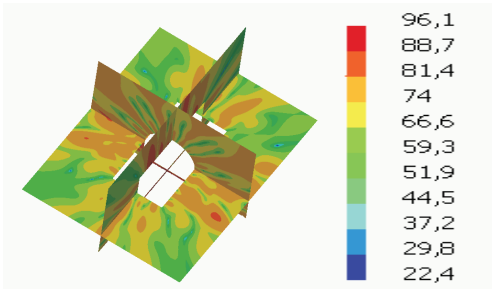


(b) Sound pressure level in dB

Figure A.18: Sound pressure distribution at the field points surrounding the induction machine at 1794.6 Hz

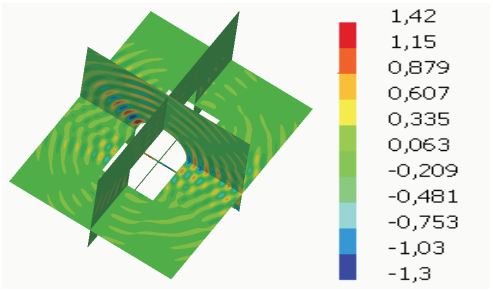


(a) Sound pressure in Pa

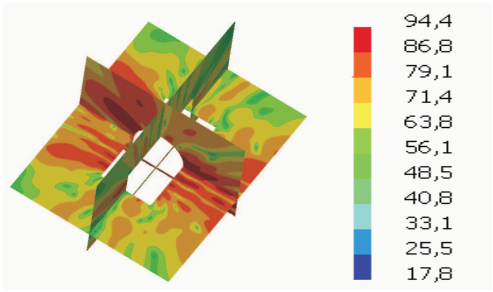


(b) Sound pressure level in dB

Figure A.19: Sound pressure distribution at the field points surrounding the induction machine at 1894.6 Hz

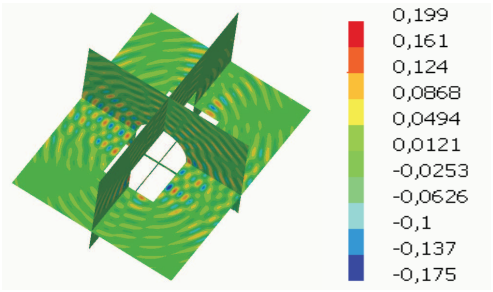


(a) Sound pressure in Pa

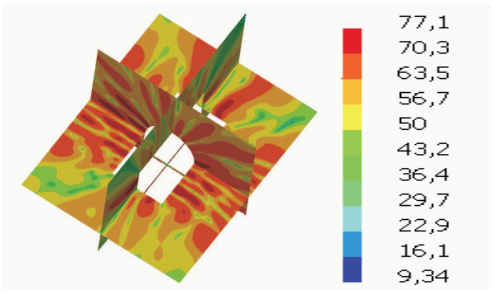


(b) Sound pressure level in dB

Figure A.20: Sound pressure distribution at the field points surrounding the induction machine at 1994.6 Hz

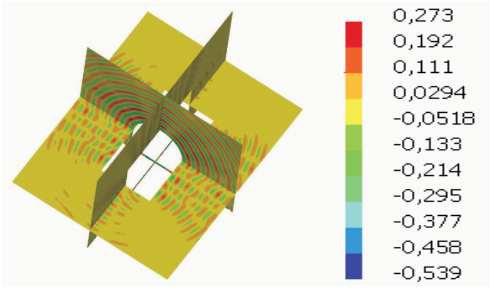


(a) Sound pressure in Pa

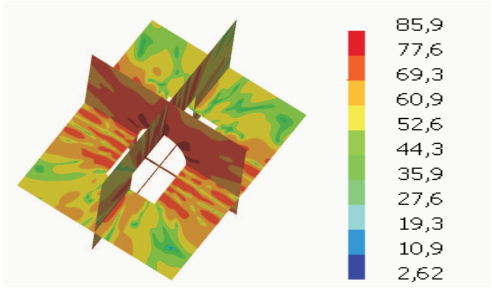


(b) Sound pressure level in dB

Figure A.21: Sound pressure distribution at the field points surrounding the induction machine at 2094.6 Hz

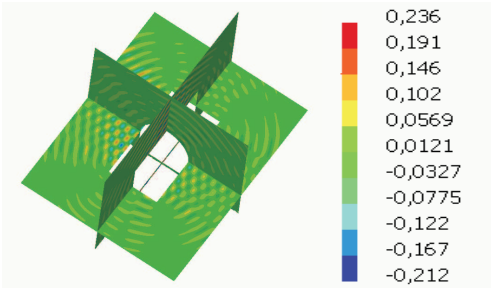


(a) Sound pressure in Pa

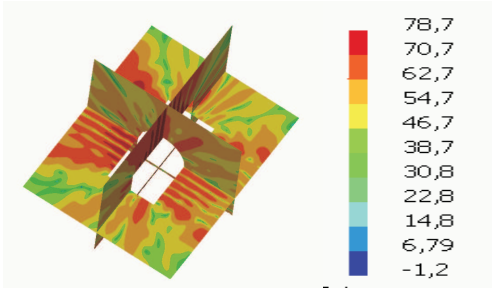


(b) Sound pressure level in dB

Figure A.22: Sound pressure distribution at the field points surrounding the induction machine at 2194.6 Hz

## REFERENCES


[1] DIN-EN 60034-9 - Drehende elektrische Maschinen - Teil 9 Geräuschgrenzwerte.

[2] DIN EN ISO 1680:2000-02 - Akustik - Verfahren zur Messung der Luftschallemission von drehenden elektrischen Maschinen.

[3] *Engineering Simulation Software, Ansys Inc., http://www.ansys.com.*

[4] Health and Environment in Europe: Progress Assessment.

[5] *LMS Virtual.Lab Acoustics v11, www.lmsintl.com.*

[6] *ANSYS 11.0 documentation. Canonsburg: SAS IP*, 2007.

[7] Belahcen A., Arkkio A., Klinge P., Linjama J., Voutilainen V., and Westerlund J. Radial forces calculation in a synchronous generator for noise analysis. In *Chinese International Conference on Electrical Machines (CICEMt'99),* Xian, PR China, August 1999.

[8] P. L. Alger. The magnetic noise of polyphase induction motors. *Power Apparatus and Systems, Part III. Transactions of the American Institute of Electrical Engineers*, 73(1):118 –125, 1954.

[9] K. J. Bathe. *Finite Element Procedures*. Prentice-Hall Inc., Upper Saddle River, New Jersey, 1996.

[10] A. Belahcen. Magnetoelastic coupling in rotating electrical machines. *IEEE Transactions on Magnetics*, 41(5):1624 – 1627, 2005.

[11] A. Belahcen. Vibrations of rotating electrical machines due to magnetomechanical coupling and magnetostriction. *IEEE Transactions on Magnetics*, 42(4):971 –974, 2006.

[12] M. E. H. Benbouzid, G. Reyne, S. Derou, and A. Foggia. Finite element modeling of a synchronous machine: electromagnetic forces and mode shapes. *IEEE Transactions on Magnetics*, 29(2):2014 –2018, 1993.

[13] J. Le Besnerais, A. Fasquelle, M. Hecquet, J. Pelle, V. Lanfranchi, S. Harmand, P. Brochet, and A. Randria. Multiphysics Modeling: Electro-Vibro-Acoustics and Heat Transfer of PWM-Fed Induction Machines. *IEEE Transactions on Industrial Electronics*, 57(4):1279 –1287, 2010.

[14] Jean Le Besnerais, Vincent Lanfranchi, Michel Hecquet, and Pascal Brochet. Characterization and reduction of magnetic noise due to saturation in induction machines. *IEEE Transactions on Magnetics*, 45(4):2003–2008, 2009.

[15] O. Bíró. Edge element formulation of eddy current problems. *Computational Methods in Applied Mechanics and Engineering*, 169(3):391–405, 1999.

[16] M. Boesing and R.W. De Doncker. Exploring a vibration synthesis process for the acoustic characterization of electric drives. *IEEE Transactions on Industry Applications*, 48(1):70 –78, 2012.

[17] M. Boesing, T. Schoenen, K.A. Kasper, and R.W. De Doncker. Vibration synthesis for electrical machines based on force response superposition. *IEEE Transactions on Magnetics*, 46(8):2986 –2989, 2010.

[18] Alain Bossavit. Virtual power principle and Maxwell's tensor: which comes first? *Compel*, 30(6):1804 – 1814, 2011.

[19] F. T. Chapman. The production of noise and vibration by certain squirrel-cage induction motors. *Journal of the Institution of Electrical Engineers*, 61(313):39 –48, 1922.

[20] M. V. K. Chari and Peter P. Silvester. *Finite Elements in Electrical and Magnetic Field Problems (Wiley Series in Numerical Methods in Engineering)*. John Wiley and Sons Inc., New York, 1980.

[21] R. D. Ciskowski and C. A. Brebbia, editors. *Boundary Element Methods in Acoustics*. Computational Mechanics Publications, Southampton, UK and Elsevier Applied Science, Essex, UK, 1991.

[22] L. Cremer, M. Heckl, and B.A.T. Petersson. *Structure Borne Sound*. Springer, Berlin Heidelberg New York, 2005.

[23] R. D'Amico, A. Pratellesi, M. Pierini, and M. Tournour. Efficient method to avoid fictitious eigenvalues for indirect bem. In *International Conference on Noise and Vibration Engineering (ISMA 2010)*, Leuven, Belgium, 20-22 September 2010.

[24] P. Dziwniel, B. Boualem, F. Piriou, J. P. Ducreux, and P. Thomas. Comparison between two approaches to model induction machines with skewed slots. *IEEE Transactions on Magnetics*, 36(4):1453–1457, 2000.

[25] Eickhoff. Structural resonances of stator core stacks. Technical report, ELIN Motoren Gmbh, 1979.

[26] E. Erdelyi. Predetermination of sound pressure levels of magnetic noise of polyphase induction motors. *Power Apparatus and Systems Part III, Transactions of the American Institute of Electrical Engineers*, 74(3):1269 –1280, 1955.

[27] K. Federhofer. *Dynamik des Bogenträgers und Kreisringes*. Springer Verlag, Wien, 1950.

[28] Jens O. Fiedler, Knut A. Kasper, and Rick W. Doncker. Calculation of the Acoustic Noise Spectrum of SRM Using Modal Superposition. *IEEE Transactions on Industrial Electronics*, 57(9):2939–2945, 2010.

[29] Heinrich Frohne. *Über die primären Bestimmungsgrössen der Lautstärke bei Asynchronmaschinen*. PhD thesis, Fakultät für Maschinenwesen der Technischen Hochschule Hannover, 1959.

[30] Martin Furlan, Andrej Cernigoj, and Miha Boltezar. A coupled electromagnetic-mechanical-acoustic model of a dc electric motor. *Compel*, 22(4):1155 – 1165, 2003.

[31] S. D. Garvey. The vibrational behaviour of laminated components in electrical machines. In *Fourth International Conference on Electrical Machines and Drives (conf. Publ. no.310)*, London, UK, 13-15 September 1989.

[32] Robert Gasch and Klaus Knothe. *Strukturdynamik - Band 1: Diskrete Systeme*. Springer-Verlag Berlin Heidelberg New York, 1987.

[33] Robert Gasch and Klaus Knothe. *Strukturdynamik - Band 2: Kontinua und ihre Diskretisierung*. Springer-Verlag Berlin Heidelberg New York, 1989.

[34] Jacek F. Gieras, Chong Wang, and Joseph Cho Lai. *Noise of Polyphase Electric Motors*. CRC Press Taylor & Francis Group, Boca Raton, Florida, 2006.

[35] R. S. Girgis and S. P. Verma. Resonant frequencies and vibration behaviour of stators of electrical machines as affected by teeth, windings, frame and laminations. *IEEE Transactions on Power Apparatus and Systems*, PAS-98(4):1446 –1455, 1979.

[36] R. S. Girgis and S. P. Verma. Method for accurate determination of resonant frequencies and vibration behaviour of stators of electrical machines. *IEE Proceedings B - Electric Power Applications*, 128(1):1, 1981.

[37] François Henrotte and Kay Hameyer. Computation of electromagnetic force densities: maxwell stress tensor vs. virtual work principle. *Journal of Computational and Applied Mechanics*, 168(1-2):235–243, 2004.

[38] L. E. Hildebrand. Quiet induction motors. *Transactions of the American Institute of Electrical Engineers*, 49(3):848 –852, 1930.

[39] Frank Ihlenburg. *Finite Element Analysis of Acoustic Scattering*. Springer-Verlag Inc., New-York, 1998.

[40] F. Ishibashi, M. Matsushita, S. Noda, and K. Tonoki. Change of mechanical natural frequencies of induction motor. *IEEE Transactions on Industry Applications*, 46(3):922 –927, 2010.

[41] A. Jacobus and W. Muller. Numerical solution of forces and torques. *IEEE Transactions on Magnetics*, 19(6):2589 – 2592, 1983.

[42] H. Jordan. *Geräuscharme Elektromotoren*. Girardet, Essen, 1950.

[43] T. Kobayashi, F. Tajima, M. Ito, and S. Shibukawa. Effects of slot combination on acoustic noise from induction motors. *IEEE Transactions on Magnetics*, 33(2):2101 –2104, 1997.

[44] E. Kreyszig. *Advanced Engineering Mathematics*. John Wiley and Sons Inc., New York, 1962.

[45] Cornelius Lanczos. *The variational principles of mechanics*. Dover Publications Inc., New York, 1970.

[46] J. Le Besnerais, V. Lanfranchi, M. Hecquet, and P. Brochet. Characterization and reduction of audible magnetic noise due to pwm supply in induction machines. *IEEE Transactions on Industrial Electronics*, 57(4):1288 –1295, 2010.

[47] S. Lepaul and J. K. Sykulsky. Coupling of motion and circuits with electromagnetic analysis. *IEEE Transactions on Magnetics*, 35(3):1602–1605, 1999.

[48] R. Lin, A. Haavisto, and A. Arkkio. Axial flux and eddy-current loss in active region of a large-sized squirrel-cage induction motor. *IEEE Transactions on Magnetics*, 46(11):3933 –3938, 2010.

[49] W. Lo, C. Chan, Z. Zhu, L. Xu, D. Howe, and K. Chau. Acoustic noise radiated by PWM-controlled induction machine drives. *IEEE Transactions on Industrial Electronics*, 47(4):880–889, 2000.

[50] M. Mair, S. Rainer, B. Weilharter, K. Ellermann, and O. Bíró. Numerische und experimentelle modalanalyse eines statorblechpakets. In *Proceedings in Applied Mathematics and Mechanics*, 2011.

[51] Wayne J. Morrill. Harmonic theory of noise in induction motors. *Transactions of the American Institute of Electrical Engineers*, 59(8):474 –480, 1940.

[52] Michael Möser. *Technische Akustik*. Springer, Berlin Heidelberg New York, 2007.

[53] Germar Müller and Bernd Ponick. *Theorie elektrischer Maschinen*. WILEY-VCH Verlag GmbH & Co. KGaA, Weinheim, 2009.

[54] Germar Müller, Karl Vogt, and Bernd Ponick. *Berechnung elektrischer Maschinen*. WILEY-VCH Verlag GmbH & Co. KGaA, Weinheim, 2008.

[55] W. Muller. Comparison of different methods of force calculation. *IEEE Transactions on Magnetics*, 26(2):1058 –1061, 1990.

[56] K. Oberretl. Das zweidimensionale Luftspaltfeld einer Drehstromwicklung mit offenen Nuten. *Electrical Eengineering (Archiv für Elektrotechnik)*, 53(6):371–381, 1979.

[57] A. M. Oliveira, R. Antunes, P. Kuo-Peng, N. Sadowski, and P. Dular. Electrical machine analysis considering field - circuit - movement and skewing effect. *Compel*, 23(4):1080–1091, 2004.

[58] A. V. Oppenheim, R. W. Schafer, and J. R. Buck. *Discrete-time signal processing*. Prentice-Hall, UpperSaddle River, New Jersey, 1999.

[59] Heinz Parkus. *Mechanik der festen Körper*. Springer-Verlag Wien New York, 1995.

[60] R. Perrin-Bit and J. Coulomb. A three-dimensional finite element mesh connection for problems involving movement. *IEEE Transactions on Magnetics*, 31(3):1920–1923, 1995.

[61] S. Rainer, O. Bíró, B. Weilharter, and A. Stermecki. Weak coupling between electromagnetic and structural models for electrical machines. *IEEE Transactions on Magnetics*, 46(8):2807–2810, 2010.

[62] Sergej Rjasanow and Olaf Steinbach. *The Fast Solution of Boundary Integral Equations*. Springer Science+Business Media, LLC, New York, 2010.

[63] J. Roivainen and A. Makinen. Unit-wave response-based computation of magnetic noise of electric machines. In *2010 IEEE International Conference on Industrial Technology (ICIT)*, Viña del Mar - Valparaiso, Chile, 14-17 March 2010.

[64] C. Schlensok, B. Schmülling, M. van der Giet, and K. Hameyer. Electromagnetically excited audible noise - Evaluation and Optimization of electrical machines by numerical simulation. *Compel*, 26(3):727–742, 2007.

[65] C. Schlensok, D. van Riesen, T. Küest, and G. Henneberger. Acoustic simulation of an induction machine with squirrel-cage rotor. *Compel*, 25(2):475–486, 2006.

[66] C. Schlensok, D. van Riesen, M. van der Giet, and K. Hameyer. Deformation analysis of induction machines by means of analytical and numerical methods. *IEEE Transactions on Magnetics*, 44(6):1498–1501, 2008.

[67] Richard Schwertassek and Oskar Wallrapp. *Dynamik flexibler Mehrkörpersysteme*. Vieweg & Sohn Verlagsgesellschaft, 1999.

[68] H. O. Seinsch. *Oberfelderscheinungen in Drehfeldmaschinen - Grundlagen zur analytischen und numerischen Berechnung*. B. G. Teubner, Stuttgart, 1992.

[69] Walter K. Sextro, Kurt Magnus, and Karl Popp. *Schwingungen: Eine Einführung in die physikalischen Grundlagen und die theoretische Behandlung von Schwingungsproblemen*. Vieweg & Teubner Verlag, Wiesbaden, 2008.

[70] Károly Simonyi. *Theoretische Elektrotechnik*. Johann Ambrosius Barth, Leipzig Berlin Heidelberg, 1993.

[71] R. K. Singal, S.P. Verma, and K. Williams. Vibrations of long and short laminated stators of electrical machines part iii: Results for short stators and validity of simplified frequency equation. *Journal of Sound and Vibration*, 129(1):31 – 44, 1989.

[72] R. K. Singal, K. Williams, and S. P. Verma. The effect of winding, frame and impregnation upon the resonant frequencies and vibrational behaviour of an electrical machine stator. *Experimental Mechanics*, 30(3):270–280, 1990.

[73] Arnold Sommerfeld. *Theoretische Physik Band II: Mechanik der verformbaren Körper*. Verlag Harri Deutsch, Thun Frankfurt/M., 1992.

[74] A. Stermecki, O. Bíró, K. Preis, S. Rainer, and G. Ofner. Numerical analysis of steady-state operation of three-phase induction machines by an approximate frequency domain technique. *e & i Elektrotechnik und Informationstechnik*, 128:81–85, 2011.

[75] P. L. Tímár, A. Fazekas, J. Kiss, A. Miklós, and S. J. Yang. *Noise and Vibration of Electrical Machines*. Elsevier, Amsterdam-Oxford-New York-Tokyo, 1989.

[76] Hans Tischmacher and Benjamin Eichinger. Sound optimization of a converter-fed drive system using an acoustic camera in combination with modal analysis. *Compel*, 29(4):1106 – 1115, 2010.

[77] M. van der Giet and K. Hameyer. Identification of homogenized equivalent materials for the modal analysis of composite structures in electrical machines. *IMechE*, 1:437–448, 2008.

[78] M. van der Giet, E. Lange, D. A. P. Corrêa, I. E. Chabu, S. I. Nabety, and K. Hameyer. Acoustic Simulation of a Special Switched Reluctance Drive by Means of Field-Circuit Coupling and Multiphysics Simulation. *IEEE Transactions on Industrial Electronics*, 57(9):2946–2953, 2010.

[79] M. van der Giet, R. Rothe, M. Herranz Gracia, and K. Hameyer. Analysis of noise exciting magnetic force waves by means of numerical simulation and a space vector definition. In *18th International Conference on Electrical Machines ICEM 2008*, Vilamoura, Portugal, 6-9 September 2008.

[80] M. van der Giet, R. Rothe, and K. Hameyer. Asymptotic fourier decomposition of tooth forces in terms of convolved air gap field harmonics for noise diagnosis of electrical machines. *Compel*, 28(4):804–818, 2009.

[81] D. van Riesen, F. Henrotte, C. Schlensok, and K. Hameyer. Coupled simulations in the design of electrical machines. In *International Conference on Computational Methods for Coupled Problems in Science and Engineering*, Santorini, Greece, 25-28 May 2005.

[82] S. Verma and A. Balan. Determination of radial-forces in relation to noise and vibration problems of squirrel-cage induction motors. *IEEE Transactions on Energy Conversion*, 9(2):404–412, 1994.

[83] S. P. Verma and A. Balan. Experimental investigations on the stators of electrical machines in relation to vibration and noise problems. *IEE Proceedings - Electric Power Applications*, 145(5):455–461, 1998.

[84] S. P. Verma and R. S. Girgis. Resonance frequencies of electrical macchine stators having encased construction, Part II: Numerical results and experimental verification. *IEEE Transactions on Power Apparatus and Systems*, PAS-92(5):1586 –1593, 1973.

[85] S. P. Verma and R. S. Girgis. Resonance frequencies of electrical machine stators having encased construction, Part I: Derivation of the general frequency equation. *IEEE Transactions on Power Apparatus and Systems*, PAS-92(5):1577 –1585, 1973.

[86] S. P. Verma and R. S. Girgis. Experimental verification of resonant frequencies and vibration behaviour of stators of electrical machines. part 1: Models, experimental procedure and apparatus. *IEE Proceedings B - Electric Power Applications*, 128(1):12 –21, 1981.

[87] S. P. Verma and R. S. Girgis. Experimental verification of resonant frequencies and vibration behaviour of stators of electrical machines. part 2: Experimental investigations and results. *IEE Proceedings B - Electric Power Applications*, 128(1):22 –32, 1981.

[88] S. P. Verma, K. Williams, and R. K. Singal. Vibrations of long and short laminated stators of electrical machines, part i: Theory, experimental models, procedure and set-up. *Journal of Sound and Vibration*, 129(1):1 – 13, 1989.

[89] S.P. Verma and W. Li. Measurement of vibrations and radiated acoustic noise of electrical machines. In *Sixth International Conference on Electrical Machines and Systems ICEMS 2003*, Beijing, China, 9-11 November 2003.

[90] P. Vijayraghavan and R. Krishnan. Noise in electric machines: a review. *IEEE Transactions on Industry Applications*, 35(5):1007 –1013, 1999.

[91] C. Wang, A. Astfalck, and J.C.S. Lai. Sound power radiated from an inverter-driven induction motor: experimental investigation. *IEE Proceedings - Electric Power Applications*, 149(1):46 – 52, 2002.

[92] C. Wang and J. C. S. Lai. Vibration analysis of an induction motor. *Journal of Sound and Vibration*, 224(4):733 – 756, 1999.

[93] C. Wang, J.C.S. Lai, and A. Astfalck. Sound power radiated from an inverter driven induction motor ii: Numerical analysis. *IEE Proceedings - Electric Power Applications*, 151(3):341 – 348, 2004.

[94] H. Wang and K. Williams. Vibrational modes of thick cylinders of finite length. *Journal of Sound and Vibration*, 191(5):955 – 971, 1996.

[95] H. Wang and K. Williams. Effects of laminations on the vibrational behaviour of electrical machine stators. *Journal of Sound and Vibration*, 202(5):703 – 715, 1997.

[96] S. Watanabe, S. Kenjo, K. Ide, F. Sato, and M. Yamamoto. Natural frequencies and vibration behaviour of motor stators. *IEEE Transactions on Power Apparatus and Systems*, PAS-102(4):949 –956, 1983.

[97] Herbert Weh. Zur elektromagnetischen Schwingungsanregung bei Asynchronmaschinen. *ETZ - Elektrotechnische Zeitschrift - A*, 85(7):193–197, 1964.

[98] Bernhard Weilharter, Oszkár Bíró, Hermann. Lang, and Siegfried Rainer. Computation of the noise radiation of an induction machine using 3D FEM/BEM. In *The 14th International IGTE Symposium on Numerical Field Calculation in Electrical Engineering*, Graz, Austria, 19-22 September 2010.

[99] Bernhard Weilharter, Oszkár Bíró, Hermann. Lang, and Siegfried Rainer. Computation of the noise radiation of an induction machine using 3D FEM/BEM. *Compel*, 30(2):1737–1750, 2011.

[100] Bernhard Weilharter, Oszkár Bíró, Gerorg Ofner, Hermann Lang, and Siegfried Rainer. Validation of a comprehensive analytic approach to determine the noise behaviour of induction machines. In *XIX International Conference on Electrical Machines ICEM 2010*, Rome, Italy, 6-9 September 2010.

[101] Bernhard Weilharter, Oszkár Bíró, Gerorg Ofner, Hermann Lang, and Siegfried Rainer. Validation of a comprehensive analytic noise computation method for induction machines. *IEEE Transactions on Industrial Electronics*, 59(5):2248–2257, 2012.

[102] Bernhard Weilharter, Oszkár Bíró, and Siegfried Rainer. Computation of rotating force waves in induction machines using multi-slice models. In *14th Biennial IEEE Conference on Electromagnetic Field Computation (CEFC)*, Chicago, IL, USA, 9-12 May 2010.

[103] Bernhard Weilharter, Oszkár Bíró, and Siegfried Rainer. Numerical investigation of the 3d vibrational behaviour of skewed induction machines due to rotating force waves. In *ISEF 2011 - XV International Symposium on Electromagnetic Fields in Mechatronics, Electrical and Electronic Engineering*, Funchal, Madeira, 1-3 September 2011.

[104] Bernhard Weilharter, Oszkár Bíró, and Siegfried Rainer. Numerical investigation of the 3d vibrational behaviour of skewed induction machines due to rotating force waves. *Compel*, 31(5):to be published, 2012.

[105] Bernhard Weilharter, Oszkár Bíró, Siegfried Rainer, and Andrej Stermecki. Computation of rotating force waves in skewed induction machines using multi-slice models. *IEEE Transactions on Magnetics*, 47(5):1046 –1049, 2011.

[106] K. Williams, R. K. Singal, and S. P. Verma. Vibrations of long and short laminated stators of electrical machines part ii: Results for long stators. *Journal of Sound and Vibration*, 129(1):15 – 29, 1989.

[107] Z. Q. Zhu, D. Howe, and C. C. Chan. Improved analytical model for predicting the magnetic field distribution in brushless permanent-magnet machines. *IEEE Transactions on Magnetics*, 38(1):229 –238, 2002.

[108] Olgierd Cecil Zienkiewicz. *Finite Element Method*. McGraw-Hill Book Company (UK) Limited Maidenhead - Berkshire - England, 1977.